A Thesis Submitted for the Degree of PhD at the University of Warwick

High Precision measurements for NDE using electromagnetic sensors

Kevin Luke McAughey

THE UNIVERSITY OF
WARWICK

A thesis submitted for the degree of

Doctor of Engineering in Non-Destructive Evaluation

University of Warwick, Department of Physics

September 2014

Contents

List of Figures

List of Tables

Acknowledgements

My greatest thanks must go to my academic supervisor Dr. Rachel Edwards. Without her constant patients, support and proof reading this thesis would be of considerably poorer quality and would have many more typos than it currently does. I must also thank my industrial supervisor Dr. Mark Potter, for his support and friendship throughout my studies, as well as his tolerance of my abuse of the rules of tabletop RPGs. I would also like to thank everyone in the Ultrasonics Group who have been in equal parts helpful, supportive and fun, although I would like to single out both Dr. Phil Petcher and Dr. Charley Fan, for their mentor-ship and unending tolerance of stupid questions. I would also like to thank everyone else in the Department of Physics who have made coffee breaks more interesting, and Christmas dinners more entertaining.

I would also like to thank my family for their support (particularly financial!) during my time at the University of Warwick. A big thanks goes to the members of Warwick Latin and Ballroom Dancesport for welcoming me into the sports club which has defined my last few years at university; my sanity may have long since fled, but I held onto it for slightly longer with your help. I would particularly like to thank my dance partners over the last three years, Daria Gromyko and Ellen Webborn, as they have had to bear the brunt of my "personality". There are many other people to whom I owe my gratitude, but naming names would take many more pages, and enough trees have made that sacrifice.

Lastly I would like to acknowledge the funding provided by both the Research Centre for Non-Destructive Evaluation (RCNDE) and by Sonemat Ltd. which have made this work possible.

Declaration

I declare that the work presented in this thesis is my own except where stated otherwise, and was carried out entirely at the University of Warwick during the period between October 2010 and September 2014, under the supervision of Dr. Rachel Edwards. The research reported here has not been submitted, either wholly or in part, in this or any other academic institution, for admission to a higher degree. Parts of this work, and other work not reported in this thesis, have appeared in other forms, listed here.

Conference proceedings:

- K. L. McAughey, R. S. Edwards, M. D. G. Potter, and S. Dixon,“Thickness Measurements of Sub-Millimetre Thickness Foils Using Lamb Wave Dispersion,” *Submitted* Boise (Idaho), USA: 2014.
- K. L. McAughey, R. S. Edwards, M. D. G. Potter, and S. Dixon, “Ultrasonic Thickness Measurements of Sub-millimetre Thickness Sheets,” in *18th World Conference on Nondestructive Testing*, Durban, South Africa: 2012.

Presentations at national and international conferences:

- K. L. McAughey, R. S. Edwards, M. D. G. Potter, and S. Dixon, “Thickness Measurements of Sub-Millimetre Thickness Foils Using Lamb Wave Dispersion,” presented at the *41st Annual Review of Progress in Quantitative Nondestructive Evaluation (QNDE 2014)*, Boise (Idaho), USA, July 2014. Poster.
- K. L. McAughey, R. S. Edwards, M. D. G. Potter, and S. Dixon, “Thickness measurements of sub-millimetre thickness foils using Lamb wave dispersion,” presented at the *52nd Annual British Conference on Non-Destructive Testing (NDT 2013)*, Telford, UK, Sep. 2013. Talk.
- K. L. McAughey, R. S. Edwards, M. D. G. Potter, and S. Dixon, “Measuring the Miniscule,” presented at the *51st Annual British Conference on Non-Destructive Testing (NDT 2012)*, Daventry, UK, Sep. 2012. Talk.

- K. L. McAughey, R. S. Edwards, M. D. G. Potter, and S. Dixon, “Ultrasonic Thickness Measurements of Sub-millimetre Thick Samples,” presented at the *18th World Conference on Nondestructive Testing (WCNDT 2012)*, Durban, South Africa, April 2012. Talk.
- K. L. McAughey, R. S. Edwards, M. D. G. Potter, and S. Dixon, “Ultrasonic Thickness Measurements of Sub-millimetre Thick Samples Using Electromagnetic Acoustic Transducers,” presented at the *50th Annual British Conference on Non-Destructive Testing (NDT 2011)*, Telford, UK, Sep. 2011. Talk.

Abstract

This thesis is concerned with two separate research projects; thickness measurements of sub-millimetre thickness sheets using the dispersion of Lamb waves, and the one dimensional profile measurement of samples with a resolution of 1 µm with a dynamic range of 2 mm.

The measurement of the wave velocities of the fundamental Lamb wave modes at long wavelengths is used to calculate the thickness of aluminium sheets without any *a priori* knowledge of the material properties of the samples being tested. The approximations used to perform these measurements were originally formulated by Lamb and their range of validity is examined, and found to have an upper limit of 14.1 kHz.mm. The reliability of the measurements across a range of sample thicknesses, from 100 to 500 µm. An empirical extension to the approximations is also presented which greatly extends their range of validity with limited knowledge of the sample properties, to 800 kHz.mm if the longitudinal and transverse sound velocities are known to within 1 % error. As part of this thesis several novel transducer designs for generation of periodic out-of-plane forces suitable for preferentially generating the A_0 wave are also presented.

The measurement of the one dimensional profile of a curved sample made of ferritic steel is performed using eddy current measurements. The eddy current probes used in this manner have first been demonstrated in a laboratory to be capable of measuring a 0.9 µm change in lift-off at a range of 10 mm with a reliability of 90 %. These probes have also been demonstrated to be insensitive to transverse misalignment of ±1 mm to the curved sample. Further to these measurements the system has also been used in field trials at a the site of an industrial partner using custom hardware and software developed during the course of this research. These measurements allow the recreation of the profile of samples within 10 µm of the current standard and have been performed with contaminants, such as a water-oil mixture used for machining, present on the sample under inspection.

Abbreviations

2D-FFT	Two-Dimensional Fast Fourier Transform
AC	Alternating Current
AFM	Atomic Force Microscopy
ADC	Analogue to Digital Converter
CSD	Cross Spectral Density
CT	Computed Tomography
DC	Direct Current
DD	Difference Detection
DFT	Discrete Fourier Transform
EMAT	ElectroMagnetic Acoustic Transducer
FFT	Fast Fourier Transform
FT	Fourier Transform
LCR	Circuit with capacitor, inductor and resistor
NDE	Non-Destructive Evaluation
NDT	Non-Destructive Testing
PDS	Phase Difference Spectrum
PPM	Periodic Permanent Magnet
SH	Shear Horizontal
SNR	Signal-to-Noise Ratio
STD	STandard Deviation
ToFD	Time of Flight Diffraction

Chapter 1

Introduction

This thesis consists of two separate research projects using electromagnetic sensors for non-destructive evaluation (NDE). The first is the use of electromagnetic acoustic transducers (EMATs) to generate and detect ultrasonic guided waves in thin samples, and from this determine the thicknesses of the samples. The specifics of this work is discussed in chapters 3-6. The second project was performed as a piece of commercial research, and so many of the details presented within this thesis remain confidential. This research focused on the use of eddy current coils to perform profile measurements to an accuracy of 1 µm, and in the unredacted version of this thesis details are discussed in chapters 7-10. An overview of the theory for both projects is given in chapter 2, while this chapter introduces the measurement techniques and describes the current state of the art.

1.1 General introduction to NDE

Non-destructive evaluation (often used interchangeably with the term non-destructive testing, or NDT) is a discipline which aims to address the necessity of inspecting components without damaging them [1–3]. These inspections fall into a range of categories, such as flaw detection and residual stress measurements [2,4], and there is some overlap with the related field of metrology for thickness or profile measurements [5–7]. There are a large number of methods employed in NDE inspections, including thermal, radiographical, optical, electromagnetic and ultrasonic techniques, where each technique has advantages and disadvantages, leading to some techniques being more suitable for specific applications.

The two measurement problems discussed in this thesis will be discussed here, as will the application of a number of measurement techniques to these particular problems. The current state of the art for thickness measurements, including using guided ultrasonic waves is discussed in section 1.2, while the theory is given in sections 2.1 and 2.2. An introduction to profile measurements is given in section 1.3, while the theory of using eddy currents to perform lift-off measurements is given in section 2.5.

1.2 Thickness Measurements

The first of the two research projects discussed in this thesis covers thickness measurements of sub-millimetre thickness sheets. Thickness measurements form a key part of NDE, both during the manufacture of components as diverse as gas turbine blades and drinks cans as a form of quality assurance [8], and during the life of the component as a method of detecting damage due to corrosion [9]. Moreover, the range of thicknesses investigated can vary from a few hundred microns to several meters.

1.2.1 Research Problem and motivation for the research

Although thickness measurements cover a very broad field and form a well established branch of NDE, this research aims to expand the field by developing a technique capable of performing thickness measurements on sub-millimetre thickness samples without prior knowledge of the material properties of the sample. The technique proposed would allow thin foils, typically the product of cold-rolling [10], to have their thickness measured ultrasonically without the texture of the roll affecting the measurement [11]. This would allow the radiographic methods which are typically used to be replaced with an intrinsically safe, and calibrationless, ultrasonic method. This replacement would remove the need for users to comply with the large amount health and safety legislation relating to radiographic inspection [12]. The proposed technique could also match on the accuracy of a commercial radiographic system, typically 1 μm [13]. This technique would also have applications to measurements of the wall thickness of drinks cans, as these often have large amounts of texture due to the way they are manufactured [10]. This allows the integrity of the can to be inspected, and reduces the likelihood of the can failing and spilling its contents. Current methods of thickness gauging are discussed here.

1.2.2 Electromagnetic NDE

Electromagnetic methods cover a set of techniques which can be used in NDE, and include diverse measurements such as eddy current testing and magnetic particle inspection [14]. Although some of these techniques can be used for thickness testing, they can also be used for crack detection or quantification of the electrical properties of materials [15–18]. As the depth of penetration of an electromagnetic field into a conductive sample is limited by the skin depth [19], typically in the order of a few hundred microns, these methods are primarily used for surface inspections.

Eddy current testing has previously been used for thickness measurements of both copper and aluminium samples, both in free space and when in the presence of a substrate [18]. In these measurements the impedance of a cylindrical coil held above an electrically conductive sample was measured using an impedance analyser, and an inverse method was used to identify the values of thickness and conductivity at which the impedance of an analytical model most closely matched the experimentally measured impedance. Provided that the sample thickness was between a fifth and half of the radius of the coil both the thickness and the conductivity could be calculated, although for thinner samples at least one of the parameters is required to be known in order to accurately evaluate the analytical solution. However, the thickness estimates from this measurement technique, typically being within 10 % of the actual thickness, are not consistently accurate across the range of samples measured, with the performance of the measurement on an aluminium sample in air being particularly unreliable, consistently producing errors greater than 17 % [18].

A more recent experiment, which aimed to simultaneously measure both the lift-off and thickness of both aluminium and copper sheets, produced significantly more accurate results [20]. These experiments were conducted with a similar cylindrical coil to those mentioned previously, and the same approach of utilising an inverse method was made. In this research, however, the inverse model was simplified using knowledge of the material properties, although the lift-off between the coil and the sample was also used as a variable. The impedance of the coil was measured using an impedance analyser and the analytical solution was evaluated for various values of sample thickness and lift-off in order to most closely match the experimental results. Using this method the accuracy of the thickness measurements on copper samples was approximately 5 % over a range of thicknesses from 22 to 110 μm. The accuracy on the aluminium samples was less consistent, varying between 1 and 17 % over samples ranging from 18 to 108 μm thick. While this shows a large improvement over the previous thickness measurements using eddy currents, the measurement technique still requires accurate knowledge of the electrical properties of the sample. Additionally, the accuracy achieved here is not sufficient for the intended industrial application, where a tolerance of approximately 1 % is believed to be necessary. Indeed, for non-ferritic materials thicker than 100 μm the accuracy achievable by a commercial system is 3 % [21].

1.2.3 Radiography

Radiography is typically used to investigate the bulk of a sample, and the field consists of several similar techniques, using x-rays, gamma rays or, occasionally, neutrons [22, 23]. Radiographical techniques are often used for detecting defects within the bulk of a material, particularly when inspection using other methods is difficult or provides poor results, such as the inspection of concrete [24].

Thickness measurements can be made using a type of radiography which was first used in medicine, known as computed tomography (CT) [25], and this has also been used industrially [26]. In these measurements a large number of images are captured at different angles through the same sample, and these individual images are then combined to form a three dimensional model of the component being inspected. Due to the large number of individual images needed CT measurements can take a large amount of time to perform, and the use of even basic radiography is heavily legislated due to the health risks involved.

A more basic method of measuring the thickness of foils during manufacture using radiography exists, and is widely used [10]. In this method a beta radiation source is placed on the opposite side of the foil from a detector, and the intensity of radiation detected is related to the thickness of the foil by

$$I = I_0 e^{-\mu x}, \tag{1.1}$$

where I_0 is the intensity when no foil is present, μ is the coefficient of attenuation, and x is the thickness of the foil [27]. The intensity measured using this technique is often used as a feedback control for the rolling process, so that the foil produced is of consistent thickness. However, the coefficient of attenuation for the material must be known in order to perform this measurement, which is a limitation compared to the technique proposed which requires no *a priori* knowledge of the material properties of the sample.

1.2.4 Thermography

Thermography uses the flow of thermal energy in a sample to extract information about the sample, and is often used to detect defects such as impact damage or delaminations in composite materials [3]. Thermography can also be used to perform thickness measurements. These are done by heating a sample and then recording images of the sample as it cools using a thermal imaging camera, where the rate of dissipation of the heat in the sample can be used to calculate relative thickness profiles. For coatings of thicknesses between 50 and 400 µm on a substrate the time taken for the heat to travel through the coating can be calculated, which gives an estimate of the thickness, and can be used to successfully differentiate between adjacent areas with different coating thicknesses [28]. Due to the nature of the exponential decay of the thermal energy in the sample the difference between the thicker 400 µm coating and the 300 µm coating is much more apparent than the difference between the 300 µm coating and the 200 µm coating. However, the coatings in this measurement were paints with a low value of thermal conductivity, and as such the measurement is not likely to be directly transferable to a highly thermally conductive material such as aluminium.

Thermography has also been used to characterise material loss due to corrosion in thicker metal samples [29]. In this study a plate with a number of test defects was heated using a quartz lamp heater, activated for a five second pulse. The cooling of the sample was then monitored using a thermal imaging camera, and the hotspots in the image were used to identify the defects, while the times at which these hotspots appeared can be used to measure the depth of the defect. Using this technique regions of 10 % wall loss can be detected in a sample with a nominal thickness of 3 mm, and the areas of wall loss can be effectively sized. However, for thicker samples the lateral heat conduction in the plane of the sample makes the measurements less accurate, and in samples of up to 5 mm nominal thickness the lower limit of detectable wall loss is increased to 25 %. Thickness measurements with an accuracy in the order of 1 % of the sample thickness may be beyond the ability of most thermographic methods, in addition to which the required knowledge of the thermal conductivity of the sample limits the technique.

1.2.5 Ultrasonics

Ultrasonics is a broad field relying on the behaviour of the propagation of sound in a material to infer information about that material. While this has applications to thickness measurements [2,6], ultrasonics can also be used for defect detection and stress measurements [30–32]. This section introduces a number of the applications for which ultrasound can be used, and also discusses some of the methods of generating and detecting ultrasound in a sample. The difference between bulk waves and guided waves for ultrasonics is discussed in greater detail in chapter 2, although the key difference is that guided waves are ultrasonic waves which are geometrically constrained by the medium in which they are propagating. The applications of these waves to thickness measurements will also be discussed in chapter 2.

1.2.5.1 Bulk wave methods

Both time of flight and resonance techniques can be used for thickness measurements, and a detailed description of the use of these methods can be found in section 2.1.2. Time of flight techniques are the most common type of ultrasonic measurements, and in addition to their use in thickness measurements they can also be applied to flaw detection and array based ultrasonics [2, 33]. For simple flaw detection, time of flight measurements can give the distance a particular flaw is located from the transducer, while the amplitude of the reflected signal can determine the lateral extent of the defect using the 6 dB drop method [34]. By using arrays of transducers it is possible to locate the defects more precisely by comparing the time of flight of the reflected signal for different elements in the array. In addition to simple flaw detection other more advanced techniques exist to determine the size of defects within the sample, such as time of flight diffraction (ToFD) [30], where the diffraction from the tips of cracks is used to determine the size and position of defects with an extremely high level of accuracy.

Another application of bulk wave ultrasonics is for the characterisation of stress within a sample, which is typically done via non-linear analysis of super-harmonics of a generated wave [4, 35]. By investigating the intensity of the second order harmonics it is possible to detect and quantify the material fatigue in metal samples, before cracks or other defects begin to form in the sample.

1.2.5.2 Guided wave methods

Guided waves can be used for many of the same applications as bulk waves, such as flaw detection or measurements of non-linearity [32,36], although there are advantages and disadvantages to their use. Due to the confined nature of guided waves they can propagate over much greater distances than bulk waves, in some cases over a kilometre [37], and this gives them a distinct advantage in being able to inspect large areas quickly and remotely. However, this capability comes at a cost, in that guided waves are often less effective at locating and sizing defects when compared to bulk wave methods. A further disadvantage of guided waves is that the signals received are often complicated by the presence of multiple wavemodes, due to the existence of multiple solutions to the guided wave equations (section 2.2) [38]. There are two common approaches to overcoming this problem, either through physically optimising the transducers to preferentially generate and detect a single wavemode [39], or through advanced signal processing which is capable of decomposing the various wavemodes [40].

Flaw detection using guided waves is a common application, and can be performed in many different sample geometries, such as pipes [41,42], railway tracks [43,44], bars and wedges [45–47]. This can be done using a single transducer where the reflections from the sample are analysed [42], or by comparing the generated signal to the detected signal by a different transducer, and analysing the effect the sample has on the transmission of the wave [41,43]. Although guided wave inspections are typically limited in their ability to characterise defects, short range inspections in the near-field of the guided wave allow greater opportunities for characterisation of defects, in both their size and orientation [43, 46]. By analysing the frequency of the wave which is transmitted past the defect it is possible to estimate its vertical extent, while the enhancement of either of a laser generated guided wave as either the laser source or laser interferometer passes over the defect can provide information about its angle to the surface [48]. The sensitivity of guided wave inspections in defect characterisation can also be improved by applying tomographical reconstruction [49, 50], which operates in the same way as CT scanning, where the combination of multiple views through a sample allow much more precise imaging of defects than available through conventional guided wave inspections.

As with bulk waves, surface guided waves have also been used for non-linearity measurements in order to determine the effects of stress on samples [32, 51], these studies present two different approaches to non-linear measurements. In [32] a low frequency "pump" wave is used to load the sample while a high frequency wave is used to interrogate it for non-linear response; the low frequency wave introduces a change in the velocity of the material by introducing a non-linearity into the sample. The change in the velocity of the high frequency probe wave is then used to make an assessment of the non-linearity in the sample. In [51] a single wave is used, where the ratio of the amplitude of the first and second order harmonics for the narrow-band Rayleigh wave is used to asses the non-linearity of the sample. In both cases the acoustic non-linearity of the sample can be related to either the stress or strain in the sample, allowing a measurement of the fatigue damage before any macroscopic cracks are present.

Lamb waves, a type of guided wave [38, 52, 53], have been used to measure the thickness and material properties of metal sheets [54–61]. The methods used in these studies are highly diverse, with some using narrow-band signals [54, 56, 58, 60], while others use broadband signals [55, 57, 59, 61]. Both of these methods aim to obtain the dispersion curves of the Lamb waves in the samples experimentally, either using measurements from multiple positions to calculate a two-dimensional fast Fourier transform for the broadband techniques, or by conducting multiple individual narrow-band measurements. The theoretical dispersion curves are calculated by varying the transverse and longitudinal velocities as well as the thickness until the calculated dispersion curves are sufficiently close to the experimental curves. These iterative methods can provide estimations for the both the sound velocities in the sample, as well as the thickness, but can be time consuming to implement. In addition to the amount of time required to successively iterate the dispersion curves, time must be taken either to generate multiple single frequency scans which are used in the narrow-band measurements to calculate the dispersion curves experimentally, or to perform measurements at multiple positions, necessary to perform the 2D-FFTs, which are typically used in the broad-band measurements [59].

One of these studies explores an approximation that gives a direct relationship between the wave velocities of Lamb waves within a sample and the thickness of the sample [55]. By using approximate values for the velocities of the fundamental Lamb waves at low values of frequency thickness an equation is given which relates these velocities to the frequency of the Lamb waves and the thickness of the sample. This is described mathematically and discussed in detail in section 2.2.3, where a critical review of this method is also given, and is the basis for the research into thickness measurements using Lamb waves presented in this thesis. A similar technique, using the dispersive properties of SH guided waves [62] to perform calibrationless thickness measurements, has also been reported. Thickness measurements of samples below 1 mm in thickness have not been reported, although the error is reported to increase for thinner samples or measurements at longer wavelengths [62].

1.2.5.3 Transduction of guided waves

A number of methods exist for generating and detecting ultrasound, and these are discussed in this section, with a particular focus on their application to generate Lamb waves. The first such method is that of piezoelectric transducers, which rely on the piezoelectric effect discovered in quartz by Jacques and Pierre Curie [63]. Piezoelectrics are a class of crystals which undergo strain when a voltage is applied to them [64]. This is due to the noncentrosymmetric nature of these crystals, where the arrangement of the atoms in the crystal lattice creates an electric dipole which shifts when exposed to an electric field. Man-made piezoelectric materials, such as lead zirconium titanate (PZT), often belong to a class of crystals known as ferroelectrics. The piezoelectricity in these crystals arises from a dipole present in the crystal, where one of the atoms of which the crystal is composed is not in the centre of the crystal [64]. However, like the ferromagnetic materials after which they have been named, ferroelectric materials only retain their properties up to a maximum temperature, the Curie temperature (T_c), limiting the temperature range in which the transducer can be used effectively [65].

Piezoelectric transducers have been used in a number of studies using to generate and detect Lamb waves in metal sheets [41, 54, 58, 61], although the precise method of coupling of these transducers to the sample does vary. The method of coupling of these transducers to the sample is important as the solutions for the characteristic equations of the Lamb waves (section 2.2) are reliant upon the assumption that the boundary conditions of the plate are completely free. This has been done using liquid couplant [54, 58], as well as by examining the sample in an immersion tank [61]. A further option is that of dry coupled transducers [41, 66], where the transducer is mechanically clamped to the surface of the sample, in this case with steel or brass shim between the sample and transducer, in order to couple ultrasound efficiently into the sample. These contact methods typically offer more efficient transduction than non-contact methods [67], resulting in higher signal to noise ratios. However, when generating and detecting ultrasound in very thin samples non-contact methods are often preferred as they avoid altering the sample which is being measured due to surface loading [68]. Non-contact measurements also allow the measurements to be performed in hostile environments, where piezoelectric transducers are unsuitable [8].

One non-contact method is that of laser based ultrasonics [69]. Although a piezoelectric transducer is reversible, that is the detection method is the inverse of the generation method, this is not true for lasers, which require two separate systems for generation and detection. For generation a high power laser is directed at the sample in order to generate ultrasound. In general this can be done in one of two ways; with a sufficiently powerful laser the point on the surface of the sample on which the laser is focused is ablated and becomes a plasma, which rapidly expands and impacts the sample, creating an ultrasonic pulse. By reducing the power of the laser, the sample at the focal point can simply be heated, and the corresponding thermal expansion provides the ultrasonic pulse [69]. These methods of generation are known as the ablative and thermoelastic regimes respectively. Detection of ultrasound using lasers in academia is typically achieved using an interferometer, as discussed in [59], although vibrometers can also be used [70], and are more common in industrial applications. These systems typically detect the vertical displacement of the surface of a sample by measuring the effect the moving sample has on the phase of a beam of light generated by a laser, although methods also exist to detect vibration in the plane of the sample as well [71]. Laser ultrasound systems can operate at large distances from the samples which they inspect, making them ideal for remote applications where the conditions which the sample is under are inimical to other transducers [72], and have been used to generate and detect Lamb waves [55–57, 59, 60, 73]. Laser based ultrasonic systems have also been used to perform inspections in inimical environments, such as the thickness measurements of steel at temperatures of up to 1250 $^{\text{o}}$C [74].

Another method of generating and detecting Lamb waves in a non-contact manner in electrically conducting samples is through the use of EMATs [49, 75–77]. These are described in detail in section 2.3. but typically consist of a coil of wire which is placed in proximity to a sample, and a magnet which is placed immediately behind the coil. The typical method of transduction for an electrically conductive sample is the Lorentz force, where applying a magnetic field and a current to a sample results in the generation of a force orthogonal to both the current and the magnetic field. In magnetic samples an additional generation mechanism is present, magnetostriction, although usually the Lorentz force still remains the main method of coupling ultrasound into the sample [78]. Although EMATs cannot operate at the same distance from the sample as lasers, they can still operate remotely, although the efficiency of the transducer decreases rapidly with increasing lift-off. Another consequence of increasing the lift-off of a transducer is that this can effect the phase of the signal recorded by the transducer [79], which can lead to errors in experimental measurements if the separation between the sample and the transducer is not kept constant. EMATs are considerably less expensive than lasers, and the configuration of the coil, static magnetic field, and current pulse can be designed to produce narrow-band signals.

1.3 Profile measurements

The second research project in this thesis concerns the measurement of the profile of a sample along its length, aiming to detect changes in the sample height of 1 µm over a dynamic range of at least 2 mm. Accurate surface profile measurements are an important part of the quality assurance of many components, and this is a field which has relevance in both NDE and metrology [80, 81]. These profile measurements are used in a number of industries for detection of warping or bending of manufactured components [7], as well as to measure structures in situ, such as continuity of road surfaces [82].

1.3.1 Research problem

The measurement of profiles is a well discussed field and several competing technologies exist. Due to the commercially sensitive nature of this work the exact nature of the research problem is discussed in detail in chapter 7. However, the research problem distils to a one dimensional measurement of the surface profile of a metal sample, where the electrical properties of the sample are significant as they allow electromagnetic methods to be considered. The accuracy of the system must be sufficient to resolve changes in lift-off of 1 µm, while operating over a range of at least 2 mm. While this can be achieved using existing contact measurements, a non-contact method is preferred to preserve the surface finish of the sample under test.

1.3.2 Contact measurements

Contact measurements are often made using a stylus or tip with a sharp point, which is put into contact with the surface of the sample, and the vertical movement of the tip is recorded as the tip is actuated across the surface of the sample [83]. This vertical motion is then combined with the positional information of the probe to form a surface profile of the sample. These measurements are commonly used in industry to measure surface profiles due to the simple nature of the measurement, and are the subject of industrial standards [84]. A limitation of these contact measurements can arise from the jitter in the stylus as it moves across the surface of the sample, although this can be alleviated by applying filters to the acquired data [83]. Due to the contact between the tip and the sample, the tip can also cause damage the surface finish of the sample, particularly where the finish is highly polished.

A similar, but significantly more precise method of determining the surface profile is by using atomic force microscopy (AFM), which allows resolution of the surface profile to an atomic scale [85]. It should be noted that although the AFM can be used as a contact measurement, it can also be used in a non-contact mode as well, where the van der Waals force from the surface of the sample acts on the tip, causing it to deflect without contact [86]. However, the limited scanning area and delicacy of the system preclude the use of AFM in almost all industrial environments. [7]

1.3.3 Optical measurements

Optical measurements are also used extensively to perform profile measurements, as well as to determine the surface roughness of samples [87]. This can be done in a number of ways, such as interferometry or by pattern projection [7, 88]. These methods often have a very high throughput, allowing large areas to be inspected and profiled in very little time. In one study, a pattern projection method, where a known pattern of light is applied to a sample of unknown topography using a projector in order to measure the deviation of the pattern and calculate the topography, was used to calculate the topography of silicon wafers to an accuracy of 50 μm. This accuracy was achieved using a system which could analyse over 2000 silicon wafers per hour, making it extremely useful for on-line monitoring [7].

The ability to scan large areas in one measurement is a significant advantage for pattern projection type measurements over those relying on stylus based contact measurements or those using interferometry, as these latter methods must be raster scanned over the desired area to be inspected. The disadvantage of these optical systems is that the surface condition of the sample is key to the performance of the system, where interferometry often requires a reflective sample in order to function with high accuracy.

1.3.4 Electromagnetic methods

Electromagnetic methods can also be used to perform profile measurements, by considering that the interaction of an electrically conductive sample with a probe is directly affected by the distance between the probe and the sample. This dependence allows the lift-off of the probe from the sample to be determined, and if the probe is maintained at a fixed height above the sample, allows the profile to be calculated. There are two main methods of profile measurements using electromagnetic sensors; capacitive measurements and inductive measurements, and each will be discussed in the following sections.

1.3.4.1 Capacitive methods

Capacitive measurements are based on the change in the capacitance of a measurement probe [1]. In the simplest possible case for a probe used to measure lift-off, the conductive sample acts as one electrode while a metal plate on the probe acts as the other, effectively creating a capacitor between the probe and the sample [14]. The capacitance of this probe will vary with the lift-off of the probe,

$$C = \frac{A\varepsilon}{d}, \tag{1.2}$$

where A is the area of the metal plates, ε is the permittivity of air, and d is the lift-off between the probe and the sample. However, in order to achieve a high spatial resolution the capacitive plate of the probe must be as small as possible, which increases the dominance of edge effects on the measurement [89]. Other capacitive probes can achieve greater range and sensitivity by utilising these fringe effects by sensing the change in capacitance between two concentric rings [90]. This proximity measurement, while extremely accurate over small values of lift-off, becomes less accurate as the lift-off increases beyond 200 µm.

1.3.4.2 Inductive methods

Inductive methods involve measuring a change in the inductance of a coil which is in proximity to an electrically conductive sample when an alternating current is applied to the coil. This change is caused by the time varying magnetic field in the coil inducing an electrical current in the surface of the sample, known as an eddy current [27,91]. The inductive coupling between the coil and the sample will cause a change in the impedance of the coil as the lift-off between the sample and the coil is altered, where this impedance change can be quantified by taking the ratio of the voltage across the coil to the current flowing through the coil [92]. The relationship between lift-off and impedance change is discussed in greater detail in section 2.5.

Typically this variation in the impedance of the coil with lift-off is an undesired effect, which interferes with the use of eddy current measurements to detect defects in samples [93]. Several studies have been performed aimed at reducing or eliminating this effect [94,95]. However, for the application of profile measurements this effect is key to determining the lift-off of samples from the eddy current probe. Measurements of the lift-off for both copper and aluminium sheets have previously been conducted simultaneously with measurements of the sheet thickness, typically to accuracies of greater than 96 % at lift-off ranges of up to 2 mm by investigating the change in the impedance across the entire frequency range of a coil [20]. In a more recent study by the same authors both the accuracy and range of the measurement have been improved, with accuracies of greater than 98 % achieved at lift-off ranges of up to 4 mm on aluminium [96].

Due to this large operational range, combined with the promising accuracy of the measurement and the relative insensitivity of the measurement to the surface condition of the sample, an eddy current based system was chosen to be developed into a measurement tool capable of meeting the requirements of the industrial research. The resolution in the lift-off measurements which these probes are capable of detecting must be improved to a level of 99.95 % in order to detect a 1 µm change at a lift-off of 2 mm. Additionally, the measurement system developed must be robust enough to work effectively in an industrial environment.

A brief summary of the methods considered is shown in table 1.1, where the eddy current approach overcomes the limitations of the other techniques.

Technique	Benefits	Limitations
Contact	Direct measurement of sample profile	Can cause damage to sample
Optical	Extremely high resolution measurements	Requires clean surface finish
Capacitive	Very high sensitivity to lift-off	Very short operating range
Inductive	High operating range	Susceptible to material variations

Table 1.1: Summary of the different approaches considered for performing profile measurements.

Chapter 2

Theory of high precision measurements

This chapter covers the theories behind the research described in this thesis, including the ultrasonic generation and propagation of Lamb waves, the equivalent circuit model of eddy current interaction, and an overview of some of the signal processing techniques used during the data processing. Due to the transition between physical and electrical phenomena there are some small changes in the notation between sections 2.1 and 2.2 covering ultrasonics, and sections 2.3 and 2.5 covering EMATs and eddy currents. Where such changes in notation occur it will be explicitly noted.

2.1 Ultrasonic Waves

Ultrasonic waves are mechanical waves which propagate through a material and have a frequency higher than the range of human hearing, typically considered to be frequencies greater than 20,000 Hz [27]. These waves can be used in numerous different ways for non-destructive testing, as discussed in section 1.2.5, although the type of ultrasonic wave used depends on the exact application [4, 6, 30]. Ultrasonic waves can be separated into two different categories; bulk waves and guided waves. Bulk waves are those where no special consideration is given to the boundary conditions of the material in which the ultrasonic waves propagate, although these boundary conditions can be considered for the reflection and transmission of the bulk waves from interfaces, or their interactions with defects [97]. Bulk waves themselves can have two different types of oscillation; longitudinal, where the particle motion is parallel to the propagation of the wave, and transverse, where the particle motion is orthogonal to the wave propagation [53]. Guided waves follow the same constituent equations as bulk waves [38], although the nature of the solutions to the wave equations will change depending on the boundary conditions which define the guided wave (discussed in section 2.2).

This section focuses on the mathematical description of an ultrasonic wave in an elastic solid, initially considering bulk waves. The methods of using bulk waves to perform thickness measurements are also discussed. In addition, the effect of boundary conditions on the propagation of ultrasonic waves in thin sheets is considered as part of the mathematical description of Lamb waves in section 2.2, while their applications to thickness measurements are examined in section 2.2.3.

2.1.1 Propagation of ultrasound in isotropic solids

When considering the propagation of ultrasound in a solid medium, the simplest case is that of an isotropic and homogeneous solid with no boundary conditions. In such a material the speed of propagation is independent of the direction due to the isotropy of the medium, and the homogeneity ensures that the propagation behaviour is the same regardless of location [98]. Another consideration in the mathematical description of the propagating ultrasound is the type of deformation caused by the travelling wave. Ultrasound waves used in NDE are, by definition, of relatively small amplitudes, such that the particle motion of the solid does not exceed the elastic limit. This is important as any violation of Hooke's law would destructively deform the sample under examination [2]. In this section the subscript tensor notation with the summation convention is used, commonly known as Einstein notation [99], and partial derivatives of tensors with respect to spatial dimensions are expressed in full, e.g. as $\frac{\partial u_i}{\partial x_j}$ rather than $u_{i,j}$. Vectors are expressed using arrow notation, $\vec{u}$, and differentials with respect to time are also expressed in full in both tensor and vector notation, $\frac{\partial u_i}{\partial t}$ or $\frac{\partial^2 \vec{u}}{dt^2}$.

2.1.1.1 Relationship between stress and strain

The propagation of ultrasonic waves in an isotropic solid is governed by the relationship between the stress and strain in the solid. Due to the small amplitudes of ultrasonic waves used for NDE, the relationship between the strain and the particle displacement can be written in the following form [98],

$$\varepsilon_{ij} = \frac{1}{2}\left(\frac{\partial u_i}{\partial x_j} + \frac{\partial u_j}{\partial x_i}\right), \tag{2.1}$$

where ε_{ij} is the tensor strain, u is the particle displacement and x is the direction of the strain. The indices i and j represent the three cardinal directions in a Cartesian coordinate system. This formulation of the strain tensor is known as the Cauchy strain tensor, and can be expanded to the following form for a three dimensional system,

$$\varepsilon_{ij} = \begin{pmatrix} \frac{\partial u_1}{\partial x_1} & \frac{1}{2}\left(\frac{\partial u_1}{\partial x_2}+\frac{\partial u_2}{\partial x_1}\right) & \frac{1}{2}\left(\frac{\partial u_1}{\partial x_3}+\frac{\partial u_3}{\partial x_1}\right) \\ \frac{1}{2}\left(\frac{\partial u_2}{\partial x_1}+\frac{\partial u_1}{\partial x_2}\right) & \frac{\partial u_2}{\partial x_2} & \frac{1}{2}\left(\frac{\partial u_2}{\partial x_3}+\frac{\partial u_3}{\partial x_2}\right) \\ \frac{1}{2}\left(\frac{\partial u_3}{\partial x_1}+\frac{\partial u_1}{\partial x_3}\right) & \frac{1}{2}\left(\frac{\partial u_3}{\partial x_2}+\frac{\partial u_2}{\partial x_3}\right) & \frac{\partial u_3}{\partial x_3} \end{pmatrix}. \tag{2.2}$$

The Cauchy strain tensor is symmetric and hence $\varepsilon_{ij} = \varepsilon_{ji}$. This stain tensor is related to the stress tensor σ_{ij} for a general material using,

$$\sigma_{ij} = c_{ijkl}\varepsilon_{kl}, \tag{2.3}$$

where the tensor c_{ijkl} is a fourth order tensor known as the stiffness tensor. When considering an isotropic material this equation can be greatly simplified to [38],

$$\sigma_{ij} = \lambda\varepsilon_{kk}\delta_{ij} + 2\mu\varepsilon_{ij}, \tag{2.4}$$

where λ and μ are the two Lamé coefficients of the material [98]. The term ε_{kk} is known as the dilatation [38,98], where the repeated index k denotes that only the trace of the tensor ε_{ij} is being considered. The dilatation is also represented by e in some literature [53,98], and is the relative volume change of the material under strain, and is variously defined as,

$$e = \frac{\Delta V}{V_0} = \varepsilon_{ij}\delta_{ij}. \tag{2.5}$$

where ΔV is the change in volume due to the strain in the material, V_0 is the original volume and δ_{ij} is the Kronecker delta. Equation 2.4 can then be rewritten substituting the definition of the strain from equation 2.1,

$$\sigma_{ij} = \lambda\frac{\partial u_k}{\partial x_k}\delta_{ij} + \mu\left(\frac{\partial u_i}{\partial x_j} + \frac{\partial u_j}{\partial x_i}\right). \tag{2.6}$$

2.1.1.2 Dynamic motion in elastic media

Thus far the relationship between stress and strain has been considered only for the static case, giving no time dependence in equation 2.6. However, the formulation of Hooke's law for an isotropic solid in equation 2.6 will also be valid in a dynamic, time-varying, case, provided that the elastic limit of the material is not exceeded [98]. In order to derive the equations governing the behaviour of ultrasonic waves in a medium, the tensor form of Newton's third law of motion is considered [53],

$$\frac{\partial \sigma_{ij}}{\partial x_j} + \rho f_i = \rho \frac{\partial^2 u_i}{\partial t^2}, \tag{2.7}$$

where ρ is the density and f_i is the body force per unit mass. The body forces encompass gravity and other forces that act throughout the material, and for a material in a state of general equilibrium this can be ignored. By omitting the body forces term this equation can be rewritten, substituting the relationship between the stress tensor and the particle motion given in equation 2.6, to arrive at the Navier-Cauchy governing equation, which can be expressed in tensor form as [38, 53],

$$\mu \frac{\partial^2 u_i}{\partial x_j^2} + (\lambda + \mu) \frac{\partial^2 u_j}{\partial x_j \partial x_i} \quad = \quad \rho \frac{\partial^2 u_i}{\partial t^2}. \tag{2.8}$$

As this equation consists only of first order tensors it can also be denoted using vector notation, where the del operator, ∇, is used in place of spatial differentials,

$$\mu \nabla^2 \vec{u} + (\lambda + \mu) \nabla \nabla \cdot \vec{u} = \rho \frac{\partial^2 \vec{u}}{dt^2}, \tag{2.9}$$

allowing a simpler expression of the equation. In order to further simplify the equation, the vector $\vec{u}$ can be subjected to Helmholtz decomposition in order to be stated in terms of a vector potential and a scalar potential [97],

$$\vec{u} = \nabla \phi + \nabla \times \vec{\psi}. \tag{2.10}$$

This decomposition allows the Navier equation to be rewritten in terms of two uncoupled potentials, representing the scalar, or dilatational, and the vector, or distortional, components of the vector$\vec{u}$ [53],

$$\nabla \left[(\lambda + 2\mu) \nabla^2 \phi - \rho \frac{\partial^2 \phi}{\partial t^2} \right] + \nabla \times \left[\mu \nabla^2 \vec{\psi} - \rho \frac{\partial^2 \vec{\psi}}{\partial t^2} \right] = 0. \tag{2.11}$$

The only valid, non-trivial, solutions of this equation require that both the scalar and vector potential components of 2.11 are equal to zero, which allows the formulation of two separate wave equations,

$$(\lambda + 2\mu) \nabla^2 \phi \quad = \quad \rho \frac{\partial^2 \phi}{\partial t^2} \tag{2.12}$$

$$\mu \nabla^2 \vec{\psi} \quad = \quad \rho \frac{\partial^2 \vec{\psi}}{\partial t^2}. \tag{2.13}$$

The wave described by equation 2.12 is the dilatational wave, which alters the volume of the material as it propagates, travelling as a wave with alternating regions of compression and rarefaction in the same direction as the propagation [53]. This wave is more commonly known as the longitudinal wave, and its propagation velocity can be determined from equation 2.12 to be,

$$C_L = \sqrt{\frac{(\lambda + 2\mu)}{\rho}}, \tag{2.14}$$

where C is the velocity of the wave and the subscript L denotes the longitudinal mode [38]. The velocity of the distortional wave, which is more commonly known as the transverse wave, can also be calculated from its governing equation, equation 2.13, to be

$$C_T = \sqrt{\frac{\mu}{\rho}}, \tag{2.15}$$

where the subscript T denotes the transverse velocity in a material.

This simple derivation of the propagation velocities of the longitudinal and transverse bulk waves is only valid when considering isotropic media, as in an anisotropic medium the stiffness tensor (equation 2.3) is considerably more complex. This additional complexity would add a directional component to the derived wave velocities, where the velocity along each of the principal directions of the material would be different [97]. The materials considered in this research can be treated as isotropic, and as such this extra level of complexity can be ignored.

2.1.1.3 Phase and group velocity

A propagating wave has two different velocities which represent different information about the wave, a group velocity and a phase velocity, although these velocities can be equal [100]. The group velocity is the easiest to conceptualise, and is taken to be the propagation velocity of the wave, or the velocity at which energy is transferred by the wave. This is shown in figure 2.1, where the propagation of energy within the wave is given by the propagation of the envelope of the wave and is usually measured by the arrival time of the wave. The phase velocity is the rate at which the phase of the wave propagates, i.e. the rate at which a single peak or trough in the wave packet travels as the wave propagates, and this may be different from the group velocity [101]. This concept is visualised in figure 2.1, where the phase velocity is shown by the rate of propagation of a single peak within the envelope of the wave.

Equations 2.14 and 2.15 describe the propagation velocities in an isotropic material of the longitudinal and transverse waves respectively, and hence are the group velocities of these waves.

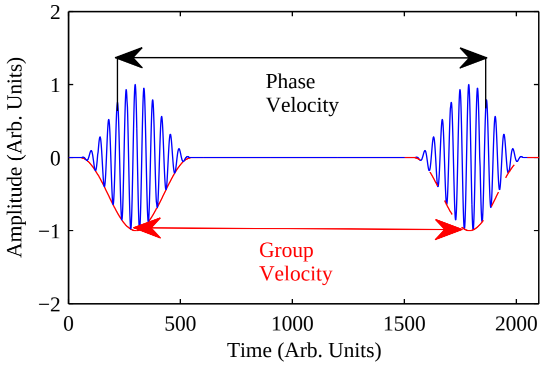

Figure 2.1: Representation of the difference between the group velocity, which measures the rate at which the envelope or energy of a wave, shown in red, propagates, and the phase velocity, which measures the rate at which a single peak within the wave packet propagates.

The group and phase velocities can be written as C_g and C_p where the subscript indicates the group or phase, and the mathematical description of the group and phase velocities is

$$C_g = \frac{\partial \omega}{\partial k}, \tag{2.16}$$

$$C_p = \frac{\omega}{k}, \tag{2.17}$$

where ω is the angular frequency of the wave and k is its wavenumber [100]. From equations 2.14 and 2.15 it can be seen that the group velocities of the bulk waves do not depend on the frequency of the wave, but only on the material in which they propagate. Thus the group and phase velocities of the waves are equivalent, and these waves are non-dispersive. The distinction between the phase velocity and the group velocity is extremely important in the discussions of dispersive waves, such as Lamb waves.

2.1.2 Using bulk waves for thickness measurements

The simple relationship between the bulk wave velocities and the properties of the material in which they propagate make them an ideal candidate for performing thickness measurements [2,6]. Additionally, the non-dispersive nature of the waves greatly simplifies the measurements made, as the velocities are independent of the frequency of the wave for an isotropic and homogeneous sample, such as typical metallic materials like steel or aluminium, which allows the results of the inspection to be independent of the frequency at which the inspection was conducted.

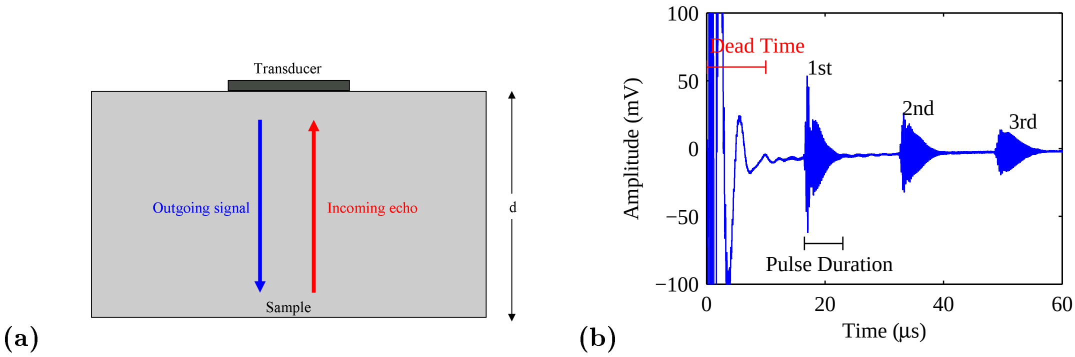

Figure 2.2: (a) A schematic diagram of a pulse echo thickness measurement, and (b) an example A-scan measured using this arrangement.

2.1.2.1 Time of flight measurements

Thickness measurements using time of flight are the simplest form of ultrasonic thickness measurement, and rely upon calculating the path length of an ultrasonic wave propagating in a sample using the time of flight of the wave and prior knowledge of the wave velocity [2]. A pulse-echo arrangement for measuring thickness is shown in figure 2.2 (a), where the transducer acts as both generator and detector, transmitting ultrasound into the sample and recording the returning echoes from the back wall of the sample. An example of the data recorded using such an arrangement is shown in figure 2.2 (b), using an undamped piezoelectric transducer excited with a broadband source to measure the thickness of an aluminium sample. For the experimental set-up shown in the figure, the thickness of the sample, d, can be determined from the arrival time of the ultrasound wave at the transducer,

$$d = \frac{Ct}{2}, \tag{2.18}$$

where t is the measured transit time of the ultrasonic wave. Ultrasonic thickness measurements performed in this way sometimes examine only the first back wall echo [6], identified in figure 2.2 (b), although it is common to use multiple subsequent echoes to increase the reliability of the measurement [102]. The pulses shown in figure 2.2 (b) are elongated in time due to the ringing in the undamped transducer, and the arrival time for these waves would be obtained through thresholding, determining the first point in time at which the returned signal exceeded a certain value [2]. However, in very thin materials, less than 1 mm for example [6], the transit time of the wave can be sufficiently short that the reflected signal can arrive while the generation pulse of the transducer is still present, distorting the A-scan, labelled in figure 2.2 (b) as the dead time, although this can often be known as the dead zone. This limitation can be avoided by using a delay line, which will separate the first back wall reflection from the generation signal in time, allowing thickness measurements on thinner samples. These delay lines often take the form of a physical rod, or an immersion tank, in industrial settings [6], although the characteristics of the delay line must be well understood.

There is an additional limit on the lowest thickness of a sample which can be measured using time of flight measurements, which is the ability to resolve successive back wall echoes. This is a distinct problem from the arrival of the first back wall echo in the dead time, and cannot be overcome using a delay line. In figure 2.2 (b) the successive echoes are clear and distinct, but in a thinner sample these echoes may start to merge, which will make it impossible to measure the thickness of the sample in the time domain. From this the limit on the thickness and pulse duration is set, such that the duration of the ultrasonic signal, labelled in figure 2.2 (b), must be less than or equal to the propagation time of one round-trip of the wave through the sample. If the ultrasonic wave consists of one cycle at the generated frequency, which is not wholly realistic, as discussed later, then the minimum measurable sample thickness is given by,

$$d_{min} = \frac{C}{2f}, \tag{2.19}$$

where central f is the frequency of the generated ultrasound. Hence increasing the frequency will reduce the minimum thickness of the sample which can be measured.

A reduction in the minimum measurable thickness can also be achieved by using transverse waves rather than longitudinal waves, which travel more slowly than longitudinal waves. This increases the time taken for the ultrasound to propagate through the sample, allowing thinner materials to be measured at the same frequency. However, transverse waves can be difficult to generate effectively using piezoelectric transducers due to the difficulty of coupling shear forces through a fluid medium [2]. Another method for reducing the minimum thickness which can be measured is by shortening the length of the ultrasonic pulse, for example by using broadband excitation [103], which is typically used in industry. These excitations are similar to a Dirac impulse, with broad frequency content occurring in a small window in the time domain. This effectively allows equation 2.19 to be superseded, as the minimum measurable thickness will be related to both the pulse width, t_p, and the speed of sound in the material,

$$d_{min} = \frac{Ct_p}{2}. \tag{2.20}$$

A further consideration, related to equation 2.19, is that this assumes a perfect response time from the measurement system, in addition to infinitely high resolution in the time domain, neither

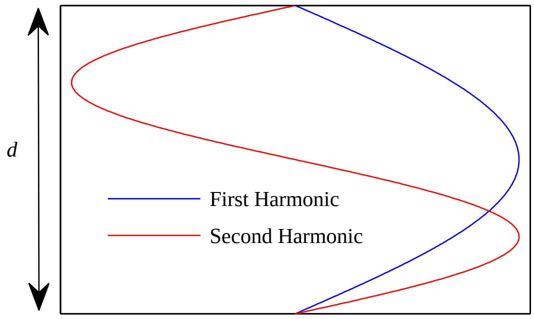

Figure 2.3: Through-thickness resonances for the first and second harmonics.

of which are experimentally achievable [6]. Any delay in the response of the system will affect the measurement of the thickness if just the first backwall echo is used (figure 2.2 (b)), as any delay will artificially increase the perceived thickness of the sample. A constant delay in the measurement system can be overcome by measuring the time between successive backwall echoes, as the delay will be applied to each echo and will be ignored when looking at the differential time between echoes. However, for increasingly short pulses in increasingly thin materials the data acquisition hardware may have insufficient bandwidth to distinguish between echoes [104]. Thus the actual minimum measurable thickness will be limited by the available hardware, as well as the physical constraints described in equations 2.19 and 2.20.

2.1.2.2 Measurements in the frequency domain

In order to overcome some of the limitations of experimental hardware, thickness measurements can instead be performed in the frequency domain, by measuring the resonant frequency of a through-thickness mode of the sheet [68, 105], i.e. the frequency of the standing waves that occur through the thickness of the sheet. The first and second harmonics of the through-thickness mode for a sample of thickness d are shown in figure 2.3. This method has been implemented in two different ways, using a frequency scanning approach [68], and using a broadband measurement system [105]. The relationship between the resonant frequency of a through thickness mode and the thickness of the sample is described by

$$d = \frac{C}{2f_0}, \tag{2.21}$$

where f_0 is the frequency of the fundamental through thickness mode, and the accuracy of the measured thickness is determined by the accuracy with which the resonant frequency can be identified.

In the frequency scanning approach a long pulse of energy at a given frequency is introduced to the sample using an electromagnetic acoustic transducer, and the vibration of the plate at that frequency is recorded using the same transducer. In these measurements an EMAT is used to avoid altering the resonance of the sample by loading the surface, as would occur when using a piezoelectric transducer [68,105]. By recording the response of the plate at a number of frequencies a plot of the resonance modes of the plate can determined. Equation 2.21 can then be used to determine the thickness of the sample [68], after identifying the frequency of the first resonance mode. In the broadband approach a high bandwidth pulse is introduced to the sample using an EMAT, which then records the response of the sample. The A-scans are windowed to exclude the dead time caused by the generation pulse, and then analysed using a Fourier transform. The peaks in the Fourier transforms correspond to the through-thickness resonance modes of the plates, and the frequency of the first resonance mode can then be used with equation 2.21 in order to calculate the thickness of the sample [105].

This is a general technique, and can be applied to the measurement of coatings and substrates as well as single materials [105]. However, this method has the same fundamental limitation as the time domain measurements in section 2.1.2.1, in that the accuracy of the measurement is dependent on the accuracy to which the speed of sound in the material is known, where this can be affected by the temperature or the composition of the sample [38,106].

2.2 Lamb Waves

Lamb waves are a type of ultrasonic wave that propagate in thin materials, where the wavelength is comparable to the thickness of the propagating medium, and result from the superposition of multiple reflected bulk waves which are confined in a thin waveguide. These waves were first described by Lamb in 1917 [107], and have been the subject of a great deal of research for application in both thickness measurements [54–61], and flaw detection [36, 47]. Although the multi-modal nature of Lamb waves is extremely complex, the characteristic equations which describe them can be derived from applying the boundary conditions for a thin sample with traction-free surfaces to equations 2.12 and 2.13.

2.2.1 Deriving the characteristic equation

In order to derive a characteristic equation to describe Lamb waves the propagation of both longitudinal and transverse waves are considered in an infinite, thin plate with traction free surfaces [38,53,97]. This is essentially a thin plate that is infinitely large in the spatial dimensions

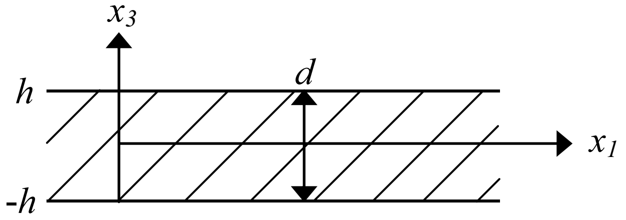

Figure 2.4: Schematic diagram of an infinite plate in which the solution to the Lamb wave equation will be considered.

other than thickness, and is surrounded by vacuum. The infinite extent of the plate allows edge effects and reflections to be ignored, while the condition of existing in a vacuum ensures that there is no coupling between the plate and the surrounding medium, i.e.. that no energy is lost from the plate. The simple case considers a plane strain within the sheet, such that the complexity of the model can be reduced to two dimensions; x_1, an infinite dimension of the direction in which the Lamb wave propagates, and x_3, the finite dimension which represents the thickness of the plate [38], as shown in figure 2.4. The assumption of a plane strain is valid where the width of the sheet in the x_2 direction is much larger than the wavelength of the Lamb waves, as is the case here. Under this assumption the wave equations for longitudinal and transverse waves given by equations 2.12 and 2.13 can be expressed as

$$\frac{\partial^2 \phi}{\partial x_1^2} + \frac{\partial^2 \phi}{\partial x_3^2} = \frac{1}{C_L^2} \frac{\partial^2 \phi}{\partial t^2} \tag{2.22}$$

$$\frac{\partial^2 \vec{\psi}}{\partial x_1^2} + \frac{\partial^2 \vec{\psi}}{\partial x_3^2} = \frac{1}{C_T^2} \frac{\partial^2 \vec{\psi}}{\partial t^2}, \tag{2.23}$$

where the velocities of the longitudinal and transverse waves are used in place of the Lamé parameters for simplicity. The solutions to these equations are assumed to consist of two separate components; a propagating wave travelling in the direction x_1, of the form $e^{i(kx_1 - \omega t)}$, and a standing wave through the thickness of the sheet, described by the functions $\Phi(x_3)$ and $\Psi(x_3)$ for the longitudinal and shear waves respectively [38, 97]. Combining these two components, the total wave equations in this case are,

$$\phi = \Phi(x_3)\, e^{i(kx_1 - \omega t)} \tag{2.24}$$

$$\left|\vec{\psi}\right| = \Psi(x_3)\, e^{i(kx_1 - \omega t)}. \tag{2.25}$$

The standing waves through the thickness of the sheet are often referred to as transverse resonance modes [38]. By substituting the proposed solutions into equations 2.22 and 2.23 the transverse resonance modes can be shown to have the form

$$\begin{aligned}\Phi\left(x_3\right) &= A_1\sin(px_3)+A_2\cos(px_3) && (2.26)\\ \Psi\left(x_3\right) &= B_1\sin(qx_3)+B_2\cos(qx_3) && (2.27)\end{aligned}$$

where the coefficients A_1, A_2, B_1 and B_2 originate from solution of the partial differential wave equations 2.22 and 2.23, and p and q are substitution variables defined as,

$$p^2=\frac{\omega^2}{C_L^2}-k^2,\ \ q^2=\frac{\omega^2}{C_T^2}-k^2. \tag{2.28}$$

The particle displacement can be written in terms of the solutions to the standing modes through the thickness of the sheet, and by considering these particle displacements in conjunction with equation 2.6, the displacements and stresses are

$$\begin{aligned}u_1 &= \frac{\partial\phi}{\partial x_1}+\frac{\partial\vec{\psi}}{\partial x_3}=ik\Phi+\frac{d\Psi}{dx_3}, && (2.29)\\ u_3 &= \frac{\partial\phi}{\partial x_3}-\frac{\partial\vec{\psi}}{\partial x_1}=\frac{d\Phi}{dx_3}-ik\Psi, && (2.30)\\ \sigma_{31} &= \mu\left(\frac{\partial u_3}{\partial x_1}+\frac{\partial u_1}{\partial x_3}\right)=\mu\left(2ik\frac{d\Phi}{dx_3}+k^2\Psi+\frac{d^2\Psi}{dx_3^2}\right), && (2.31)\\ \sigma_{33} &= \lambda\left(\frac{\partial u_1}{\partial x_1}+\frac{\partial u_3}{\partial x_3}\right)+2\mu\frac{\partial u_3}{\partial x_3}=\lambda\left(-k^2\Phi+\frac{d^2\Phi}{dx_3^2}\right)+2\mu\left(\frac{d^2\Phi}{dx_3^2}-ik\frac{d\Psi}{dx_3}\right), && (2.32)\end{aligned}$$

where the factors of ik stem from the differential of the x_1 terms in the time varying component of ϕ and $\vec{\psi}$, $e^{i(kx_1-\omega t)}$, and the exponential is omitted as it present in all of the equations.

The Lamb waves can be separated into two different regimes based on the symmetry of the wave about the centre of the plate, where the symmetry of the particle displacement in the plane of the plate, described by equation 2.29, is considered. For displacement in the plane the wave will be symmetric if the displacement u_1 contains only cosines, and antisymmetric if it contains only sines. This separation of the displacements and stresses into symmetric and antisymmetric components allows the solutions for the transverse resonance (equations 2.26 and 2.27) to be simplified such that $\Phi\left(x_3\right)=A_2\cos(px_3)$ and $\Psi\left(x_3\right)=B_1\sin(qx_3)$ for the symmetric modes. From this the particle displacements and stresses of the symmetric modes can be written as [38, 97],

$$u_1 = ikA_2\cos\left(px_3\right)+qB_1\cos\left(qx_3\right), \tag{2.33}$$

$$u_3 = pA_2\sin(px_3) - ikB_1\sin(qx_3), \tag{2.34}$$

$$\sigma_{31} = \mu\left(-2ikA_2\sin(px_3) + \left(k^2-q^2\right)B_1\sin(qx_3)\right), \tag{2.35}$$

$$\sigma_{33} = -\lambda\left(\left(k^2+p^2\right)A_2\cos(px_3)\right) - 2\mu\left(p^2A_2\cos(px_3) + ikqB_1\cos(qx_3)\right). \tag{2.36}$$

For the antisymmetric modes the solutions for the transverse resonance are $\Phi(x_3) = A_1\sin(px_3)$ and $\Psi(x_3) = B_2\cos(qx_3)$, which allows the particle displacements for these modes to be expressed as

$$u_1 = ikA_1\sin(px_3) - qB_2\sin(qx_3), \tag{2.37}$$

$$u_3 = -pA_1\cos(px_3) - ikB_2\cos(qx_3), \tag{2.38}$$

$$\sigma_{31} = \mu\left(2ikpA_1\cos(px_3) + \left(k^2-q^2\right)B_2\cos(qx_3)\right), \tag{2.39}$$

$$\sigma_{33} = -\lambda\left(\left(k^2+p^2\right)A_1\sin(px_3)\right) - 2\mu\left(p^2A_1\sin(px_3) - ikqB_2\sin(qx_3)\right). \tag{2.40}$$

One of the restrictions on the model under consideration is that the surfaces of the plate are traction free, and hence $\sigma_{31} = \sigma_{33} \equiv 0$ at $x_3 = \pm d/2$, where d is the thickness of the plate and $x_3 = 0$ is the centre of the plate, and the half-thickness is often referred to as h for simplicity. By applying this boundary condition to the equations for stress in the symmetric case, equations 2.35 and 2.36, a pair of simultaneous equations can be formulated. These simultaneous equations for the symmetric case can be represented in matrix form as

$$\begin{bmatrix} -2\mu ikp\sin(ph) & \mu\left(k^2-q^2\right)\sin(qh) \\ \left(-\lambda\left(k^2+p^2\right)-2\mu p^2\right)\cos(ph) & -2\mu ikq\cos(qh) \end{bmatrix} \begin{bmatrix} A_2 \\ B_1 \end{bmatrix} = \begin{bmatrix} 0 \\ 0 \end{bmatrix}. \tag{2.41}$$

This set of simultaneous equations is homogeneous and the absolute values of the coefficients A_2 and B_1 cannot be determined directly from the equations. However, for a homogeneous set of simultaneous equations the determinant of the matrix must be zero in order to obtain non-trivial solutions, giving

$$\begin{vmatrix} -2\mu ikp\sin(ph) & \mu\left(k^2-q^2\right)\sin(qh) \\ \left(-\lambda\left(k^2+p^2\right)-2\mu p^2\right)\cos(ph) & -2\mu ikq\cos(qh) \end{vmatrix} = 0. \tag{2.42}$$

By rearranging this determinant and separating the trigonometric identities, the equation can be written as [38]

$$\frac{\tan(qh)}{\tan(ph)} = \frac{4k^2pq}{\left(k^2-q^2\right)}\frac{\mu}{\left(\lambda k^2+\lambda p^2+2\mu p^2\right)}. \tag{2.43}$$

This can be further simplified using the relationship between the Lamé parameters and the bulk wave velocities given in equations 2.14 and 2.15 to give a characteristic equation for the symmetric modes,

$$\frac{\tan(qh)}{\tan(ph)} = -\frac{4k^2pq}{\left(k^2-q^2\right)^2}. \tag{2.44}$$

Using the same process the characteristic equation for the antisymmetric modes can also be derived, which is closely related to the equation for the symmetric modes, and is given by

$$\frac{\tan(qh)}{\tan(ph)} = -\frac{\left(k^2-q^2\right)^2}{4k^2pq}. \tag{2.45}$$

The similarity between the equations allows the characteristic equation for both symmetric and antisymmetric Lamb wave modes to be written as [38, 53, 97],

$$\frac{\tan(qh)}{\tan(ph)} = -\left[\frac{4k^2pq}{\left(k^2-q^2\right)^2}\right]^{\pm 1}, \tag{2.46}$$

where the sign of the index indicates which type of mode is being described; the positive index refers to the symmetric wavemodes, whilst the negative index refers to the antisymmetric wavemodes. This equation was originally derived by Lamb, and is commonly known as the Rayleigh-Lamb Frequency equation [38, 107–109].

2.2.2 Propagation of Lamb waves

Equation 2.46 provides a mathematical description of Lamb waves, although this equation cannot be solved analytically to determine the valid modes of propagation for the wavemodes; instead it must be solved numerically [38, 53]. This is typically done by rearranging equation 2.46 to give the following

$$\frac{\tan(qh)}{\tan(ph)} + \left[\frac{4k^2pq}{\left(k^2-q^2\right)^2}\right]^{\pm 1} = L_S, \tag{2.47}$$

where in the case of the solution to the equation $L_S = 0$, a valid Lamb wave mode exists. In order to identify the values of frequency thickness and phase velocity where the solution to equation 2.47 is zero, the equation is evaluated for a range of both frequency thickness and phase velocity values, and adjacent values of either the frequency thickness or the phase velocity are compared in order to identify the locations of any zero crossings. These zero crossings are then examined to determine the exact position at which the equation is equal to zero, either by a simple linear interpolation, or by a more complex method such as a Newton-Raphson refinement, and the final positions of the zeros are recorded. The thickness of the plate is usually set to 1 mm, which allows those values of

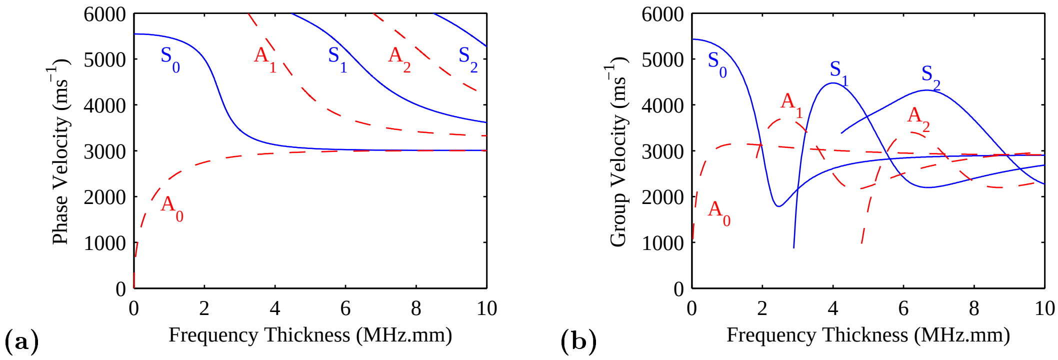

Figure 2.5: Dispersion curves for Lamb waves in aluminium, where the symmetric modes are shown using a solid blue line and the antisymmetric modes are shown with a dashed red line for (a) the phase velocity, (b) the group velocity.

frequency thickness and phase velocity where the equation is soluble to be plotted on a graph of frequency thickness against phase velocity, as shown in figure 2.5 (a) for a 1 mm thick aluminium plate. The resulting dispersion curves show both the existence of multiple Lamb wave modes and how the phase velocities of these Lamb waves vary as a function of frequency thickness.

Although the phase velocities of the Lamb wave modes can be calculated numerically from equation 2.46 the calculation of the group velocity is more complicated. By substituting the relationship $k = {}^{\omega}/_{C_p}$ into equation 2.16 an equation relating the group velocities of the Lamb wave modes to their phase velocities can be found [38],

$$C_g = \frac{C_p^2}{C_p - (fd)\,\frac{dC_p}{d(fd)}}, \tag{2.48}$$

where fd is the frequency thickness of the Lamb wave. The group velocities of the various Lamb wave modes for a 1 mm aluminium plate can therefore be calculated from the phase velocities of those same modes, and the group velocity dispersion curve is shown in figure 2.5 (b) [38].

An important consideration for both the detection and generation of Lamb waves is the determination of the particle motion of the waves within the sample. Although the simultaneous equations governing the symmetric wavemodes presented in equation 2.41 do not allow direct calculation of the coefficients A_2 and B_1, their ratio can be calculated as [53],

$$\frac{A_2}{B_1} = \frac{\left(k^2 - q^2\right)}{2ikp}\,\frac{\sin(qh)}{\sin(ph)}. \tag{2.49}$$

By considering this ratio, and by setting the value of the coefficient B_1 equal to an arbitrary value

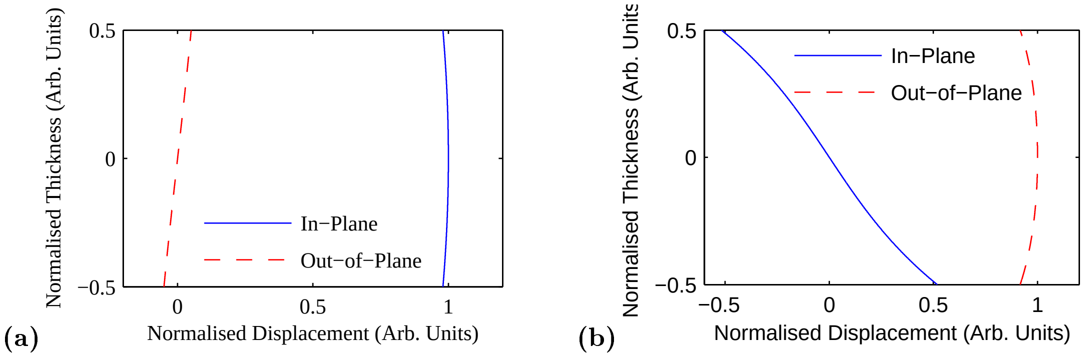

Figure 2.6: Relative displacement profiles showing the proportion of in-plane and out-of-plane displacement at a frequency thickness of 0.5 MHz.mm for (a) the S$_0$wave and (b) the A$_0$wave.

of 1, the relative particle displacements u_1 and u_3 can be calculated from equations 2.33 and 2.34,

$$u_1 = \frac{\left(k^2 - q^2\right)}{2p} \frac{\sin(qh)}{\sin(ph)} \cos(px_3) + q\cos(qx_3), \tag{2.50}$$

$$u_3 = \frac{\left(k^2 - q^2\right)}{2k} \frac{\sin(qh)}{\sin(ph)} \sin(px_3) + k\sin(qx_3), \tag{2.51}$$

where the magnitudes of the displacements are considered. From the values of phase velocity and frequency thickness where Lamb wave modes are supported these equations allow the relative displacements of any of the wavemodes to be calculated, and similar equations can be formulated for the behaviour of the antisymmetric modes,

$$u_1 = -\frac{\left(k^2 - q^2\right)}{2p} \frac{\cos(qh)}{\cos(ph)} \sin(px_3) - q\sin(qx_3), \tag{2.52}$$

$$u_3 = -\frac{\left(k^2 - q^2\right)}{2k} \frac{\cos(qh)}{\cos(ph)} \cos(px_3) + k\cos(qx_3). \tag{2.53}$$

The relative displacement profiles through the thickness of an aluminium sample for the fundamental symmetric and antisymmetric modes have been calculated for a frequency thickness of 0.5 MHz.mm, and figure 2.6 shows the behaviour of the waves. This shows that the energy of the wavemodes is shared between the in-plane displacements and the out-of-plane displacements across the thickness of the plate. There are considerable differences between the two fundamental wavemodes; the S$_0$wave consists almost entirely of in-plane motion at this frequency thickness, while the A$_0$wave has a much more even distribution of energy between the in-plane and out-of-plane displacements.

2.2.3 The Long-wavelength approximations

One possible technique for the application of Lamb waves to thickness measurements is that presented by Dewhurst, where a relationship between the thickness of the sample and the wave velocities of the fundamental modes in that sample is found [55]. This is based on earlier work done by Lamb, where analytical solutions to the characteristic equations for both the symmetric and antisymmetric waves were explored in the limiting case where the thickness of the material was assumed to be much smaller than the wavelength of the propagating wave [107]. This assumption concerns the region of the dispersion curve where only the fundamental modes are supported, at frequency thickness values of less than 2 MHz.mm in aluminium, seen on the far left of the dispersion curve in figure 2.5 (a). By firstly considering the symmetric mode, equation 2.44 can be simplified by assuming that the products qh and ph are small, which in turn permits the use of the small angle approximation $\tan\theta \approx \theta$,

$$\frac{qh}{ph} \approx -\frac{4k^2pq}{\left(k^2-q^2\right)^2}, \tag{2.54}$$

which further simplifies to,

$$\left(k^2-q^2\right)^2 + 4k^2p^2 = 0. \tag{2.55}$$

It is useful at this point to introduce the concept of the longitudinal and transverse wavenumbers, $k_L = {}^{\omega}/{c_L}$ and $k_T = {}^{\omega}/{c_T}$, which, combined with equation 2.28, allow equation 2.55 to be expressed solely in terms of the wavenumbers,

$$\left(2k^2-k_T^2\right)^2 + 4k^2\left(k_L^2-k^2\right) = 0. \tag{2.56}$$

The definitions of the wave velocities from equations 2.14 and 2.15 can then be used to rewrite this in the form

$$\frac{1}{k^2} = \frac{4\left(\lambda+\mu\right)}{\lambda+2\mu}\frac{\mu}{\rho\omega^2}, \tag{2.57}$$

giving an equation for the wavenumber, k, in terms of the frequency of the wave and the material properties. Using equation 2.17 the phase velocity of the S_0 wave, C_S, for the case where the wavelength is much larger than the sheet thickness, can then be given in terms of only the material properties, with no dependence on frequency

$$C_S^2 = \frac{4\left(\lambda+\mu\right)}{\lambda+2\mu}\frac{\mu}{\rho}. \tag{2.58}$$

This relates to the dispersion curve in figure 2.5 (a) in the region where the frequency thickness is small, and there is no dispersion in the S$_0$wave.

A similar process can be followed for the antisymmetric wave in order to obtain an analytical solution to the characteristic equation in the limiting case where the thickness is much smaller than the wavelength. However, in this case the $\tan(\theta)$ terms of equation 2.45 must be expressed as the third order Taylor expansion, as a lower order expansion has a trivial solution, giving

$$\frac{qh\left(1+\frac{1}{3}q^2h^2\right)}{ph\left(1+\frac{1}{3}p^2h^2\right)} = -\frac{\left(k^2-q^2\right)^2}{4k^2pq}. \tag{2.59}$$

By collecting terms, and again using the concept of the longitudinal and transverse wavenumbers, this can be rearranged to give

$$k_T^4 + k^4h^2\left[\frac{4}{3}k_L^2 - \frac{4}{3}k_T^2 + k_T^2\left(\frac{k_T^2}{k^2} + \frac{k_L^2k_T^2}{3k^4} + \frac{4}{3}\frac{k_L^2}{k^2}\right)\right] = 0. \tag{2.60}$$

When ${}^{k_T^2}/_{k^2}$ and ${}^{k_L^2}/_{k^2}$ are $\ll 1$, as is the case where the phase velocity of the A$_0$ wave is much less than either the transverse or longitudinal velocity, as can be seen in the dispersion curve in figure 2.5 (a), this equation simplifies to

$$k_T^4 + \frac{4}{3}h^2k^4k_L^2 - \frac{4}{3}h^2k^4k_T^2 = 0. \tag{2.61}$$

As with the symmetric wave this equation can be written to give the phase velocity of the A$_0$ wave, C_A, in terms of the Lamé parameters and density of the material,

$$C_A^2 = \frac{4}{3}\left(1 - \frac{\mu}{\lambda+2\mu}\right)\frac{\mu}{\rho}h^2k^2.$$

This equation can then be rearranged in order to express it in a similar form to the symmetric wave in equation 2.58,

$$C_A^2 = \frac{k^2h^2}{3}\frac{4\left(\lambda+\mu\right)}{\lambda+2\mu}\frac{\mu}{\rho} \tag{2.62}$$

From inspection of the individual long wavelength approximations (equations 2.58 and 2.62), the equations can be combined to remove any dependence on the material properties, giving a relation between the phase velocities of

$$C_A^2 = \frac{k^2h^2}{3}C_S^2. \tag{2.63}$$

This equation describes an analytical relationship between the phase velocities of the S$_0$ and A$_0$

waves, the wavenumber of the A_0wave, and the half-thickness of the sheet and will be valid for any material. By expressing the wavenumber in terms of frequency and phase velocity, defined in equation 2.17, giving $k^2 = {}^{\omega^2}/_{C_A^2}$, this equation can be written as,

$$C_A^4 = \frac{4\pi^2 f^2 h^2}{3} C_S^2. \tag{2.64}$$

By taking the square root and writing the half-thickness h in terms of the thickness d, the equation can be simplified further [55], to give

$$C_A^2 = \frac{\pi f d}{\sqrt{3}} C_S. \tag{2.65}$$

This equation is referred to as the combined approximation as it is a combination of the analytical solutions to the characteristic equations for both the symmetric and antisymmetric waves, in the limiting case where the wavelength of the Lamb wave is much greater than the thickness of the sample.

By using the relationship between the phase and group velocities of the Lamb waves described by equation 2.48 it is possible to calculate the group velocities, denoted by the subscript g, of the long wavelength Lamb waves, with a resulting equation of

$$C_{Ag} = \frac{\frac{\pi f d}{\sqrt{3}} C_S}{\sqrt{\frac{\pi f d}{\sqrt{3}} C_S} - (fd) \frac{d}{d(fd)} \left(\sqrt{\frac{\pi f d}{\sqrt{3}} C_S} \right)}. \tag{2.66}$$

As the long wavelength approximation for the S_0 wave given by equation 2.58 has no dependence on frequency, the phase and group velocities of the S_0 wave are equivalent. This allows an expression relating the thickness of the sheet to the group velocities of the S_0 and A_0 waves at a specific frequency to be calculated [55], given by

$$C_{Ag}^2 = \frac{4\pi f d}{\sqrt{3}} C_{Sg}. \tag{2.67}$$

Equations 2.65 and 2.67 allow the thickness of a plate to be calculated directly from the measured velocities of the fundamental Lamb waves, provided that the frequency of the waves and thickness of the sheet are such that the long wavelength condition is valid, without *a priori* knowledge of the material properties.

As previously mentioned work on the application of these approximations to thickness measurements has been previously undertaken [55], although in this study only the group velocity approximation was used. A laser based system for the generation and detection of ultrasound was used, and although this work provides a good introduction to this novel measurement technique there are some issues with the methodology used.

In reference [55] the group velocity approximation was used in preference to the phase velocity approximation. While the group velocities are simpler to measure than phase velocities, it is shown in section 4.1 that the accuracy of the phase velocity approximation is significantly greater than that of the group velocity, a detail not considered in the original paper. Furthermore, the method of measuring the group velocity is limited in its accuracy. The relationship between the arrival time and the frequency is determined by hand for each individual A-scan; rather than using a method of time frequency representation, such as a short time Fourier transform [110]. The frequency of the wave at a given point in the A_0wave train is identified by taking the inverse of the time between successive peaks, while the arrival time of that frequency is taken as the mean arrival time. This method extracts very little of the available information from the experimental data, with large sections of the wave reduced to only a few measurement points with no estimate of uncertainty or error.

From the group velocity measurements the thickness of the sample can be calculated. In reference [55] this is done by plotting the square of the group velocity against the frequency for ten frequencies, and a line is then fitted, passing through the data and the origin. The gradient of the line is then scaled using the S_0 group velocity to obtain the thickness of the sample. Although the exact relationship between the frequency thickness of the Lamb waves and the accuracy of the approximation has not been quantified it is recognised that the low frequency data is more reliable, and thus only the first four data points were used to fit the line relating the frequency to the square of the group velocity. However, it is can be seen for the two figures shown in [55] for this plot that the fourth plot deviates markedly from the proposed straight line fit, and thus will introduce an error into the gradient.

A further concern about the experiments presented in reference [55] is their repeatability. Although thickness measurements have been performed on a number of samples, with thicknesses ranging from 27 μm to 425 μm, where the accuracy of the measurement decreases from 98.1 % to 70.5 % over the thickness range, only a single measurement has been performed on each of these samples, with no estimate provided on the uncertainty of the measurement. This means that there is no information presented on the reliability of the measurement, as the measurements presented could simply be the best results obtained from hundreds performed, or could be uncharacteristically poor results obtained by chance.

In this work a detailed comparison of both versions of the approximation will be performed, and a large number of thickness measurements will be taken in order to fully investigate the reliability of this method. In addition, the increase in computational power since the publication of reference [55] will allow the process of the signal analysis to be performed using a well defined algorithm, further increasing the repeatability and transparency of the work presented in this thesis.

2.3 Generation and detection of ultrasound using EMATs

Electromagnetic acoustic transducers (EMATs) have been used for a number of decades for generating and detecting ultrasound in electrically conductive or ferromagnetic samples [75, 111–114]. These non-contact transducers have a number of advantages in that they can generate ultrasound in the sample without loading the sample [68], and can be scanned across the surface of the sample at high speed [115]. This section introduces the theory behind the operation of EMATs, and discusses some typical transducer designs. In this section the symbols ρ and σ refer to the electrical material properties of resistivity and conductivity respectively.

2.3.1 General Principles of EMATs

An EMAT is a device capable of translating an electrical signal into forces at the surface of a sample in order to generate ultrasound, and in this respect is similar to a piezoelectric transducer. The key difference between these two devices is in the manner by which they couple energy into the sample; a piezoelectric transducer uses physical coupling to transfer sound waves generated by an oscillating crystal into the sample, whereas an EMAT uses electromagnetic coupling. Both piezoelectric transducers and EMATs are reversible, in that the same transducer used to generate ultrasound in a sample can also be used to detect ultrasound in the same sample. An EMAT uses the interaction of a dynamic magnetic field, produced by the flow of a time varying current through an electrical coil, with a conducting sample in order to generate forces within the sample [111, 112], as seen in figure 2.7. This dynamic field will interact with the sample through a number of mechanisms to generate ultrasound in the sample, with the exact mechanisms present depending on the characteristics of the sample. In electrically conductive samples the dynamic field will induce an image current in the surface of the sample in opposition to the current flowing in the coil, and this induced eddy current in the presence of a magnetic field will generate a force due to the Lorentz mechanism. Further generation mechanisms are present in ferromagnetic samples, where the dynamic field interacts magnetically with the sample, and these are known as the magnetostrictive and magnetisation mechanisms. The design of EMAT transducers can be varied in order to optimise the direction of the forces generated in the sample. A typical EMAT design consists of a coil through which a time varying current is driven, and this current generates a

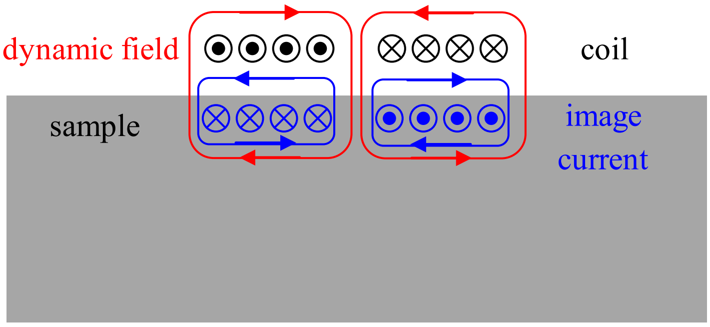

Figure 2.7: Basic principals of EMAT generation of ultrasound, where a time varying current generates a dynamic magnetic field.

varying magnetic field [112]. A permanent magnet can be used to provide a bias field to enhance the generation of Lorentz forces, as discussed in section 2.3.1.1, although an electromagnet can also be used [116].

2.3.1.1 EMAT operation using the Lorentz force

EMATs couple energy into a sample electromagnetically via a number of mechanisms, which vary in importance depending on the type of sample being considered. Typically EMATs are used on electrically conductive samples, and thus the most commonly considered is the Lorentz force, which is present in all EMAT generation in electrically conducting materials. The Lorentz mechanism is that by which a current flowing in a magnetic field will exert a force on the medium in which the current is flowing [117], and size and direction of a Lorentz force is given by

$$\vec{F} = q\left(\vec{E} + \vec{v} \times \vec{B}\right), \tag{2.68}$$

where $\vec{E}$ is the vector electric field, $\vec{v}$ is the velocity of the charged particle, in this case an electron with charge q, and $\vec{B}$ is the magnetic flux density. For the operation of a generation EMAT there is no electric field so that term is omitted, and the charged particles in motion are the electrons flowing in the image current at the surface of the sample, seen in figure 2.8. For a normal static bias field, as is typical in radially polarised shear wave EMATs [72], the force generated can be written in terms of the eddy current density [114], J_{eddy}

$$\vec{F} = J_{eddy} B_0 \,\hat{r} + J_{eddy} B_D \,\hat{z}, \tag{2.69}$$

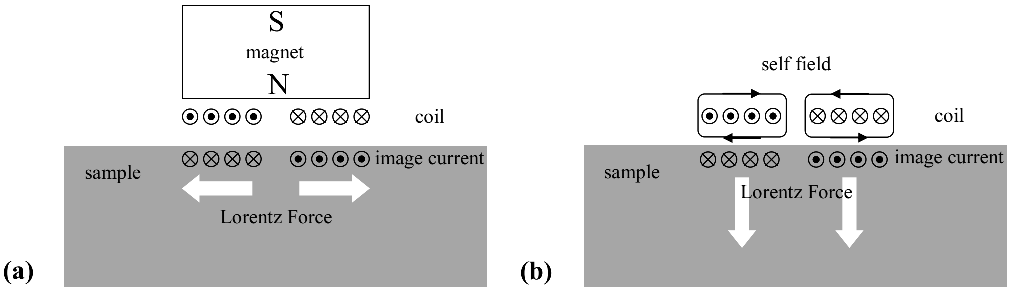

Figure 2.8: Comparison between the Lorentz force generated by an EMAT due to (a) the bias field produced by a permanent magnet, and (b) the self field produced by a time varying electrical current in the coil.

where an angular symmetry is assumed about the centre of the coil, and the force is given in cylindrical coordinates. The term B_0 relates to the static bias field, and the term B_D is the dynamic self field of the coil, where the orientation of the forces is shown in figure 2.8. The static bias field and the force it produces in the radial direction is shown in (a), while the dynamic field, and the normal force that it produces, is shown in (b). It is important to note that both forces will be present in a sample where a radially polarised shear wave EMAT is used to generate ultrasound, and although the magnitude of the forces is unlikely to be equal, with the force due to the static field being much larger than that of the dynamic field [72], the dynamic field can still create significant effects on the generated ultrasound [118]. Another important note about the interaction of the self field with the eddy currents in the sample is that it will always produce a repulsive force in the sample, and thus the force generated is at twice the frequency of the input signal [119].

In addition to the Lorentz force mechanism of generation present in electrically conductive samples, there are additional mechanisms which have a significant effect in generating ultrasound in ferromagnetic samples using EMATs. Both magnetostriction and magnetisation forces are capable of coupling electromagnetic energy into a ferromagnetic material to generate ultrasound [120–122], although the generation mechanisms are distinct. The magnetisation creates an attractive force between the ferromagnetic material and the source of the magnetisation [121], while the magnetostrictive forces will create a change in the shape of the sample due to a dynamic magnetic field [122], in analogy to the behaviour of a piezoelectric material in a dynamic electric field.

These effects are not present in paramagnetic materials, such as aluminium or stainless steel, which have been primarily used in the research presented in this thesis, although they will be present in the mild steel samples used. However, when the various generation mechanisms in mild steel are quantified the force generated via magnetostriction as a percentage of that generated by the Lorentz force is between 25.7 to 27.5 % [78, 120], and thus the effects of the additional generation mechanisms have not been considered.

2.3.1.2 Skin effect

Due to the electromagnetic nature of the coupling, the volume of the sample which is affected by the dynamic magnetic field from the coil is limited by the electromagnetic skin effect [123]. For a good conductor, the current density at a given depth, z, can be defined as [124],

$$J = J_0 e^{-z/\delta}, \tag{2.70}$$

where J_0 is the current density at the surface and δ is the skin depth of the material. This skin depth is a function of angular frequency, ω, and the electrical properties of the material, and is described by

$$\delta = \sqrt{\frac{2\rho}{\omega \mu_r \mu_0}}, \tag{2.71}$$

where ρ is the resistivity, μ_r is the relative magnetic permeability of the sample and μ_0 is the permeability of free space.

In addition to the decrease in the current density with depth, the skin effect also applies a phase delay to the eddy current which is a function of the depth. Where a semi-infinite medium is considered, the total delay can be calculated by integrating the delay at each depth over the infinite half-space giving a total delay of $\frac{\pi}{4}$ [124]. However, for materials where the thickness of the medium is comparable to the skin depth the phase delay must be considered mathematically using a complex value of the skin depth, where the real part of the skin depth governs the intensity of the current at a given depth, while the imaginary part governs the delay. This introduces an additional term to equation 2.70 [124];

$$J = J_0 e^{-z/\delta} e^{-iz/\delta}. \tag{2.72}$$

This equation can be used to calculate both the decay in intensity and phase lag with depth caused by the skin effect. An example of this equation is shown for a 100 kHz alternating current (AC) in aluminium in figure 2.9, where (a) represents the amplitude of the current, normalised to the amplitude at the surface, while (b) shows the phase delay. The signal oscillates with time and the amplitude drops off exponentially with depth. For a 100 kHz signal there is still significant energy (50 % of the surface energy) at depths of 185 µm in an aluminium sample. However, in the region where significant energy is present in the sample at depths of less than 185 µm, there is less than 0.7 µs, allowing the phase delay term to be largely ignored.

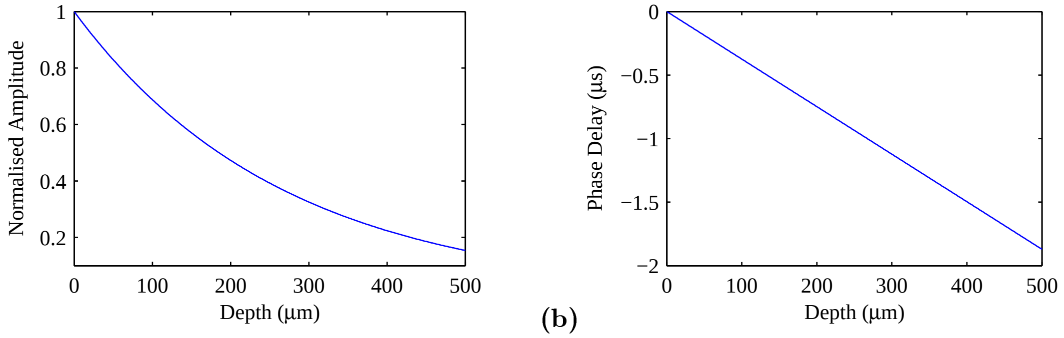

Figure 2.9: The skin effect in aluminium visualised for a 100 kHz AC current with the colour scale showing the amplitude of the wave normalised to the amplitude at the surface.

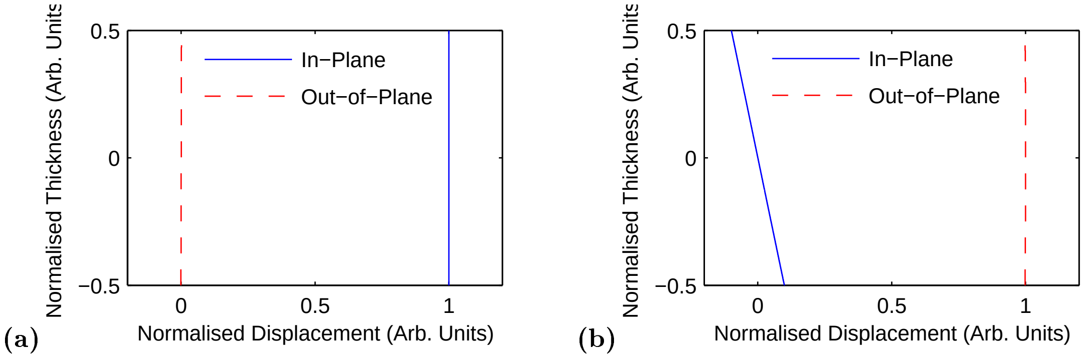

Figure 2.10: Relative displacement profiles showing the proportion of in-plane and out-of-plane displacement at a frequency thickness of 0.01 MHz.mm for (a) the S_0wave and (b) the A_0wave.

2.3.2 Using Lorentz force to customise sensitivity

The combined approximations in section 2.2.3 that are to be used to measure thickness require that the wavelength of the Lamb wave be much greater than the thickness of the sheet in which they propagate. For an A_0 wave at 100 kHz in an aluminium sample 100 µm thick the wavelength is 3.1 mm, which is considerably greater than the thickness of the sheet. From the values of the phase velocities of the A_0 and S_0 Lamb waves at this frequency thickness value the relative displacement profiles across the thickness of the sheet can be calculated using equations 2.50-2.53, and these are shown in figure 2.10. For the S_0wave in (a) the displacement is almost entirely in-plane, with almost no out-of-plane component, and is uniform through the thickness of the sample, while for the A_0 wave shown in (b) the large majority of the displacement is out-of-plane, which is again uniform throughout the sample, although there is some in-plane displacement which has its greatest amplitude at the surface of the sample. From this it is apparent that in this regime of frequency thickness it should be possible to perform selective generation of the A_0 or S_0 waves depending on the direction of the force provided by the EMAT. This will be performed by using the Lorentz force interaction from the self field of the EMAT coil to generate an out-of-plane force to generate

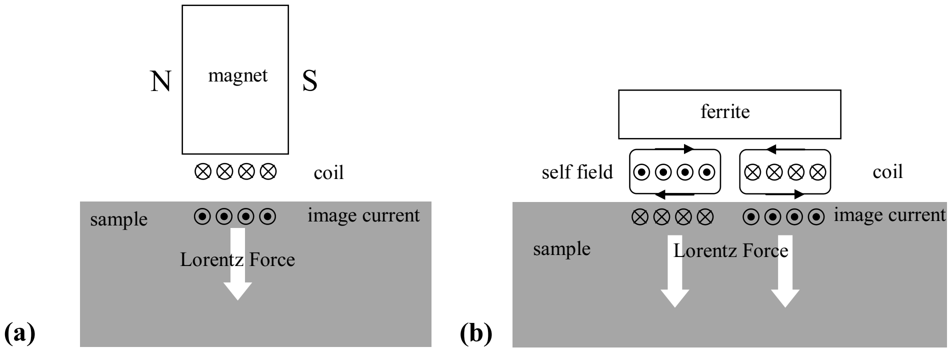

Figure 2.11: Schematic diagram of EMATs designed to generate predominantly out-of-plane displacements. (a) A linear coil with a bias field parallel to the sample surface, and (b) a spiral coil with a ferrite backing in order to enhance the self-field.

predominantly A_0 waves, and will be discussed in greater depth in sections 2.3.3 and 3.2.1. The detection EMAT will be similarly selective, with an in-plane EMAT being predominantly sensitive to the S_0 wave, while an out-of-plane EMAT will be sensitive to the A_0 wave.

2.3.3 Standard EMATs used in this work for generation or detection of out-of-plane forces

The generation EMATs used in this project have been designed specifically for their ability to generate out-of-plane displacements using the Lorentz mechanism, as this out-of-plane displacement will preferentially generate the A_0 wave (figure 2.10). This focus on the measurement of the A_0 wave is due to the square term in equation 2.65, meaning that the A_0 wave is likely to be the dominant source of uncertainty in thickness measurements made using the combined approximation. Similarly the detection EMATs have been selected due to their sensitivity to out-of-plane displacements. A number of different designs have been used during the course of the research, and the more complex designs are discussed in more detail in section 3.2. The simpler out-of-plane transducers are discussed here, such as the linear coil transducer shown in figure 2.11(a), as these are standard EMAT designs, although they were manufactured as part of this research. The linear coil transducer will generate eddy currents in the surface of the sample, which will interact with both the static bias field and the dynamic field to provide an orthogonal force, as shown in the figure. The linear coil design can also be used for the detection transducer, although there are substantial differences between the coils between the two transducers. For the generation transducer the number of turns of wire in the coil is effectively limited by the spatial domain, where the width of the coil limits the frequencies it can generate [111], as the low frequency of operation reduces the effects of inductance and interwinding capacitance on the EMAT coil [125].

Additionally, the gauge of wire used must be sufficiently large to reduce or eliminate the effects of ohmic heating arising from the generation pulse [126]. For the detection EMAT this constraint is not present, and so the thickness of the wire can be decreased, while the number of turns is increased.

The generation of out-of-plane forces from the interaction of the dynamic field of an EMAT with the surface eddy currents has been discussed in section 2.3.1.1, where the dynamic field of the EMAT both generates the eddy current in the surface of the sample and causes a Lorentz force to be generated in the surface of the sample as well. This self-field generation can be enhanced by placing a ferrite behind the coil in order to focus the magnetic field [127], and a schematic diagram of this EMAT is shown in figure 2.11 (b). Unlike the EMAT shown in figure 2.11 (a), the ferrite backed EMAT cannot be used as a detection transducer due to the lack of bias field, although this design has been previously shown to generate Lamb waves with fewer distortions than a spiral coil with a bias field [118].

When discussing the thickness measurements in section 2.1.2, the dead time, the time when the generation pulse of a transducer saturates the detection transducer, can be a complicating factor. In EMAT measurements, even when using separate generation and detection transducers the dead time can be a large factor, due to the long range effects of the electromagnetic coupling [49, 62].

2.4 Signal Processing

The calculation of the group velocities of the A_0 and S_0 waves required in order to calculate the thickness of a sample when using the approximation in equation 2.67 is relatively straightforward when using narrow-band waves, as the arrival time of the envelope of the wave will give the group velocity. However, for a broadband wave the analysis is more complex, as the dispersive nature of the Lamb waves will spread the arrival times for different frequencies in the wave. This problem is typically resolved using some form of time-frequency representation, such as a short-time Fourier transform, a wavelet transform, or a Wigner-Ville distribution [128–131]. In this research the measurement of the phase velocity of the Lamb waves was the primary focus, and the relationships of the Fourier transform and the cross spectral density to phase velocity will be examined here. These phase velocity measurements have a different set of complexities to the group velocity measurements, due to the problems of the unknown initial phase of the wave, as well as the issue of phase unwrapping, which will both be discussed. The problems of dispersion are also mainly limited to the A_0 wave for the low frequency thicknesses used in this research, as the S_0 is effectively non-dispersive in this region.

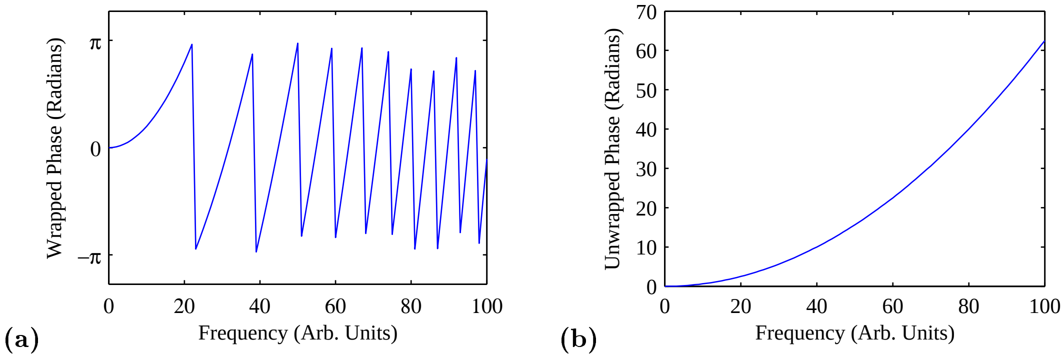

Figure 2.12: Example phase spectra to demonstrate the effects of unwrapping. (a) A wrapped phase spectra, as would be obtained from the argument of a Fourier transform, and (b) the same spectrum once it has been unwrapped via a difference detection method.

2.4.1 Fourier transforms

The continuous Fourier transform is part of the Cohen class of transforms which examines the similarity of an infinite signal to an infinite number of sines and cosines [131,132]. When considering digital signals it is important to note that the signal cannot extend over infinite time, and in these cases the discrete Fourier transform (DFT) is used,

$$X\left(g\right)=\sum_{n=1}^{N}x\left(n\right)e^{-i2\pi gn/N}, \tag{2.73}$$

where the term n is the index of the signal x, which has a maximum length N. The variable g is the index of the inverted signal X, which is the frequency spectrum when x defines a time domain signal, as in this work. Computationally the DFT is usually calculated by the fast Fourier transform algorithm (FFT).

The Fourier transform of a real-valued signal results in a complex signal of the same length, although the result is conjugate symmetric, as no new information is obtained [131]. The magnitude of the complex signal represents the amplitude of the transform and gives the frequency content of the time domain signal. The argument of the complex numbers represents the phase of the time domain signal, and is calculated by taking the arctangent of the ratio of the imaginary components to the real components,

$$\arg\left(z\right)=\arctan\left(\frac{y}{x}\right), \tag{2.74}$$

for a complex number defined by $z = x + iy$. As a result of the arctan function the phase obtained is bounded by values of $\pm\pi$. This bounded phase spectrum is known as the wrapped phase spectrum, and can be seen in figure 2.12 (a). In order to be used in most types of analysis this phase spectrum must be unwrapped, a procedure that reverses the modulo operation imposed by the arctan function.

The simplest form of phase unwrapping is the difference detection (DD) method, where the difference between adjacent points on the phase spectrum is calculated. If the difference is greater than π radians then the phase spectrum is assumed to have undergone a wrapping operation, and a value of $\pm 2\pi$ is applied to the latter point in order to undo this operation. A successful example of this unwrapping method is shown in figure 2.12 (b), where the synthetic wrapped signal shown in (a) has been unwrapped. The limitation of this method is that if the rate of change of phase between adjacent positions in the spectrum is larger than π the algorithm will incorrectly interpret the difference as a wrapping point, and will unwrap the spectrum in error at this point. A more detailed analysis of the limitations of this method of phase unwrapping, and presentation and analysis of alternative methods, is given by Karam [133].

An implementation of the DD method of phase unwrapping, where the length of the DFT is increased, and the phase unwrapped until two subsequent phase spectra match, is intended to overcome the limitation of a rapidly varying phase. However, as noted by Karam it is possible that two phase spectra at increasing sample sizes may have the same incorrect unwrapped spectra [133]. An alternative method of unwrapping the phase is that of adaptive numerical integration, first suggested by Tribolet [134], where the differential of the phase is calculated from the wrapped spectrum, and then integrated to obtain the unwrapped spectrum. Due to the adaptive nature of this algorithm it is shown that the computational cost increases with the rate of phase change, which limits the effectiveness of the algorithm on signals with a high rate of phase change. A further method, presented by Steiglitz, is that of polynomial factoring, where a Z-transform is applied to the time series to be unwrapped in order to calculate the roots of the signal in the Z-plane [135]. The Z-plane is the generalised form of a Fourier transform, where rather than the imaginary frequency used in a DFT, a complex frequency is used. This type of transform is often used to evaluate the performance of filters, but can also be applied to other problems [131]. By summing the phase contribution of each individual root of the time domain signal the total unwrapped phase of the signal can be computed. An efficient algorithm that applies a scaling factor to multiple instances of the FFT in order to evaluate the Z-transform has also been developed [136].

In order to calculate the thickness from the combined approximation given in equation 2.65 the phase velocity must be measured, rather than simply the group velocity, and this can be calculated from the unwrapped phase spectrum using [137],

$$C_p\left(f\right) = \frac{2\pi f L}{\phi\left(f\right) - \phi_0 + 2\pi N}, \tag{2.75}$$

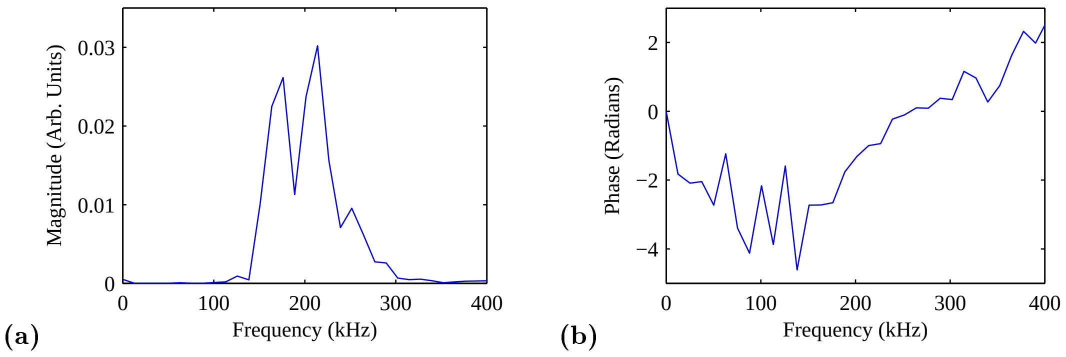

Figure 2.13: An example showing (a) the magnitude and (b) the phase spectrum of a signal. The region where there is significant frequency content can be seen in (a), which corresponds to the region where the phase spectrum contains meaningful information in (b).

where f is the frequency, L is the distance over which the wave has propagated, $\phi(f)$ is the phase spectrum, ϕ_0 is the initial phase, and N is an integer value. The $2\pi N$ term is a correction that addresses two distinct problems relating to the wrapped nature of the phase spectrum. Firstly, the term encompasses the number of complete wavelengths between the generation position and detection position. In a similar manner to the problem of unwrapping the number of whole wavelengths between the generation position and the detection position is not described by the phase spectrum, as only the wrapped value of the phase is given by the phase spectrum. By adding an integer value of 2π the number of complete wavelengths travelled by the wave is given by the integer N. Secondly, the term addresses the issue that the beginning of the phase spectrum of a signal may be unknown, an example of which is shown in figure 2.13. In this figure the frequency content of the signal can be seen in (a), and it is clear that there is no meaningful signal below approximately 125 kHz. The corresponding phase of the signal can be seen in (b), and although the phase spectrum has values for the region below 125 kHz, these values are unreliable as the signal has no frequency content in this region. The number of unwrapping steps in the phase spectrum between the initial frequency and the first frequency with meaningful frequency content, i.e. in the region below 125 kHz, is unknown as there is no significant magnitude in this region, and thus the first phase must be corrected by applying the term $2\pi N$, for a suitable value of N in order to compensate for the region where no information is present.

2.4.2 Cross spectral density

It is often the case that the initial phase of the signal, ϕ_0, is not known, and thus equation 2.75 cannot be used. It can instead be rewritten by considering the phase difference spectrum between two closely spaced measurement positions [138],

$$C_p\left(f\right) = \frac{2\pi f x}{\left[\phi_1\left(f\right) - \phi_2\left(f\right)\right] + 2\pi n}, \tag{2.76}$$

where x is the distance between the measurement positions, and n is an integer value. As with equation 2.75 the integer n has two contributing factors: the sum of the number of complete wavelengths between the positions at which the phase spectra are measured; and the unknown phase before the start of the frequency content in the phase spectra (as shown in figure 2.13). The term $\left[\phi_1\left(f\right) - \phi_2\left(f\right)\right]$ is often referred to as the phase difference spectrum (PDS) or $\Delta\phi\left(f\right)$, and can be calculated by subtracting the phase spectra calculated by the DFT for two time domain signals.

A direct method for calculating the PDS exists, and this uses an analysis tool called the cross spectral density (CSD). The CSD, $S_{fg}\left(\omega\right)$, is the Fourier transform of the cross-correlation of two functions and is described analytically as [139],

$$S_{fg}\left(\omega\right) = \int_{-\infty}^{\infty} R_{fg}\left(t\right) e^{-i\omega t} dx, \tag{2.77}$$

where $R_{fg}\left(t\right)$ is the cross-correlation of the functions $f\left(t\right)$ and $g\left(t\right)$. The magnitude of the CSD describes the cross correlation of the frequency content of the two time domain signals, while the argument gives their phase difference spectrum. This allows for the easy identification of frequency regions where both time domain signals have significant content, as in figure 2.13, and a direct calculation of the phase difference spectrum.

The convolution theorem, together with the linearity of the Fourier transform, allows the CSD to be expressed as the convolution of the Fourier transforms of the two signals [131],

$$S_{fg}\left(\omega\right) = \left(\int_{-\infty}^{\infty} f\left(t\right) e^{-i\omega t} dx\right)^{*} \cdot \left(\int_{-\infty}^{\infty} g\left(t\right) e^{-i\omega t} dx\right) \tag{2.78}$$

where the asterisk denotes the complex conjugate. This allows the CSD of the two signals to be calculated efficiently using the fast Fourier transform (FFT), an implementation of the DFT.

The phase unwrapping of the phase difference spectrum is, in practice, slightly easier than the unwrapping of an individual phase spectrum, as the PDS for two closely spaced measurement positions is likely to vary much less rapidly than either of the individual phase spectra [138]. The fact that the rate of change of phase is low avoids the limitation of the DD method that the phase shift between adjacent points of the spectrum cannot be larger than π radians, and allows this method to be used in preference to the more flexible, but complicated methods, such as adaptive numerical integration or polynomial factoring [133,134,136].

2.5 Eddy Currents

In addition to the thickness measurements using Lamb waves, a commercial research project was conducted based on the accurate quantification of lift-off using eddy currents. Due to the commercial nature of this research further details of the measurements will be discussed in chapters 7 to 10, which will be redacted from the publicly available version of this thesis. The theoretical background for the eddy current measurements used is discussed here.

Electromagnetic eddy currents occur as a result of the interaction of a varying magnetic field with a conducting material, and act in opposition to the varying field which creates them. They are often used in non-destructive testing for flaw detection and lift-off measurements [16,18,96,140–142]. In this section a model using equivalent circuits is presented which is capable of predicting the behaviour of a coil through which an AC current is flowing in proximity to a conductive sample In keeping with the electrical engineering definition of the imaginary number, j will be used here instead of i.

2.5.1 Introduction to Eddy currents and inductive coupling

An eddy current probe typically consists of a coil of fine wire (typically under 0.1 mm in diameter), occasionally with a ferrite core in order to increase the sensitivity of the coil [1,18]. In eddy current testing an electrically conductive sample is placed in proximity to a coil with an AC signal being passed through it. The AC signal creates a dynamic magnetic field, which will generate eddy currents in the surface of the sample. These eddy currents will in turn affect the dynamic magnetic field and the response of this field will vary depending on the sample. The change in the dynamic field can be monitored in a number of ways, including measuring the magnetic field using Hall sensors or giant magnetoresistance devices [14]. However, the simplest method of measuring the response of the sample to the eddy currents is using the eddy current coil itself, where the impedance of the coil is measured in order to infer information about the surface of the sample. As an electrical circuit these coils will have a resonant frequency, and, although there has been some work on operating at or near this resonance [15,142], when used for NDE the coil is driven with an electrical current well below the resonant frequency [1,2,92].

As the lift-off between an eddy current coil and a conductive sample increases there will be a change in both the complex impedance of the coil and its resonant frequency [143]. When the coil is moved from free space closer to a metal sample the eddy current coil will interact with the

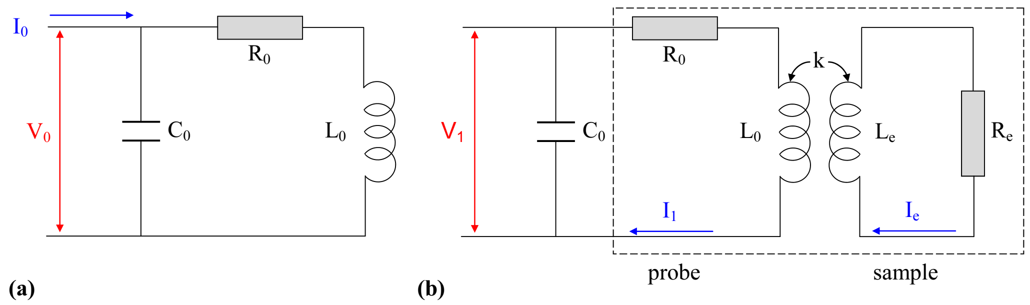

Figure 2.14: A diagram of the equivalent circuit model of an eddy current coil (a) in free space, and (b) in proximity to a metallic sample

sample, through a number of different effects depending on the sample properties. The simplest case for this behaviour is for a paramagnetic sample, where the main interaction is via inductive coupling between the coil and the sample. This occurs as the AC signal in the coil creates a dynamic magnetic field that induces eddy currents in the sample, which in turn create their own dynamic magnetic field. The induced dynamic magnetic field opposes the dynamic field of the coil and will create a change in the impedance of the coil. An additional effect in paramagnetic samples is capacitive coupling between the sample and the coil. This occurs where the electric current in the coil creates a capacitance with the surface of the conductive metal sample However, this is only significant at very low lift-off values, on the order of 10 µm, and is ignored in this case as the operating lift-offs will be much larger.

In order to calculate the resonant frequency of the coil in air it can be useful to consider the coil as an electronic circuit, although solutions can also be obtained using Maxwell's laws [91]. The circuit model can be extended to include the presence of a metallic sample in proximity to the coil by including additional virtual components that represent the sample, and an equivalent circuit can be created in order to calculate the complex impedance and resonant frequency in the presence of the sample.

2.5.2 Equivalent Circuit model, ignoring resistance

An eddy current probe can be thought of as an LCR circuit, where the capacitance (C_0) is in parallel to both the resistance (R_0) and inductance (L_0) which are in series with each other, as shown in figure 2.14 (a) [144]. The capacitance results from the intra-winding capacitance of the coil, as well as the capacitance of any cabling attached to the coil, while the inductance is the result of the coil itself. The resistance is simply the total resistance of both the coil and the cabling attached to it. This model for the eddy current circuit only considers the circuit in air, where there is no change to the inductance L_0 due to interaction with a sample. The complex impedance of this circuit can be calculated by first considering the complex impedance of the resistor and inductor branch independently of that of the capacitor branch. The impedances of these branches are given respectively by

$$Z_L = R_0 + j\omega L_0, \tag{2.79}$$

$$Z_C = \frac{-j}{\omega C_0}, \tag{2.80}$$

where j is $\sqrt{-1}$ and ω is the angular frequency at which the impedance is measured. The total impedance of the circuit, Z_T, can then be calculated by considering the two branch impedances [144],

$$Z_T = \frac{Z_L Z_C}{Z_L + Z_C}, \tag{2.81}$$

where Z_T is the total impedance of the equivalent circuit. By using the definitions of Z_L and Z_C in equations 2.79 and 2.80 the total impedance of this circuit can be calculated as,

$$\begin{aligned} Z_T = Z_0 &= \frac{(R_0 + j\omega L_0)\left(\frac{-j}{\omega C_0}\right)}{(R_0 + j\omega L_0) - \left(\frac{j}{\omega C_0}\right)}, && (2.82) \\ &= \frac{R_0 + j\omega L_0}{1 + j\omega C_0 R_0 - \omega^2 L_0 C_0}. && (2.83) \end{aligned}$$

The resonant frequency of an electrical circuit occurs when the impedance is at its maximum, which in this case can be calculated by determining the point at which the denominator of the impedance is at it's minimum. This can be done by solving the quadratic equation formed by setting the denominator equal to zero, which gives a resonant frequency of [145]

$$\omega_0 = \sqrt{\frac{1}{L_0 C_0} - \left(\frac{R_0}{L_0}\right)^2}. \tag{2.84}$$

When the equivalent circuit model is expanded to consider the effects of the mutual inductance caused by bringing the coil into proximity with a conductive sample, additional components are added to the circuit, as shown in figure 2.14 (b). As the changes to the impedance in the circuit due to lift-off will be due to the inductive coupling between the probe and the sample, initially only the inductive portion of the circuit, denoted by the subscript L, will be considered. The quality of the coupling between the coil and the sample is described using the term k, the coupling coefficient. This term is a simple representation of an extremely complex phenomenon, governing the electrical properties of the sample, the physical properties of the coil and the lift-off of the coil from the sample [15, 143]. By applying Kirchoff's laws to the inductive branch of the circuit the voltage in the probe portion of the circuit can be calculated (equation 2.85), as can the voltage in the eddy current portion of the circuit (equation 2.86), by reference to figure 2.14 (b);

$$V_{1,L} = I_{1,L}\left(R_0 + j\omega L_0\right) - I_e\left(j\omega L_e k\right), \tag{2.85}$$

$$0 = I_e\left(R_e + j\omega L_e\right) - I_{1,L}\left(j\omega L_0 k\right), \tag{2.86}$$

where k is the coupling coefficient between the eddy current coil and the sample [143], $V_{1,L}$ is the voltage in the eddy current probe and the voltage within the sample itself is equal to zero. By rearranging equation 2.86 to solve for I_e the following equation is obtained,

$$I_e = \frac{I_{1,L}\left(j\omega L_0 k\right)}{R_e + j\omega L_e}. \tag{2.87}$$

This can be substituted into equation 2.85 to obtain an equation relating the voltage and current, $V_{1,L}$ and $I_{1,L}$, which can be used to calculate the complex impedance of the inductive branch of the circuit shown in figure 2.14,

$$Z_{1,L} = \frac{V_{1,L}}{I_{1,L}} = \left(R_0 + j\omega L_0\right) - \frac{\left(j\omega L_e k\right)\left(j\omega L_0 k\right)}{R_e + j\omega L_e}, \tag{2.88}$$

which can be rearranged to give

$$Z_{1,L} = R_0 + j\omega L_0\left(1 - k^2\right) + \frac{j\omega L_0 R_e^2 k^2 + \omega^2 L_0 L_e R_e k^2}{R_e^2 + \omega^2 L_e^2}. \tag{2.89}$$

When considering a sufficiently thick sample compared to the electromagnetic skin depth, and for a treatment of the electromagnetic field generated by the eddy current coil as a plane wave, the resistive and reactive components of the image eddy current are equal [124],

$$R_e = \omega L_e. \tag{2.90}$$

Using this substitution, and separating the impedance into real and imaginary parts, equation 2.89 can be re-written as

$$Z_{1,L} = \left[R_0 + \omega L_0 \frac{k^2}{2}\right] + j\left[\omega L_0\left(1 - \frac{k^2}{2}\right)\right]. \tag{2.91}$$

By considering the total impedance of the circuit in figure 2.14 (b), and not just that of the inductive loop, equation 2.81 allows the capacitance C_0 to be included,

$$\begin{aligned} Z_1 &= \frac{\left(\frac{-j}{\omega C_0}\right)\left(R_0 + \omega L_0 \frac{k^2}{2} + j\omega L_0 \left(1 - \frac{k^2}{2}\right)\right)}{\left(\frac{-j}{\omega C_0}\right) + \left(R_0 + \omega L_0 \frac{k^2}{2} + j\omega L_0 \left(1 - \frac{k^2}{2}\right)\right)} && (2.92) \\ &= \frac{R_0 + \omega L_0 \frac{k^2}{2} + j\omega L_0 \left(1 - \frac{k^2}{2}\right)}{1 + j\omega C_0 R_0 - \omega^2 C_0 L_0 \left(1 - \frac{k^2}{2}(j+1)\right)}. && (2.93) \end{aligned}$$

By considering the simplest case, where the resistance of the coil is low enough to be considered negligible, i.e. $R_0 \ll \omega L_0$, the equation for the impedance can be written as

$$Z_1 = \frac{\omega L_0 \frac{k^2}{2} + j\omega L_0 \left(1 - \frac{k^2}{2}\right)}{1 - \omega^2 C_0 L_0 \left(1 - \frac{k^2}{2}(j+1)\right)}, \tag{2.94}$$

and the resonance frequency can be calculated analytically by considering the maximum of the above equation. One possible method of obtaining the maximum is by taking the differential of equation 2.94 with respect to ω using the quotient rule,

$$\frac{df(\omega)}{dx} = \frac{d}{d(\omega)}\left[\frac{g(\omega)}{h(\omega)}\right] = \frac{g'(\omega)h(\omega) - g(\omega)h'(\omega)}{[h(\omega)]^2}, \tag{2.95}$$

where $f(\omega)$ is the function being differentiated, in this case Z_1, and the following substitutions are used,

$$\begin{aligned} g(\omega) &= \omega L_0 \frac{k^2}{2} + j\omega L_0 \left(1 - \frac{k^2}{2}\right) = j\omega L_0 k' && (2.96) \\ h(\omega) &= 1 - \omega^2 C_0 L_0 \left(1 - \frac{k^2}{2}(j+1)\right) = 1 - \omega^2 C_0 L_0 k' && (2.97) \\ g'(\omega) &= L_0 \left(j + \frac{k^2}{2}(1-j)\right) = jL_0 k' && (2.98) \\ h'(\omega) &= -2\omega C_0 L_0 \left(1 - \frac{k^2}{2}(j+1)\right) = -2\omega C_0 L_0 k'. && (2.99) \end{aligned}$$

The following substitution is used to simplify the equations,

$$k' = \left(1 - \frac{k^2}{2}(j+1)\right) = -j\left(j + \frac{k^2}{2}(1-j)\right). \tag{2.100}$$

The differential of the impedance can be written as,

$$\frac{dZ_1}{d\omega} = \frac{jL_0 k' \left(1 - \omega^2 C_0 L_0 k'\right) - j\omega L_0 k' \left(-2\omega C_0 L_0 k'\right)}{\left[1 - \omega^2 C_0 L_0 k'\right]^2}. \tag{2.101}$$

By setting this equal to zero in order to find the maximum the following equation is obtained, which, when solved for ω, allows the resonant frequency to be identified by solving

$$0 = \frac{jL_0k' - j\omega^2C_0L_0^2k'^2 + 2j\omega^2C_0L_0^2k'^2}{\left(1-\omega^2C_0L_0k'\right)^2}. \tag{2.102}$$

By setting the numerator of this equation equal to zero, and ensuring that the denominator is non zero, the equation can be solved to give,

$$\omega^2 = \frac{-jL_0k'}{jC_0L_0^2k'^2} \tag{2.103}$$

and hence the resonant frequency is,

$$\omega_1 = j\sqrt{\frac{1}{C_0L_0k'}}. \tag{2.104}$$

The presence of the imaginary number j is due to the way in which k' is defined. The impedance at resonance as a function of k' can also be calculated by substituting the solution for ω into equation 2.94, giving

$$\begin{aligned} Z_1 &= \frac{j\omega L_0k'}{1-\omega^2C_0L_0k'}, \\ &= \frac{-\sqrt{\frac{1}{C_0L_0k'}}L_0k'}{1+\frac{1}{C_0L_0k'}C_0L_0k'} \\ &= -\sqrt{\frac{L_0k'}{4C_0}}. \end{aligned} \tag{2.105}$$

An example of using these equations to calculate the resonant frequency and the impedance at resonance is given in figure 2.15 comparing the analytical solutions to the numerical solution of equation 2.94. In this case the resonant frequency and the impedance at resonance as a function of coupling coefficient have been calculated analytically for a coil with a capacitance of 8 nF and an inductance of 180 µH have been calculated, and these are compared with the numerical solutions in figures 2.15 (a) and (b). These figures show excellent agreement, and demonstrate the validity of the calculations.

Although the change in the resonant frequency and impedance at resonance as a function of coupling coefficient can be analytically described using these equations, the change in these values as a function of lift-off are not. This is due to the fact that the relationship between the lift-off and the coupling-coefficient is unknown, however, there is sufficient evidence that changes in the lift-off will measurably change the impedance in the coil [93, 94, 141, 142]. This will allow a measurement

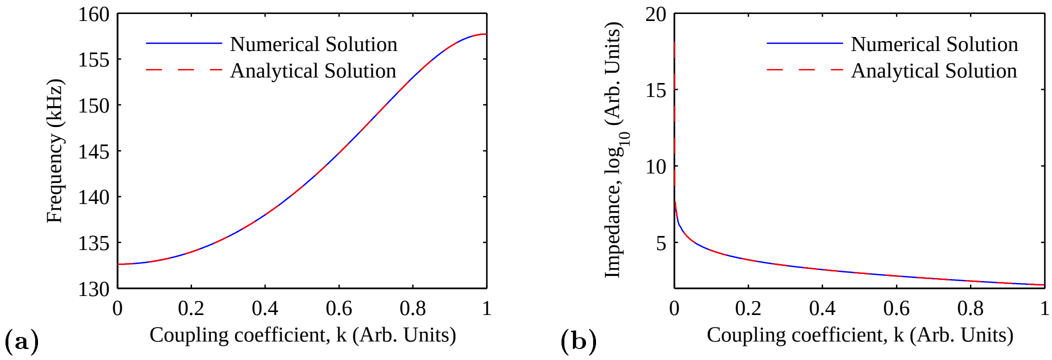

Figure 2.15: Comparison between analytical solutions of the equivalent circuit model and their numerical solutions as the coupling coefficient varies for (a) the resonant frequency, and (b) the impedance at resonance.

of the lift-off to be made by measuring the change in the impedance of the coil, which is discussed in more detail in chapters 7 to 10.

Chapter 3

Lamb Waves: Experimental Details

This chapter covers the experimental approach to testing and using the combined approximation discussed in section 2.2.3 in order to perform thickness measurements on metal sheets without knowledge of the material properties of the sample. The experimental work focuses on measurements of the phase velocity, and using those phase velocity measurements to provide calibrationless thickness measurements. The phase difference spectrum (PDS, discussed in section 2.4) between two closely spaced measurement positions is used to calculate the phase velocity of the dispersive A_0 wave, which is then used in conjunction with the phase velocity of the S_0 wave in order to calculate the thickness of the sample between the two measurement positions. The acquisition of measurements from closely spaced positions is discussed in this chapter, as are the EMAT designs used. The change from simple EMATs using broadband generation, to more specialised EMATs with narrow-band signals throughout the course of this research will also be discussed.

3.1 Acquisition of multiple measurements

The application of the long wavelength approximation to thickness gauging has been previously reported by Dewhurst [55]. However, this paper uses the group velocity version of the long wavelength approximation, whereas the measurements in this research is concerned with the phase velocity. These phase velocity measurements require the two closely spaced measurements, which are obtained by scanning the detection EMAT across the surface of the sample while the generation EMAT was held in a constant position, creating a large number of individual A-scan measurements, as can be seen in figure 3.1. It is important to note that the phase velocity measurements, and thus the thickness measurements in which they are used, are an average over the area between the two measurement positions. Therefore having a large number of individual measurement

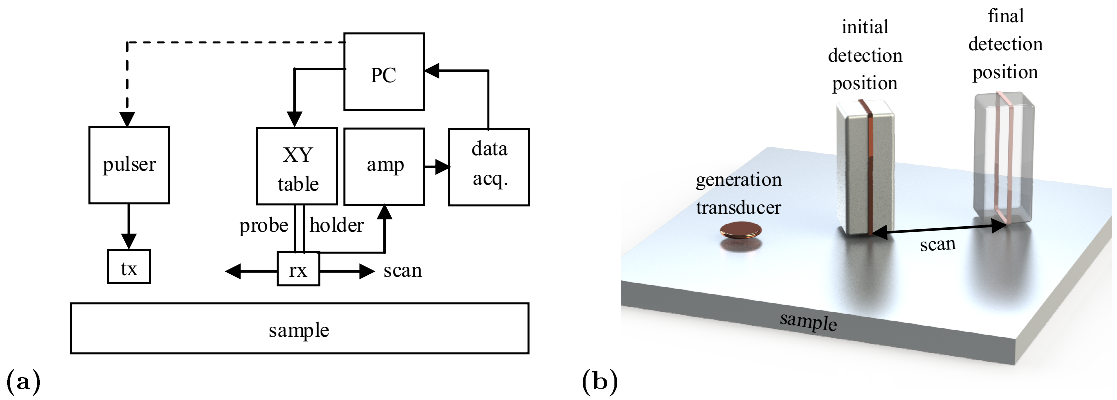

Figure 3.1: A schematic diagram of the scanning arrangement showing (a) the experimental set-up, including the computer control of the XY table, which scans the detection transducer across the sample while keeping the generation transducer fixed, and (b) the angle of the scan relative to the edge of the sample in order to minimise edge reflections.

positions allows the thickness profile across the sheet to be measured. This is also important for proving the reliability of the measurements, as the previous work by Dewhurst considered only one measurement for each sample [55]. The consistency of the measurements across the length of the sample will be extremely important in demonstrating the repeatability of the measurement which would be key for any industrial application. The scanning of the detection transducer was performed using a stepper motor driven XY table, where the individual step size of the table is 50 μm, although measurement positions were typically taken at 100 μm intervals. The mean step size of the XY table was confirmed by measuring the distance travelled for 4000 steps, although the variation between individual steps could be considerable. The XY table was controlled using a PC, which also controlled the data acquisition, and in some of the measurements, the pulse generator. As shown in figure 3.1(b), the scanning axis along the sheet was at a skewed angle relative to the edge of the sheet, which was done in order to minimise the effects of spurious edge reflections of the S_0 wave on the phase velocity measurements of the A_0 wave. Although the initial separation of the transducers, as well as the scan length, varied throughout the course of this research, the initial separation was typically in the region of 80 to 120 mm, while the scan length was between 80 and 100 mm.

3.2 EMAT Design

During the course of this research a number of EMAT designs have been used for both generation and detection, and these have been designed to have predominantly an out-of-plane orientation in their Lorentz force, in order to preferentially generate the A_0 wave. This is due to the distribution of energy in the long wavelength Lamb waves shown in figure 2.10, where it can be seen that the A_0 wave at the frequency thickness of interest consists almost entirely of out-of-plane displacement. In addition to the linear and spiral coil EMATs discussed in section 2.3.3, which have been used in the broadband measurements, several periodic EMATs have also been designed and produced in order to increase the efficiency of narrow-band generation. By using periodic EMATs, where the spatial frequency of the EMAT matches the wavelength of the Lamb wave to be generated at a certain frequency, the efficiency of the generation can be greatly increased [52, 146].

3.2.1 Generation EMATs

The generation EMATs are separated into two main categories depending on whether the EMAT was designed to generate in conjunction with a broadband pulse, or via a narrow-band tone burst. The two broadband EMATs suitable for generation have been discussed briefly in section 2.3.3, but the exact construction of the linear and spiral coils used is elaborated upon here.

For the generation EMAT in the initial experiments a linear coil was used (shown in figure 2.11 (a)), which consisted of 4 turns of 0.315 mm wire, wrapped in a loop around two 12 mm cubic magnets arranged with the north-south axis parallel to the surface of the sample. The relatively thick wire gauge served to protect the EMAT from damage due to ohmic heating as a result of the large current passed through the coil [126]. The front face of the EMATs were protected by a lip on the edge of the transducer housing, which kept the coil recessed from the sample. Although this simple design was sufficient for laboratory based experiments, more complex steps must be taken in an industrial environment, such as adding a ceramic wear face to the EMAT. Unfortunately, due to the relatively small number of turns of wire in proximity to the surface of the sample the induced eddy currents, and thus the Lamb wave amplitudes, were relatively small. In addition, the small size of the cubic magnets caused a number of edge effects to be introduced into the generated Lamb waves. Although the use of larger magnets would improve the signal to noise of the generated ultrasound, as well as reduce the significance of any edge effects, a different strategy was pursued in order to limit the size of the magnets used, as these can often attract swarf and other metal debris in an industrial environment.

In order to increase the amplitude of the Lamb waves generated, an alternative coil design was used which increased the eddy current density in the surface of the sample. This was achieved using a spiral coil consisting of 20 turns of 0.315 mm wire, with a ferrite backing plate designed to enhance the self field of the coil [127]. An additional benefit of using the spiral coil was that the impact of edge effects was greatly reduced, where the edge effects are attributed to the interaction of the eddy currents in the surface of the sample with the static bias field at the edges of the linear coil transducer. These interactions are undesirable, as the bias field is not uniform, particularly towards the edges of the magnet, and can lead to unintended in-plane generation forces [118].

The narrow-band EMATs were designed to have a periodicity of 9 mm, which satisfies the criterion that for the combined approximation that the wavelength of the ultrasound be much larger than the thickness of the sample. The first EMAT designed in with this periodicity was a meander coil, which had no bias field and relied entirely on the self field of the coil in order to generate an out-of-plane displacement. The self field was enhanced using a ferrite backing material. The coil is only capable of producing a repulsive force, as discussed in section 2.3.1.1, as the Lorentz force of the dynamic magnetic field produced by the coil and the eddy currents induced in the surface of a conductive sample will always act in the same direction [119]. Although the effect of the dynamic field on the generation of acoustic waves using meander coils as a complement to the static bias fields has been discussed [147], it is believed that the reliance solely upon the dynamic field, enhanced by a ferrite, is a novel method of generating periodic out-of-plane forces in order to excite Lamb waves. The interdigital spacing of the meander coil is equal to the wavelength, due to the solely repulsive nature of the Lorentz force, as shown in figure 3.2 (a). The meander coil initially used consisted of 5 turns of 0.15 mm diameter wire, where the decrease in wire gauge used in comparison to the broadband coils is due to the decrease in power of the generation electronics used for the narrow-band signals. The number of turns in the coil is a separate characteristic from the number of wavelengths of the meander coil, and effectively is the number of times the coil shown in figure 3.2 (a) is superposed.

Due to the periodicity of the EMAT being equal to the wavelength, the size of this meander coil was quite large, for the coil pictured a length of 45 mm, and an alternative design was explored. This novel design uses a racetrack coil in conjunction with a periodic permanent magnet (PPM) array, and is similar to those used to produce SH waves [111]. A schematic diagram showing the alternating field of the PPM array EMAT is shown in figure 3.2 (b). The magnets are arranged to ensure that the static field is parallel to the surface of the sample, which interacts with the induced current created by a coil, in order to provide an out-of-plane displacement which alternates with the same periodicity as the array. The EMAT used in this research was constructed using 4 mm cubic magnets, with 0.5 mm alumina spacers, the kerf k in the diagram, between the magnets. The sum of the magnet size and the kerf, 4.5 mm, is shown as d in the diagram, and due to the alternating polarity of the magnets this causes the periodicity of the PPM EMAT to be 9 mm. A racetrack coil, named for its elliptic shape, is used in the EMAT and consists of 20 turns of 0.15 mm wire. In addition to reducing the footprint of the coil from 5λ to 3λ this coil generated the out of plane Lamb waves more efficiently than the meander coil, as a meander coil at this

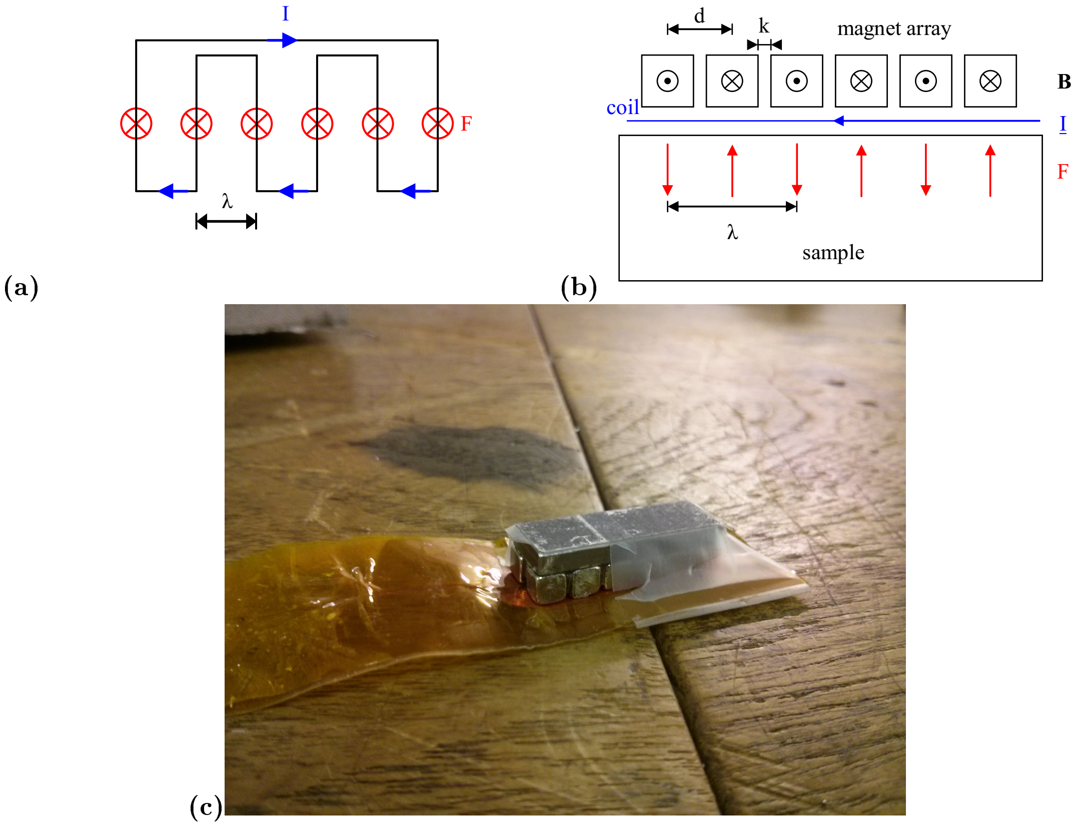

Figure 3.2: A schematic diagram of the EMATs used to generate out-of-plane displacements with narrow-band signal showing (a) a top down view of a self field meander coil, (b) a side view of a PPM EMAT with a racetrack coil, and (c) a picture of the PPM EMAT without a protective housing.

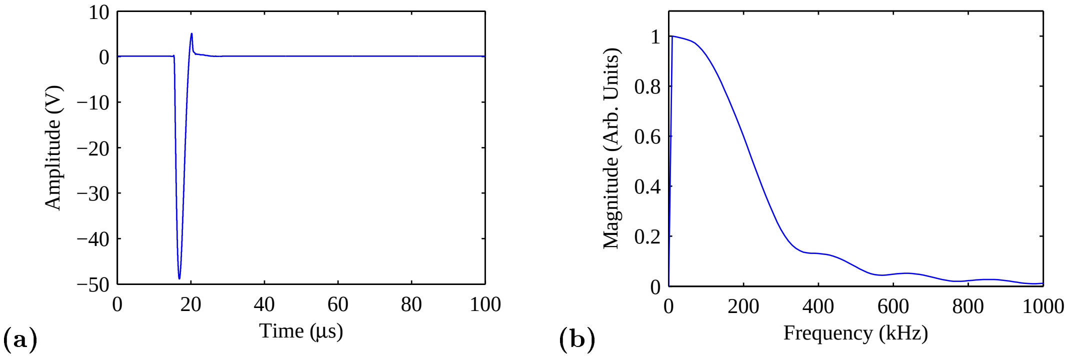

Figure 3.3: Characteristics of the broadband generation pulse in (a) the time domain, and (b) the frequency domain.

length would have produced considerably less energy than the PPM array EMAT.

3.2.2 Generation electronics

The generation electronics required varied depending on the type of signal that was used, either broadband or narrow-band. The broadband signals were generated using a capacitor discharge, where the time domain signal and respective frequency content are shown in figure 3.3 (a) and (b) respectively. The short time duration of the broadband pulse ensures that it has a large spread in the frequency domain, as can be seen in (b), although the large majority of the signal energy lies in the region below 300 kHz. The measured amplitude of the pulse is much smaller than the actual amplitude, as the amplitude of the pulse was measured using an oscilloscope directly after being passed thorough the high voltage attenuator. This is a direct measurement of the pulse of the signal generator, rather than one obtained by inductive coupling to the generation cable, although the amplitude is greatly decreased by the attenuator in order to avoid damaging the measurement oscilloscope.

The narrow-band signal was generated using a Ritec PR-4000 tone burst generator, and an example of the tone burst generated at 100 kHz with both one and five cycles is shown in figure 3.4 (a), obtained from the pulse monitoring channel of the Ritec, while the frequency content of the pulses is shown in (b). The spikes seen in the time domain data are artefacts of the generator, and will introduce some high frequency noise into the generated ultrasound. By increasing the number of generation cycles it can be seen that the frequency bandwidth of the signal can be reduced, with the five cycle pulse having a much sharper peak in the frequency domain. The amplitude of the narrow-band signal shown here is considerably smaller than the amplitude of the signal produced using the broadband source which allows finer gauge wires to be used in the construction of the narrow-band generation transducers.

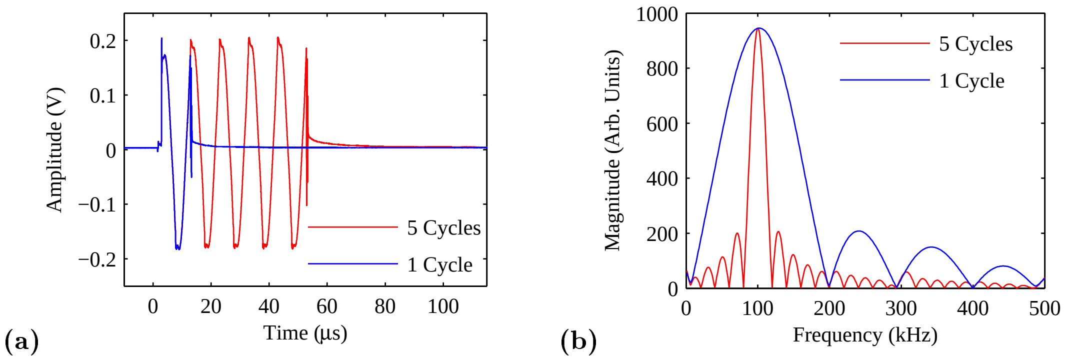

Figure 3.4: Characteristics of the narrow-band generation pulse in (a) the time domain, and (b) the frequency domain, where the peak amplitude of the signals is normalised. The single cycle data is shown in blue, while the five cycle signal is shown in red.

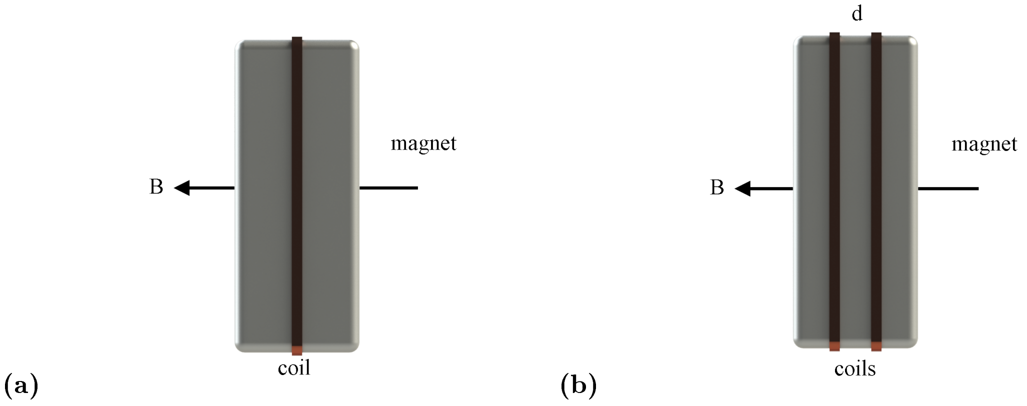

Figure 3.5: Schematic diagram of the detection transducers optimised for out-of-plane sensitivity, where the sample is parallel to the magnetic field, showing (a) a single channel transducer, and (b) a dual channel transducer.

3.2.3 Detection EMATs

As with the generation transducers, the detection EMATs have been constructed to ensure that the orientation of the Lorentz force is out-of-plane by using a linear coil in conjunction with a magnetic field which is parallel to the surface of the sample [148]. The motion of the ultrasonic wave in the presence of the bias field will generate eddy currents in the surface of the sample, which will be detected by the linear coil, where the arrangement of the bias field and the coil make the coil primarily sensitive to out-of-plane forces. The arrangement of the coil and magnetic field can be seen in figure 3.5 (a). The initial detection EMAT was comprised of 10 turns of 0.08 mm wire, combined with two 12 mm cube magnets, arranged side by side to act as a single bar magnet with the bias field parallel to the surface of the sample in order to provide a sensitivity to out-of-plane displacements.

As per section 3.1, the detection EMAT was scanned across the XY table in order to determine the wave velocity between measurement positions. However, the reliability in the positioning of the XY table is not perfect, so the distance between any two measurement positions will have an uncertainty, which will lead to an uncertainty in the measured phase velocity between the measurement positions. The error in positioning due to the XY table can be eliminated by using a dual coil detection EMAT with a static distance between the two detection coils. This allows the phase velocity measurements at each of the coils to be compared, while there is a fixed distance between them, d, which should significantly increase the reliability of the measurement. A schematic diagram of this is shown in figure 3.5 (b); the construction of the EMAT the two detection coils must be as similar as possible. The linear coils for the dual channel detection EMAT were both constructed using 10 turns of 0.08 mm thick wire, while the spacing between the coils was 8 mm. The coils are arranged symmetrically about the centre of the magnet in order to ensure that the magnetic field in the areas of the sample where the coils are sensitive is as similar as possible. The dual coil EMAT was used in later measurements in an attempt to overcome uncertainties in the positional reliability of the XY table, as well as a representation of the most likely implementation of the measurement technique in an industrial environment, removing the need to precisely actuate a single transducer over a sample.

Chapter 4

Thickness measurements using low frequency Lamb waves

As discussed in section 2.2.3, low frequency Lamb waves can be used to perform thickness measurements without *a priori* knowledge of the material properties by comparing the wave velocities of the dispersive A_0 wave and the non-dispersive S_0 wave at long wavelengths compared to the thickness of the sample [55]. This chapter describes the initial experimental results obtained when using the combined approximation described by equation 2.65 on aluminium samples. The range of validity of the approximation with respect to the Lamb wave frequency and the thickness of the sample is considered, and the results of this are used to select the sample thickness and frequency range for subsequent measurements. Two approaches are taken in parallel: investigating the application of both broadband and narrow-band Lamb waves to thickness measurements using the combined approximation [55]. Although the results of previous measurements by Dewhurst are encouraging, the validity of the approximation has not previously been comprehensively examined, and the reliability of the technique is unknown. The rigour required to demonstrate and evaluate the reliability of this method is extremely important in developing this technique for industrial applications. Thus in this research, the robustness and applicability of the technique is quantified and improved, and the region of validity of the approximation is explored.

4.1 Validity of the Combined Approximation

The combined approximation discussed in section 2.2.3 is only valid in regions where the wavelength of the Lamb wave is much larger than the thickness of the sheet in which it propagates. The two approximations for thickness, d, given by measuring the velocities of the symmetric (C_S) and antisymmetric (C_A) waves, using either the phase or the group velocity respectively, can be rearranged to directly calculate the sample thickness,

$$d = \frac{\sqrt{3}}{\pi f}\frac{C_A^2}{C_S}, \tag{4.1}$$

$$d = \frac{\sqrt{3}}{4\pi f}\frac{C_{Ag}^2}{C_{Sg}}, \tag{4.2}$$

where f is the frequency and the subscript g denotes the use of the group velocity (also presented in equations 2.65 and 2.67). The thickness measured when using equations 4.1 and 4.2 will have an associated error that results from the fact that the equations used are approximations, and hence it is important to consider the range of validity of these approximations. In order to define this range of validity, the acceptable error in the thickness measurements must first be selected, considering the inherent error which occurs not due to experimental uncertainty, but due to the use of the approximations themselves. In this research the acceptable error in the approximation is limited to 1 %, as this level of uncertainty is considered acceptable in most industrial applications, and is likely to be less than the error due to experimental uncertainty in measuring the sound velocities of the Lamb waves. In applications where a different value for the acceptable error can be considered, for either a smaller error when a more precise measurement is required, or a larger error when a greater tolerance in the uncertainty is present, it would be relatively straightforward to reassess the range of validity.

In order to assess the validity of the combined approximation it was tested with numerically calculated velocity values from the dispersion curves. For a 1 mm thick aluminium sample the dispersion curves, such as those shown in figure 2.5, were calculated using equation 2.46, considering only the frequencies, phase velocities and group velocities of the A_0 and S_0 waves.

These velocity and frequency values were then input into equations 4.1 and 4.2 for the phase and group velocities respectively to represent a idealised velocity measurement (with no experimental error) and the thickness of the sheet was calculated. This provides a measured thickness for both the phase and group velocity approximations which varies as a function of frequency, and can be compared to the true thickness of 1 mm to find the disparity between the two values. The accuracy of the approximation, which is the agreement between the measured thickness and the actual thickness, expressed as a percentage of the actual thickness, is plotted as a function of the frequency thickness product in figure 4.1.

The accuracy of both the phase and group velocity measurements decrease as the frequency thickness increases, shown by the move away from 100 % accuracy in figure 4.1 as the frequency thickness increases from zero, although the accuracy of the group velocity decreases at a much greater rate. Considering the acceptable error of 1 %, the point at which the accuracy drops below 99 % gives the upper limit of the range of validity, which for the phase velocity is 14.1 kHz.mm. The limit of the range of validity for the group velocity is considerably lower, at 4.70 kHz.mm. Although the dispersion curves were calculated using a 1 mm thick sheet the frequency thickness axis allows a limit to the operating frequency to be defined for a sample of any thickness. Considering a 100 µm thick sheet, the upper limit of frequency of the signal for a 1 % error in thickness when using the phase velocity approximation is 141 kHz, compared to 47 kHz using the group velocity approximation. This low region of validity for the group velocity measurements explains the limitations in the accuracy of the measurements performed by Dewhurst [55], as discussed in section 2.2.3.

As discussed in section 2.2.3, and demonstrated in figure 4.1, the validity of the approximation is limited to very small values of frequency thickness where the wavelength of the Lamb wave is considerably longer than the thickness of the sample. Due to this limitation both the thickness of the sample and the frequency of inspection must be carefully considered when planning actual measurements. Additionally, the inspection protocol must consider the relative performance of the measurements using the phase and group velocities, with the phase velocity being roughly three times as accurate as the group velocity.

A simple measurement of the group velocity, using a single measurement to find the average wave velocity between the generation position and the measurement position, will thus measure the average thickness in this region. While this method would have an advantage in the simplicity of the technique, and in application of the measurement technique to existing tomographical techniques [149], for this research accurate measurements over a small region were prioritised. For these

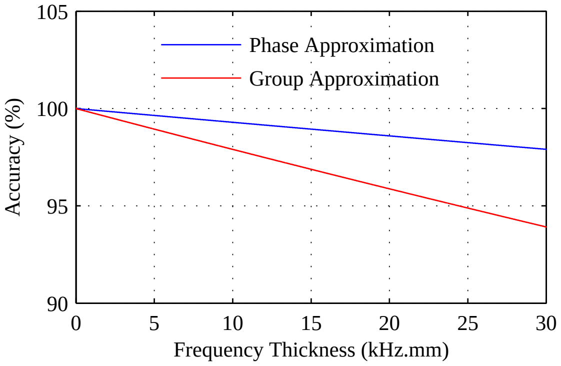

Figure 4.1: The accuracy of the combined approximation as a function of the frequency thickness. The region of validity is defined as an accuracy in excess of 99 %, which for the phase velocity corresponds to frequency thicknesses below 14.1 kHz.mm, while for the group velocity this limit falls to 4.70 kHz.mm.

reasons the implementation of the approximation using the phase velocity was chosen, in spite of the more complex analysis required, to give a wider region of validity for the frequency thickness, and to simplify the generation of the frequencies required for the sample thicknesses investigated.

4.2 Thickness measurements using broadband Lamb waves

The limitations to the validity of the approximation must be carefully considered during its use. Investigations have been performed previously into the performance of the approximation when using broadband Lamb waves [55], however, these only considered the group velocity of the waves, due to the complexity involved in performing phase velocity measurements. Based on the data shown in figure 4.1, the more accurate phase velocity approximation has been selected for this work. The limitations of the broadband signal generator used, which can be seen in figure 3.3 to have significant frequency content up to 300 kHz, mean that for the 100 µm thick aluminium sample used in this work a portion of the frequency spectrum will fall outside of the 1 % range of validity. However, for a frequency of up to 287 kHz the approximation can be considered valid to an accuracy of 2 % for a 100 µm sheet, which covers the large majority of the frequency bandwidth of the generator.

The aluminium samples used in this work were sourced from Advent RM at a tolerance of 10 % of the nominal thickness. However, the thickness of the sheets was confirmed with a calibrated micrometer to be 100 ± 1 µm, while the composition of the aluminium is 99.5 % pure, with impurities unlisted.

For this experiment the generation transducer used was an EMAT consisting of a ferrite backed spiral coil, which relied entirely upon the dynamic field created by the current flowing in the coil in order to create a Lorentz force within the sample, as discussed in section 3.2.1. The lack of bias field for the generation transducer was selected in order to preferentially generate ultrasound with out-of-plane displacement [118], which is the predominant orientation of motion in the A_0 wave for the frequency thickness used here, as described in section 2.2.2. The detection transducer was a linear coil, arranged with a bias magnet with the north-south axis parallel to the surface of the sample in order to create an EMAT which was mostly sensitive to out-of-plane motion [150], described in detail in section 3.2.3.

As described in section 3.1 the generation transducer was held at a fixed position on the sample, while the separation between the generation and detection transducers was gradually increased from 100 to 200 mm in steps of 100 µm. The ultrasound data was captured at each position using a computer controlled digital oscilloscope. The individual time domain signals from each

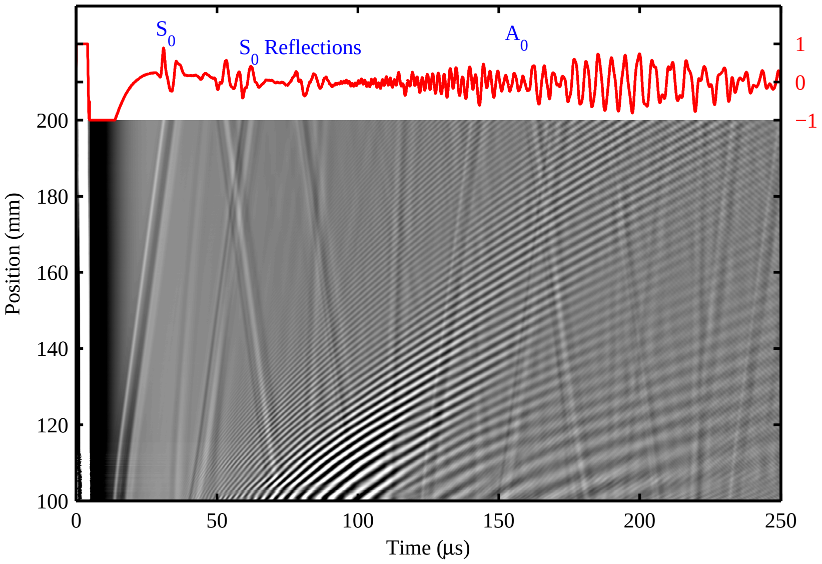

Figure 4.2: B-scan of the broadband measurement, with the A-scan for the measurement at 200 mm shown in red at the top of the figure. The S_0 and A_0 waves are labelled in blue, and the presence of multiple S_0 wave reflections can be seen from the B-scan.

measurement position are known as A-scans, an example of which is shown in red in figure 4.2. The grayscale image shown beneath the A-scan is a collection of all the individual A-scans arranged by measurement position, where the colour represents the amplitude of the A-scans, ranging from black at the minimum amplitude, to white at the maximum; this is a B-scan. The figure shows the faster travelling S_0 wave, as well as its reflections from the edge of the sheet, and the slower, dispersive A_0 wave. The increasing separation between the transducers leads to the slope of the S_0 wave, where the gradient of the line is equal to the group velocity of the wave, which due to the non-dispersive nature of the S_0 wave at this frequency thickness is equivalent to the phase velocity. The dispersive nature of the A_0 wave can be seen in figure 4.2 by the difference between the arrivals of the peaks of the wave, which is the striped pattern within the wave, and the wave packet itself, the area of brightness in the figure showing the energy of the wave. This clearly shows the difference between the group velocity of the A_0 wave and its phase velocity (section 2.1.1.3). Multiple reflections of the S_0 wave from the edge of the sheet can also be seen throughout the B-scan image, arriving after the faster S_0 wave, and during the arrival time of the A_0 wave. Any differences in the gradient of these waves are dependent on the paths through the sample along which the waves propagated. The arrival of the reflected S_0 waves is likely to disrupt the measured phase of the A_0 wave, which could lead to uncertainties in the thickness measurements using those measurements.

In order to calculate the thickness of the aluminium sheet using the combined approximation,

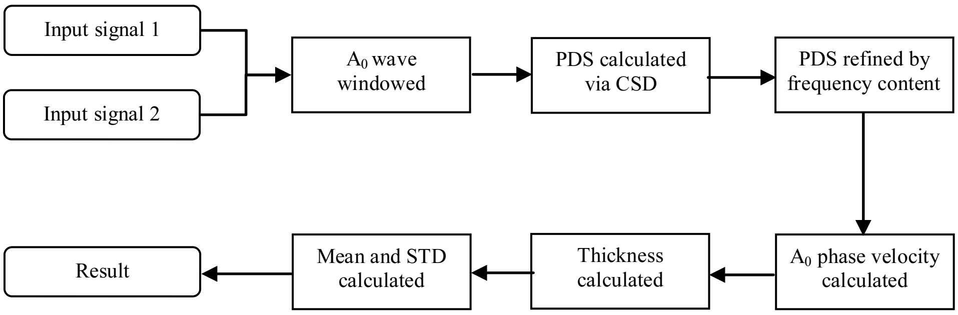

Figure 4.3: A flow chart describing the steps in the signal processing algorithm used to calculate the thickness of the sheet. The definitions of the acronyms used in this figure are phase difference spectrum (PDS), cross spectral density (CSD), and standard deviation (STD).

the phase velocities of the S_0 and A_0 waves must be measured. For the S_0 wave this is relatively simple, as the time difference between the peaks of the S_0 wave in the A-scans at different positions is easy to measure. From this measured time difference, and the knowledge of the distance between the measurement positions the S_0 wave velocity can be calculated. The average velocity measured during the scan over the 100 µm thick aluminium sample is 5521 ± 8 ms^{-1}. This value is reasonable when compared to the value suggested by the theoretical dispersion curves for this frequency thickness, 5431 ms^{-1}, calculated for aluminium with longitudinal velocity of 6374 ms^{-1}, and a transverse velocity of 3111 ms^{-1} [151]. The disparity between the two values is most likely due to a difference in the longitudinal and transverse sound velocities in this sample, which could be a result of the texture of the sample [11], or a variation in its composition.

Measurement of the A_0 phase velocity is more complicated, owing to the dispersive nature of the wave, and requires a more complex analysis of two measurement signals from closely spaced positions. This allows the phase difference spectrum to be calculated between the two positions, as discussed in section 2.4, and the analysis performed on these two measurements is described by the flow chart in figure 4.3. The flow chart describes the individual steps that comprise the thickness measurement algorithm, and each individual step is discussed in detail in the following paragraphs.

The A_0 wave packets for each of the two A-scans were windowed in the time domain, as shown in figure 4.4 for measurements taken at separations of 150 and 154 mm. The window of each A-scan is taken over the same time period, with the same start time and window length for both measurements, in order to allow the phase spectra to be directly comparable. The variation in the phase between the two measurements as a function of frequency can be seen by eye, with the

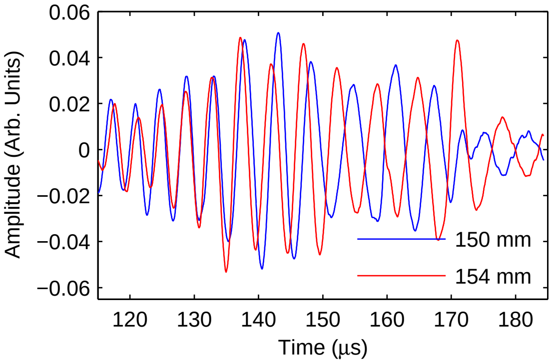

Figure 4.4: The time windowed A_0 wave at two measurement positions, 150 mm in blue, and 154 mm in red.

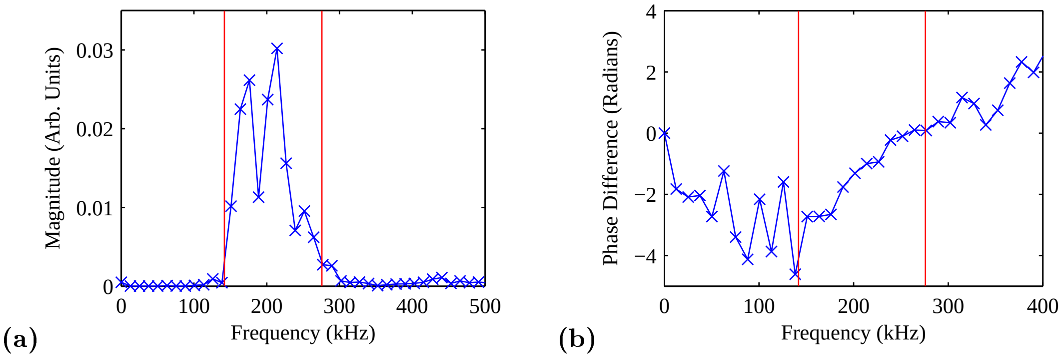

Figure 4.5: (a) The magnitude of the CSD, and (b) unwrapped phase difference spectrum. The red lines denote the edges of the regions where there is significant frequency content in both of the A_0 waves, and thus the region where there is meaningful phase information.

higher frequency waves arriving between 120 and 150 µs being in much better phase agreement than the low frequency waves which arrive later. By considering equation 2.76, discussed in section 2.4.2, the calculation of the phase velocity requires knowledge of the unwrapped phase difference spectrum (PDS), which can be calculated by taking the difference between the unwrapped phase spectra at two separate measurement positions. However, as discussed in section 2.4.2, the PDS can also be calculated using the cross spectral density (CSD), which is the technique used here. The unwrapping of this spectrum was calculated using the difference detection method, again discussed in further detail in section 2.4.

The magnitude and argument of the CSD for the windowed sections of the two A-scans (shown in figure 4.4) are presented in figure 4.5 (a) and (b) respectively. The magnitude is a measure of the frequency content of both signals, while the argument is the phase difference spectrum. This PDS is only meaningful in regions where the signal has frequency content, and here that is defined as the region where the magnitude of the CSD is at least 10 % of the maximum magnitude of the CSD, which is shown in the figure by the red vertical lines. Over the region where there is meaningful phase information the phase difference spectrum is well behaved, increasing smoothly as frequency increases, however the phase values of the PDS below 138 kHz is unknown, due to the lack of frequency content in this region. The PDS between the two red lines is used to calculate the frequency dependent phase velocity using equation 2.76, repeated here for ease of reference,

$$C_p\left(f\right) = \frac{2\pi f x}{\triangle\phi\left(f\right) + 2\pi n}, \tag{4.3}$$

where the uncertainty in the starting phase of the PDS is dealt with by with the inclusion of the term $2\pi n$ in the denominator. In order to ensure that the correct value of n is chosen, the phase velocity is calculated as a function of frequency for a range of n values. The correct value of n is selected as that at which the resulting thickness calculation is closest to the nominal thickness of the sample, where the next nearest values of n have a significant effect on the measured thickness, in this case the closer value differs by over 30 µm, while the other value differs by over 60 µm. The phase velocity for this value of n is shown in figure 4.6 (a), along with the calculated phase velocity given by the dispersion curves for this material. The calculated phase velocity, which is shown in red, is in excellent agreement with the measured phase velocity over the frequency region where the phase of the signal has frequency content.

From each point of the frequency dependent phase velocity a thickness can be calculated using equation 4.1, and for each value n used in equation 4.3. A plot of the thickness values for the correct value of n, here chosen to be 2, can be seen in figure 4.6 (b), as well as a line corresponding the nominal thickness of 100 µm (the black dashed line) and the thickness which would be measured by the approximation with perfect knowledge of the phase velocities and no experimental uncertainties (the red dashed line). For each value of n the thickness is then averaged across the frequency range to give the measured value for this pair of measurement positions, and the standard deviation of the measured thickness is also calculated. This thickness measurement is reasonably self-consistent across the frequency range, although there is one outlier at 176 kHz which appears to be the result of the dependence of the thickness on the square of the A_0 phase velocity, so that small discrepancies in the phase velocity are amplified in the thickness measurement. Despite the frequencies used in this experiment exceeding the range of validity of the approximation for an aluminium sample of this thickness, the variation in the measured thickness is much larger than the difference between the nominal thickness and the thickness as measured by the approximation. This implies that the largest limitation to the accuracy of the method over this region of frequency thickness is the experimental measurement of the phase velocities, rather than the inherent inaccuracy in the approximation. For this pair of measurement positions the thickness given by the average across

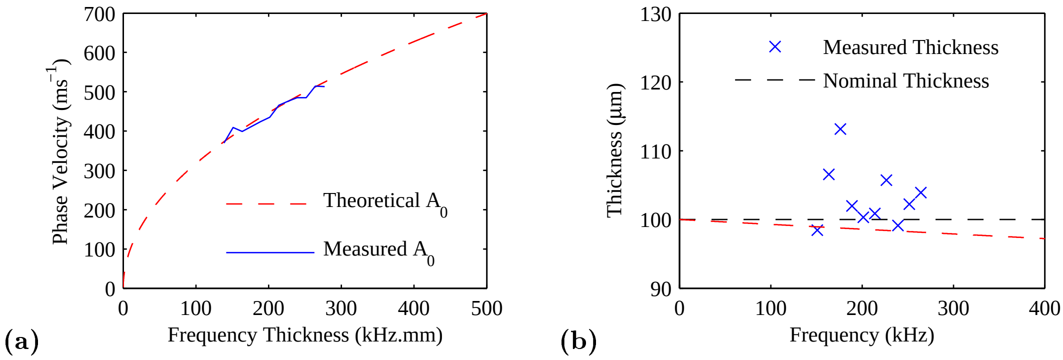

Figure 4.6: A plot of the frequency-dependent phase velocity of the A_0 wave, (a), along with the theoretical dispersion curve for aluminium at a mean transducer separation of 152 mm. The frequency dependent thickness calculated from the phase velocity is shown in (b) together with the nominal thickness of the sheet, as well as the sheet thickness that would be measured by the approximation with perfect knowledge of the phase velocities.

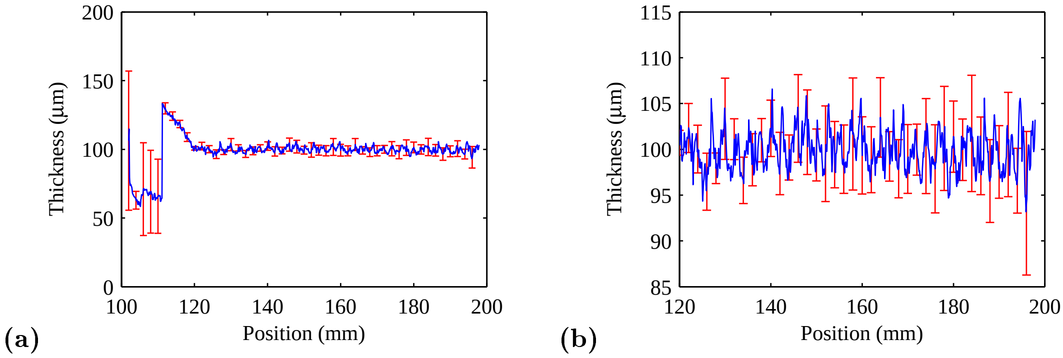

Figure 4.7: (a) The measured thickness of the sheet along the length of the scan, (b) enlargement of the data after 120 mm. The thickness measured across the whole sheet is 98.4 ± 11.9 µm, while focusing on the data at transducer separations greater than 120 mm the measured thickness is 99.9 ± 2.1 µm.

the frequency range, and the uncertainty from the standard deviation, is 103.2 ± 4.4 µm, which is in good agreement with the thickness of the sheet.

The thickness measurement given by this pair of A-scans is the average thickness of the sample over the 4 mm distance between the two positions, and the location of the measurement is set as being midway between the two measurement positions, at a transducer separation of 152 mm. The thickness was also calculated for all possible pairs of measurement positions separated by 4 mm over the whole scan, from a separation between the generation and detection transducers of 100 to 200 mm, and the results of the measurements during this scan are plotted against position in figure 4.7 (a). The error bars are plotted for every twentieth measurement in order to give a representation of the uncertainty in the measurements. The average thickness across the sheet is 98.4 ± 11.9 µm, where the uncertainty is provided by the standard deviation of the thickness measurements at each measurement position and all points in the scan are included in this measurement. While the average measurements is in good agreement with the nominal thickness of the sheet, the uncertainty in the measurement is quite large. This is due to the large change in the measurement at the beginning of the scan, in the region of the scan below 120 mm separation.

The physical cause of the poor performance in this region is twofold, and is due to issues with the positional accuracy of the transducer, and the reflections of the S_0 wave interfering with the A_0 wave. The initial measurements of the thickness occur in the region where the backlash in the actuation system has not been accounted for. This backlash is an effect when actuating a mechanical system whereby changing the direction of motion there is a certain amount of slack that must be recovered before the actuation starts in the alternative direction [152]. As the XY table was reset to the starting position before the scanning commenced in the opposite direction there is some backlash in this system at the start of each scan, and hence the separation between the analysed scans is likely to be different from the expected value of 4 mm in this region. This will result in errors in the calculation of the phase velocity, due to the uncertain translation of the probe in this region. The errors in the phase velocity measurements in this region will propagate to become errors in the thickness measurements, as seen in figure 4.7. The other contributing factor in the uncertainty of the thickness measurements, which will be the dominant factor in the frequency-dependent measurements, is the disruptive effects of the S_0 wave reflections on the phase spectrum of the A_0 wave. This can be seen in figure 4.2, where in the region of separations of less than 120 mm there are a number of instances of S_0 wave reflections arriving simultaneously with the A_0 wave. These reflected waves will have their own phase spectrum, which will superimpose with the phase spectrum of the A_0 wave, causing uncertainties in the measured phase of the A_0 wave. Although the uncertainties caused by backlash within the system could be reduced or removed by using a backlash compensated system to position the reception transducer, the variations caused by reflections are more difficult to compensate for.

By ignoring the measurements of the thickness in the region below 120 mm, and ensuring the analysis is done in a region where the effects of backlash and multiple reflections are minimised, the agreement between the measured thickness and the nominal thickness improves greatly, as shown in figure 4.7 (b). The thickness measured when considering only this region is 99.9 ± 2.1 μm, which is in excellent agreement with the nominal thickness of the sheet, and shows a much improved uncertainty. The uncertainty in the measurements in this region is still affected by the precision of the XY stage and the disruption to the phase of the A_0 wave due to the reflections of the S_0 wave, but to a lesser extent. In this region the precision of the stage will affect the reliability of the distance measurements between the measurement positions, introducing an effect into the thickness measurements. The disruptions to the phase due to reflections will have a similar, although less

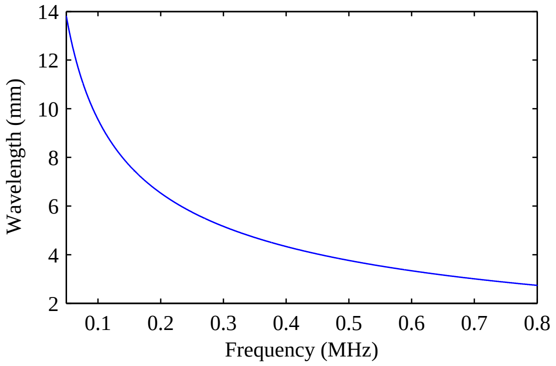

Figure 4.8: Wavelength of the A_0 wave as a function of frequency in a 100 µm thick aluminium sheet.

severe, effect to the those before 120 mm separation, as can be seen from the B-scan in figure 4.2 the intensity of the reflected S_0 waves arriving concurrently with the A_0 wave is reduced as the transducer separation increases.

4.3 Narrow-band Results

A further contributor to errors in the results is the possibility of the phase unwrapping procedure introducing errors into the phase difference spectrum of the signals, and removing this step will allow an improved measurement. By using a narrow-band signal this process of unwrapping the phase of the signal becomes unnecessary, which allows simpler computation of the phase difference and thus the thickness. Additionally, the mode selectivity of the narrow-band signal is likely to reduce the effects of the S_0 wave reflections interfering with the A_0 wave. For thickness measurements using narrow-band signals the broadband signal generator used in section 4.2 was replaced with a narrow-band generator, as discussed in section 3.2.2, which has a lower output power, and thus a modification to the generation transducer was also required. The spiral coil used in the broadband measurements was replaced with a ferrite backed meander coil, as discussed in section 3.2.1. The periodicity of the EMAT was chosen to be 9 mm in order to match the wavelength of the A_0 wave at a frequency of approximately 100 kHz, which is well within the region of validity of the approximation for a 100 µm thick aluminium sheet. The variation of the wavelength with frequency calculated using the dispersion curves in figure 2.5 is shown in figure 4.8. Due to variations in the texture or material composition of the aluminium sample, the wavelength does not correspond exactly with the frequency selected here, but the variations do not exceed the limit to the range of validity of the approximation, 14.1 kHz.mm (section 4.1).

Other than the change to the generation mechanism, the experiments using narrow-band Lamb

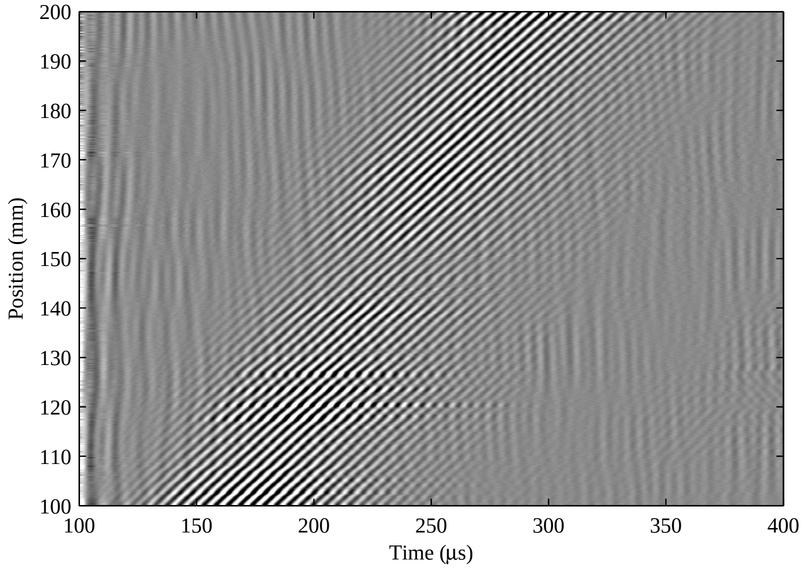

Figure 4.9: B-scan of the narrow-band measurements on a 0.1 mm thick sheet of aluminium. The initial 100 µs of the image is omitted, as the generation pulse dominates the signal in this region.

waves were conducted in the same manner as the experiments using broadband signals (section 4.2); the detection transducer was placed at a set initial separation from the generation transducer, which was held at a fixed position, and this separation was gradually increased from 100 to 200 mm, as discussed in section 3.1, with the data acquired at each separation. The data are then displayed as a B-scan, with an example shown in figure 4.9, which shows the raw data for a narrow-band measurement on a 100 µm thick sheet of aluminium. There are several key differences between this figure and figure 4.2. The time domain record begins at 100 µs as a result of the electrical cross-talk between the generation and reception transducers dominating the received data at times prior to this, as discussed in section 2.3.3. The increase in the significance of the cross talk is due to the change in generation; for broadband generation the EMAT is driven by a capacitor discharge, which is highly localised in the time domain but contains broad frequency content, and hence has a very short dead time. For narrow-band generation, a five-cycle sine wave is used, such as that shown in figure 3.4, which is highly localised in the frequency domain but is spread out in the time domain, and this has the effect of extending the region of dead time further into the received signal. This cross-talk has the effect of obscuring some of the wavemodes, particularly at low separation distances, namely the faster S_0 wave. The reflections of the S_0 wave from the edges of the sample can still be seen in figure 4.9, as can the narrow-band A_0 wave. The obfuscation of the S_0 wave by the generation pulse requires that the velocity of this wave be calculated using a secondary measurement, which although not a significant factor in this case, could become an issue in more time constrained measurements. This is performed in the same manner as described in section 4.2, where the S_0 wave was calculated using a broadband pulse generator and a spiral EMAT coil. Due to the non-dispersive nature of this wave the group velocity is equal to the phase velocity, and is independent of frequency. Thus this broadband measurement is a suitable measurement of the phase velocity and is performed as a separate measurement.

As with the broadband measurement, the phase velocity of the A_0 wave was calculated using information from two closely spaced measurement positions (4 mm separation) and used to determine the thickness of the material, using equation 4.1. The calculation of the phase velocity was performed in the same manner as the broadband measurements, using the algorithm described in figure 4.3. As before the phase difference spectrum (PDS) was calculated using the cross spectral density, where this was then used to calculate the phase velocity using equation 4.3, as with the broadband measurements (section 4.2). As the signal used in this measurement is narrow-band, unwrapping of the PDS is unnecessary as only the value of the PDS at a single frequency is considered, where the unknown phase before this frequency is accounted for in the $2\pi n$ term in equation 4.3. As with the broadband measurements in section 4.2 the A_0 and S_0 phase velocities are then used to calculate the thickness of the sheet using equation 4.1, although due to the electrical cross-talk the velocity of the S_0 wave was calculated from a separate measurement.

The uncertainty in the thickness measurements presented in section 4.2 was provided from the statistical distribution of the thickness measurements across the relevant frequency range. For the narrow-band measurements, however, the uncertainty was calculated from the propagation of the uncertainty in the phase velocity, ΔC_{RMS}, defined as [138]

$$\frac{\Delta C_{RMS}}{C} = \frac{1}{2\pi}\frac{|N_T(f)|}{|S(f)|}\frac{\lambda}{\Delta x}, \tag{4.4}$$

where C is the phase velocity, in this case of the A_0 wave, $|N_T(f)|$ is the absolute noise spectrum, $|S(f)|$ is the absolute signal spectrum, λ is the wavelength of the wave and Δx is the distance between measurement positions. By simple propagation of uncertainty, the uncertainty in the phase velocity is then used to calculate the uncertainty in the thickness using the following relation [153],

$$\frac{\Delta d}{d} = \sqrt{2\frac{\Delta C_A^2}{C_A^2} + \frac{\Delta C_S^2}{C_S^2}} \tag{4.5}$$

where ΔC_A is the uncertainty in the A_0 phase velocity calculated from equation 4.4 and ΔC_S is the uncertainty in the S_0 phase velocity.

The thickness measurements were performed for a scan of length 100 mm across the 100 μm

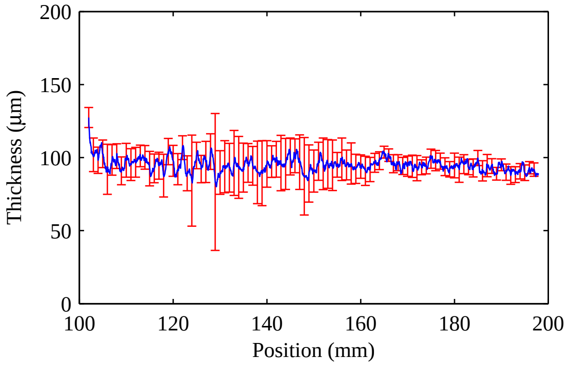

Figure 4.10: Thickness profile of a nominally 100 µm thick aluminium sheet using narrow-band signals. The average measured thickness along the length of the scan is 95.0 ± 4.6 µm, which is in reasonable agreement with the nominal thickness of the sheet.

thick aluminium sheet, starting at a separation distance between the measurement transducers of 100 mm, and the variation of the thickness with position is shown in figure 4.10. The average of the thickness measured across the length of the scan is 95.0 ± 4.6 µm, where the uncertainty is provided by the standard deviation of the measurements along the sheet.

The greatest limitation on the accuracy of this measurement is again the accuracy in the step size of the XY table. This can be seen in the B-scan in figure 4.9, where there are several discontinuities in the A_0 wave, for example at positions of 127 mm and 171 mm. These are due to the inconsistent positioning of the XY table during scanning. Any deviation between the expected distance between measurement positions and the actual distance between those positions will have a large effect on the accuracy of the thickness measurement as the calculation of both the S_0 and A_0 wave velocities is dependent on this distance. Another possible source of error in the measurement is again interference between the S_0 wave reflections and the A_0 wave, which could disrupt the phase of the A_0 wave sufficiently to introduce errors in the thickness measurements, although the generation transducer has been constructed in such a way as to minimise the strength of the S_0 wave produced (section 3.2.1) in order to reduce this effect.

4.4 Two Coil Approach

In order to overcome the main source of error in the measurements presented in sections 4.2 and 4.3, namely issues with the positioning, an alteration was made to the reception transducer, adding a second linear coil to the EMAT as described in section 3.2.3. In this new approach, at each measurement position using the XY table the data from both coils is recorded, and these two measurements are used to calculate the phase velocity. This ensures that the distance between

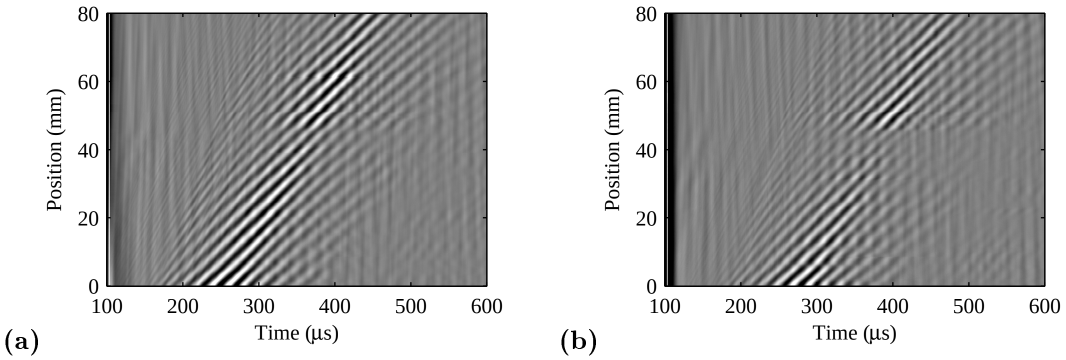

Figure 4.11: B-scans of the narrow-band signal on a nominally 100 μm thick aluminium sheet for (a) channel A, and (b) channel B for the two coil detection system. The arrival times of the waves for channel B occur after channel A, with a decrease in signal strength at channel B.

the measurement positions is accurately known, and dependent on the EMAT construction rather than the XY table, removing the positional inaccuracies as a source of error in the thickness measurements. A further improvement to the experimental procedure is the replacement of the ferrite-backed meander coil EMAT with a periodically polarised magnet (PPM) EMAT, the construction of which is discussed in 3.2.1. The use of a PPM EMAT simplifies the construction process and produces more consistent transducers, in addition to generating higher amplitude ultrasound. This was necessary to overcome a limitation in the sensitivity of the dual channel detection transducer, where the second channel has less sensitivity than the first channel. The generation mechanism used was the same as with the previous narrow-band measurements, where a multi-cycle tone burst was used to generate the narrow-band signal.

The data for this experiment was acquired in the same manner as in sections 4.2 and 4.3, where the generation transducer was maintained in a static position while the separation between the generation and reception transducers was gradually increased, although for each measurement position two time domain signals were captured by the dual channel reception transducer. The time domain signals from each channel were then used to create two separate B-scans, one for each channel, with an example shown in figure 4.11. The B-scans from the two channels are very similar, as would be expected, although there is a notable reduction in the signal amplitude between channels A and B. The decrease in signal strength between the two channels is due to the eddy currents generated by the ultrasound in the presence of a magnetic field reducing the energy of the ultrasonic wave [154]. As the dual channel EMAT consists of only one large magnet, the amount of energy lost by the ultrasound will be greater for channel B, as the ultrasound has further to travel in the presence of the magnetic field and thus loses more energy. This effect is similar to the magnetic braking produced by Lenz's law when dropping a magnet inside a copper

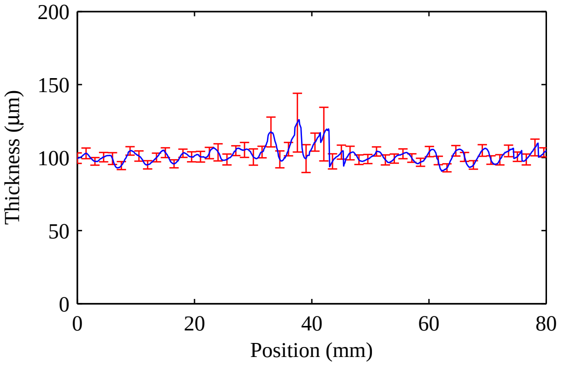

Figure 4.12: Thickness profile of a nominally 100 µm thick aluminium sheet using a dual channel reception EMAT with a narrow-band generation signal. The average thickness of the sheet along the scan is 101.9 ± 5.5 µm, which is in very good agreement with the nominal thickness of the sheet.

pipe [155].

As with the narrow-band B-scan shown in figure 4.9, the generation pulse lasts for roughly 100 µs, obscuring the incident S_0 wave, although edge reflections of this wave are visible throughout the dual channel B-scan. This necessitates that the velocity of the S_0 wave be calculated from a separate measurement. The A_0 wave velocity was also calculated in the same manner as the previous narrow-band results, where the phase difference was calculated using the CSD, which was used with equation 2.76 to compute the phase velocity. The uncertainty in the phase velocity was calculated using equation 4.4, and the thickness and uncertainty in the thickness were calculated using equations 4.1 and 4.5 respectively.

The measured thickness as a function of position is shown in figure 4.12, where the uncertainty is shown in red for one measurement out of every fifteen to provide a representative illustration of the uncertainty in the thickness measurement. By considering the thickness along the length of the scan the average thickness of the sheet is calculated as 101.9 ± 5.5 µm, where the uncertainty is derived from the standard deviation of the thickness along the scan. This is in good agreement with the nominal thickness of the sheet, confirmed by a micrometer measurement to be 100 ± 1 µm, although there are some deviations from the expected value at scan positions between roughly 30 to 40 mm. These correspond to areas of low signal strength in the B-scans in figure 4.11. There is also an increase in the uncertainty in this region, indicating that the thickness measurement is capable of identifying regions where the accuracy is diminished due to poor signal to noise, as would be expected from equation 4.4. Indeed, by considering the uncertainty of each measurement position and using a weighted mean and variance, the thickness of the sheet is calculated as 100.1 ± 3.9 µm, a significant improvement in accuracy over the unweighted mean.

4.5 Conclusions

In this chapter the limitations of the combined approximation used have been explored, and a methodology intended to minimise those limitations has been discussed. The range of validity of the phase velocity approximation has been shown to be three times greater than that of the group velocity approximation. Unlike previous work [55], this research has therefore focused on the phase velocity approximation. This methodology has then been implemented allowing thickness measurements to be performed on 100 µm thick sheets of aluminium using a combination of techniques. Using a broadband signal generator the thickness of the sheet was measured to be 99.9 ± 2.1 µm, while using a narrow-band generator the measured thickness was 95.0 ± 4.6 µm, demonstrating the potential of the measurement technique. In order to reduce the sensitivity of the measurement on errors in the distance between measurement positions on the XY table a dual coil reception transducer was constructed. Using this technique the thickness of the sheet was measured to be 100.1 ± 3.9 µm, a figure in excellent agreement with the nominal thickness of the sheet.

The approach has been tested on 100 µm thick aluminium sheets, which is a good initial measurement, and demonstrates the potential of the measurement technique. However, this potential must be extended to other materials and thicknesses to fully demonstrate the benefits of the technique in an industrial setting, and progress towards this goal is presented in the next chapter.

Chapter 5

Demonstration of the combined approximation on thicker samples

In this chapter the methods described in chapter 4 are expanded so that the thicknesses of a greater variety of samples can be measured, including aluminium samples with greater thicknesses than those described in chapter 4, and samples of other materials. This is done in order to expand the scope of the measurement technique, and to demonstrate that the positive results achieved for 100 µm thick aluminium are possible on other samples. The examinations of thicker aluminium samples will be influenced by the limitation to the validity of the approximation discussed in section 4.1, namely that in order to ensure that the approximation has an accuracy of greater than 99 % the frequency thickness must be less than 14.1 kHz. The limitations of the combined approximation when examining these samples is discussed, and a method for expanding the range of validity of the approximation is presented, showing that with only an limited knowledge of the material properties the range of validity of the approximation can be greatly extended.

5.1 Aluminium samples of different thicknesses

The measurements described in chapter 4 describe a test of the fundamental science on a single sample type, a 100 µm aluminium sheet. To be broadly useful as an industrial technique the measurements must also be demonstrated on a larger range of samples. In order to expand the utility of the measurement, tests were first performed on thicker aluminium samples to identify the limitations in the technique, and to develop a process for overcoming these. In addition, although the analysis of the phase velocity data is the same as in the algorithm presented in figure 4.3, the automation of the testing procedure has been increased in order to improve the industrial utility of the measurement, and reduce uncertainty introduced by a human operator. In the previous chapter the tests performed using a narrow-band generation signal required that the frequency of the signal be manually selected using the Ritec PR-4000, but in this series of tests the frequency was tuned automatically using a computer interface to control the Ritec signal generator. The software allows an initial start position in frequency to be defined, after which the computer will adjust the generation frequency in order to maximise the strength of the A_0 wave by ensuring the wavelength of the generated Lamb wave matches the periodicity of the generation transducer. The improvement of the automation of the measurement technique contributes to the utility of the technique in an industrial environment, by demonstrating that a standardised testing procedure can produce accurate thickness measurements on a range of samples. The scanning procedure for the dual channel transducer is the same as in section 4.4 when using the two coil detector, where the generation transducer is held in a constant position and the separation between the generation and detection transducers is increased from roughly 80 to 160 mm, and one measurement on each of the detection transducer's channels is performed at each measurement position. The reason for the change in the scanning range from the measurements presented in chapter 4 is twofold: firstly that the more efficient generation transducer allows a smaller number of cycles to be used, reducing the electrical cross-talk; and secondly that the number of spurious reflections increases with larger separations, making the data more difficult to analyse. The phase velocity is then calculated by comparing the phase of the two signals captured by the detection transducer at any given measurement position.

5.1.1 Aluminium sheet, 250 μm thick

The first sample tested using the improved methodology was a 250 μm thick sheet of aluminium. The B-scan for the sample recorded from channel A is shown in figure 5.1 (a), and the measured thickness as a function of position in figure 5.1 (b). The B-scan shows a high level of signal-to-noise in the raw data, indicating the benefits of the automated approach to tuning the generation signal, particularly with regards to reducing the coherent interference from the S_0 wave. This is due to the optimisation of the generation frequency for the A_0 wave, in this case to 30.1 kHz due to matching the wavelength of the Lamb wave in this sample to the periodicity of the EMAT, which decreases the effect of the S_0 wave reflections on the measurement, to the extent that they cannot be seen on the B-scan. As with the other narrow-band measurements the S_0 wave velocity was measured separately using the broadband technique discussed in section 4.2, as the non-dispersive nature of the wave means that the phase and group velocities are equivalent. The difference between

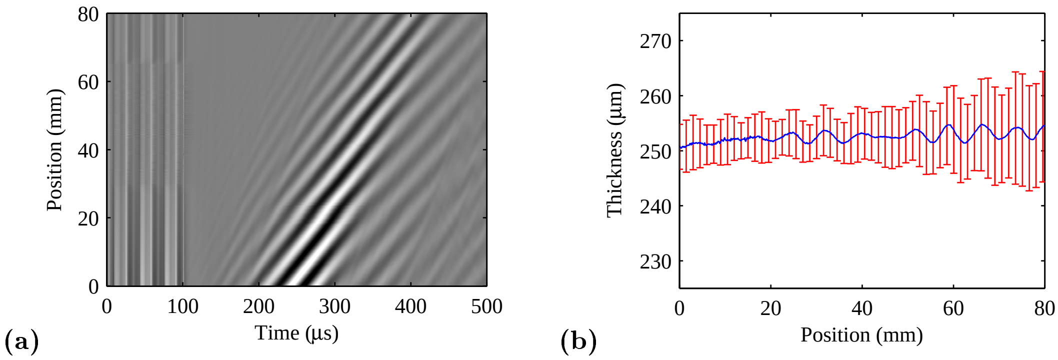

Figure 5.1: Results of thickness measurements performed on a 250 μm thick sheet of aluminium showing (a) a B-scan from the measurement and, (b) the thickness of the sheet as a function of the scan position. The average thickness measured across the sample is 252 ± 1 μm, when a weighted mean is used.

the velocity of the peaks within the wave and the energy of the wave packet for the A_0 wave can again be clearly seen in the B-scan, as can waves of a seemingly different velocity at a later time, corresponding to reflected A_0 waves from the edges of the sheet.

The thickness measurement performed gives a reliable estimate of the thickness of the sheet, where the weighted mean, previously used in section 4.4, across the sheet is 252 ± 1 μm, although the uncertainty in the individual measurements ranges from ± 5 μm to ± 10 μm, which seems larger than the perceived pattern in the measurement. As would be expected by the use of the signal to noise ratio to define the uncertainty, the points at the lower separations where the signal is strong have a lower error than the points at high separations, where the signal is visibly weaker in figure 5.1 (a).

It should be noted that although the physical separation of the coils in the dual channel transducer has not changed, the value used in equation 4.3 for the separation has changed from that used in the calculation for the 100 μm sheet (section 4.4). This change will be discussed in detail in section 5.1.3, as will possible sources for this disparity.

5.1.2 Aluminium sheet, 500 μm thick

A further test has been performed on aluminium sheets with a nominal thickness of 500 μm, and an example of these results are shown in figure 5.2. As with the previous measurement on 250 μm thick aluminium the frequency of the investigation was automatically tuned to optimise the received signal, although in this case the frequency selected was 45 kHz, where the wavelength of the Lamb wave matches the periodicity of the generation transducer. A further similarity between the B-scan in figure 5.2 (a) and that in figure 5.1 (a) is that the S_0 wave is not visible in the B-scan. This leaves only the A_0 wave, with little to no interference from the S_0 wave to distort its phase velocity

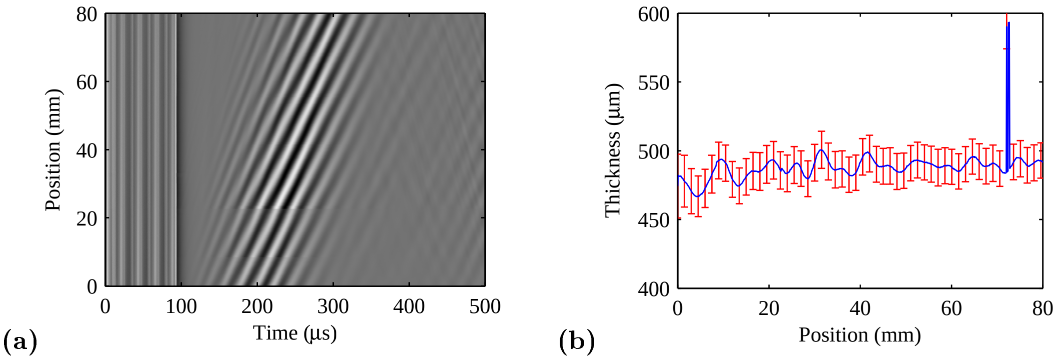

Figure 5.2: Results of thickness measurements performed on a 500 µm thick sheet of aluminium showing (a) a B-scan from the measurement and, (b) the thickness of the sheet as a function of the scan position.

measurements, which should improve the accuracy of the resulting thickness measurements, while the S_0 wave phase velocity was obtained using a broadband measurement of the group velocity, which due to the non-dispersive nature of the S_0 wave at this frequency thickness is equivalent to the phase velocity. The frequency of the generated Lamb wave in this sample is higher than that presented in section 5.1.1, which, combined with the greater thickness of the material, results in a higher velocity for the A_0 wave. This higher frequency and thickness directly affects the accuracy of the long wavelength approximation in these measurements, and the frequency thickness value of 22.5 kHz.mm exceeds the range of validity defined by the 1 % accuracy criterion. The systematic error from the use of the approximation will still be less than 2 %, which is still acceptable for these preliminary measurements. The greater speed of the A_0 wave means that some reflections of this wave from the edges of the sample can also be seen towards the end of the B-scan, although these fall outside of the time window where the direct A_0 wave is examined.

The thickness measurement of the sample can be seen in figure 5.2 (b), where the average measured thickness of the sample is 488 ± 9 µm, which is in good agreement with the nominal thickness of the sample. However, given that the frequency thickness of this sample exceeds the region where the the approximation can be considered accurate to 1 %, the agreement of the measured thickness with the thickness which would be measured by the approximation at this frequency thickness is more relevant, and the measured thickness is in excellent agreement with the thickness of 492 µm provided by the approximation. A feature of interest in this scan occurs at approximately 70 mm through the length of the scan, where an artefact of the data processing algorithm can be seen; a handful of data points that are noticeably larger than the points around them. This discrepancy is a result of the processing algorithm selecting the incorrect value of n in equation 4.3, which results in the sharp discontinuities in thickness seen in the figure.

Sample thickness (μm)	Change in separation (mm)
100 ± 1	+1.00
250 ± 2	-2.25
500 ± 5	+3.50

Table 5.1: Values of z, the change to the nominal transducer separation of 8 mm for each of the measurements using the dual coil detection transducer.

As with the previous measurement on the 250 μm sheet, the separation of the coils used in equation 4.3 to calculate the phase velocity was different from the physical separation of the coils, and this will be discussed in section 5.1.3.

5.1.3 Source of the static phase delay

As has been noted, each of the measurements using a dual coil transducer has used a slightly different value for the separation of the two measurement coils in equation 4.3, which has differed from the physical coil separation of 8 mm. The changes to this separation were made in order to tune the measured thickness of the technique to the nominal value, although the same value was used for each measurement, meaning that the measurements for each individual sample are self-consistent. This step is effectively performed as an empirical calibration to each sample. In this section the method of altering the measurements is discussed, as are some of the possible sources of the phase delay that requires this alteration.

For each of the phase velocity measurements using equation 4.3 (also defined previously as equation 4.3) the distance between the coils was altered, and the expression for the phase velocity is shown,

$$C_p\left(f\right) = \frac{2\pi f\left(x+z\right)}{\triangle\phi\left(f\right)+2\pi n}, \tag{5.1}$$

where the term z is the difference between the actual separation of the measurement coils and the separation value used. The values of the extra term z for each of the measurements using the dual coil detection transducer are shown in table 5.1.

A possible source of error is the presence of the magnetic field between the two measurement positions, as this would not cause an issue with the single channel measurements. In the single channel measurements discussed in sections 4.2 and 4.3 the distance that the propagating wave had to travel under the magnetic field was constant across all measurement positions, while in these dual channel measurements there is a significant difference in the distance the waves travel in the magnetic field between the coil at the front of the magnet and the second measurement coils. As has already been noted in section 4.4 the magnet has a significant damping effect on the amplitude of the ultrasound recorded by the second coil, relative to the first, and a phase effect is

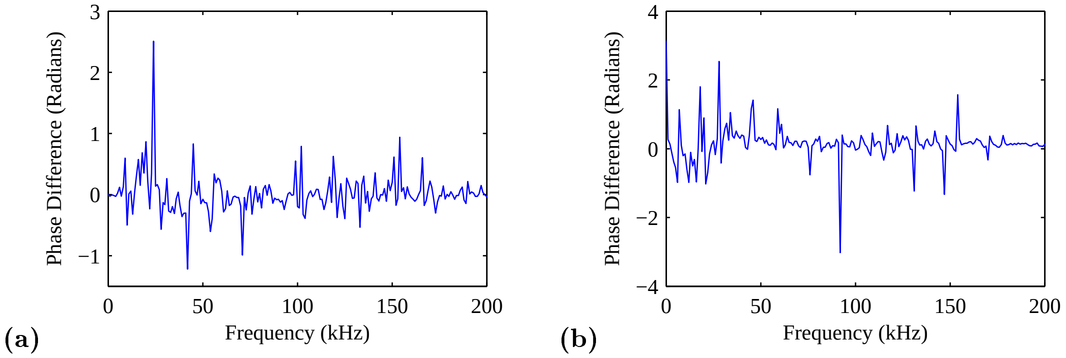

Figure 5.3: Phase difference between the recorded A-scans when (a) a magnet with a field parallel to the sample is introduced between the generation and detection transducers, and (b) when an EMAT is placed between the two transducers.

also possible. In order to examine this more closely an experiment was performed on the 500 μm thick aluminium sheet where the generation and detection transducers were positioned at close to their maximum spacing of 160 mm, and an A-scan was recorded with and without a magnetic field applied parallel to the sample between them. The phase spectrum of each measurement was then calculated and the difference between them is shown in figure 5.3 (a). As can be seen from this figure over the frequency range where the previous measurements have been made there is no perceptible change to the phase introduced by the magnet. That is to say, although the magnet has a pronounced effect on the amplitude of the signal recorded at the second coil, there is no evidence that there is any change to the phase of the signal due to the magnet.

A further test was performed using a similar methodology, where an EMAT connected to an oscilloscope was placed between the generation and detection transducers to determine if the measurement of the ultrasonic wave using the EMAT coil caused a significant change in the wave itself. The phase difference between the signals at the detection transducer, with and without the EMAT present, is shown in figure 5.3 (b), and as with the experiment using only the magnet, there is no discernible pattern to the change in the phase between the two phase spectra.

Another possible source of the static phase difference is in a difference in the lift-off of the two detection coils due to a change in the presentation of the transducer. If the transducer is held at an angle to the surface of the sample there will be a difference in the lift-offs of the two measurement coils that would not be present in a single coil measurement. It has been previously shown that the phase of a signal measured by an EMAT can be extremely sensitive to the lift-off of the reception transducer [79, 156], and as the detection EMAT was repositioned each time the measurement was performed this would adequately explain the change in the static phase delay between the measurements on different samples.

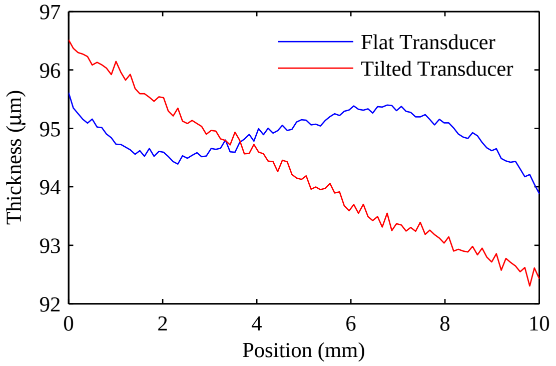

Figure 5.4: Difference in calculated thickness over the same area of a 100 μm thick aluminium sample due to a tilt in the transducer, such that the two measurement coils are at different lift-offs to the sample.

In order to perform a preliminary evaluation of this, an experiment was conducted on a 100 μm thick sheet of aluminium using the dual coil detection transducer, in the same manner as section 4.4, although the length of the scan performed was only 10 mm. This measurement was conducted using a frequency of 45 kHz, chosen in order to replicate the frequency of the measurement performed in section 5.1.2 and to rule out frequency as a significant factor. In this measurement two scans were performed over the same region of the sheet, although in the first scan the tilt of the transducer was minimised to keep the lift-off difference between the coils as small as possible, while in the second measurement the transducer was tilted, so that there was a difference in lift-off between the individual coils of approximately 0.5 mm. The two measured thickness profiles are shown in figure 5.4 Although the difference between the two measurements is small, the scan with the detection transducer parallel to the surface has an average thickness of 94.9 ± 0.4 μm across the length of the scan, while the tilted transducer has a an average thickness of 94.2 ± 1.1 μm over the same range, it is possible to see from figure 5.4 that there is a significant difference between the measurements, of up to 2 μm in some regions. As a preliminary measurement this shows that the presentation of the transducer to the sample will have a significant effect on the measured thickness, and this is an important area for further research. This also presents a significant challenge to implementation, as the vertical position of the sample must be very tightly controlled, likely requiring a special section in the rolling process where the measurement can be performed.

5.1.4 Single Channel Measurements

Although the thickness measurements conducted using a dual channel transducer are reliable, the unknown source of the static phase delay used in each case is of considerable concern when developing an industrially robust system where changes in the lift-off or tilt of the detection

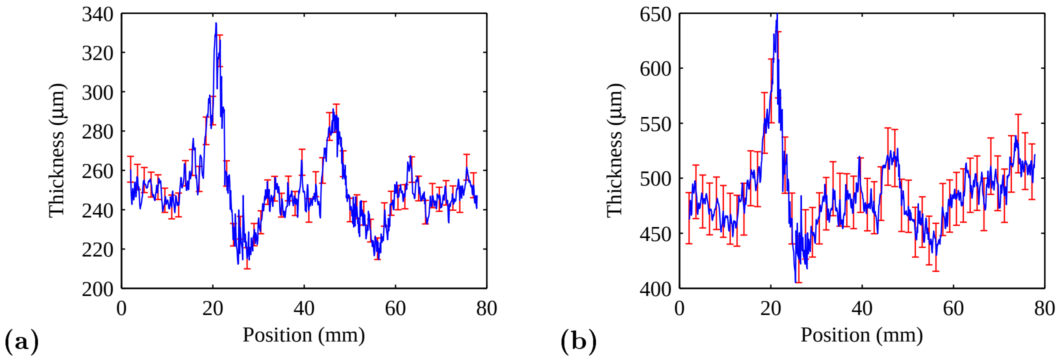

Figure 5.5: Results of thickness measurements performed on aluminium using a single channel detector for (a) a 250 µm thick sheet, and (b) a 500 µm thick sheet.

EMAT may occur. The value of this phase delay, although constant throughout each of the measurements, is chosen in order to coerce the measured thickness to the nominal thickness and hence the measurements are inherently biased. In order to take steps towards assuaging these concerns thickness measurements on these samples have also been performed using only the first channel of the transducer, effectively using the same measurement technique as that presented in section 4.3. An example of these measurements can be seen in figure 5.5 (a) and (b), for the 250 µm and 500 µm thick aluminium samples respectively. The measured thickness of the 250 µm sample is 247 ± 19 µm, while that of the 500 µm sample is 481 ± 31 µm. Although these uncertainties are large, the agreement between the measured values and the nominal values is again reasonable.

It can be seen from figure 5.5 that there is a considerable agreement in the pattern of measured thickness between the two samples, despite the fact that the two samples are completely independent. Due to this repeatability, the uncertainty in these measurements is chiefly due to the inaccuracy in the XY table, as the measurement scan across the two samples happened over the same range of motion of the table. This could explain the recurrence of the pattern in both measurements, as the thickness profile of the sheet is convoluted with the positional accuracy profile of the XY table. It should be noted that this positional inaccuracy has developed over time, and hence the single channel EMAT measurements on the 100 µm sheet (section 4.2), taken on the same XY table, but an earlier stage of the research, do not show this problem to the same level. Another possible source of this recurring pattern is that as the sheets are the same physical size it is possible that spurious reflections distort the data in the same manner. However, due to the difference in the frequency thickness of the waves between the two sheets, and thus the difference in the propagation velocity of the Lamb waves, this is unlikely.

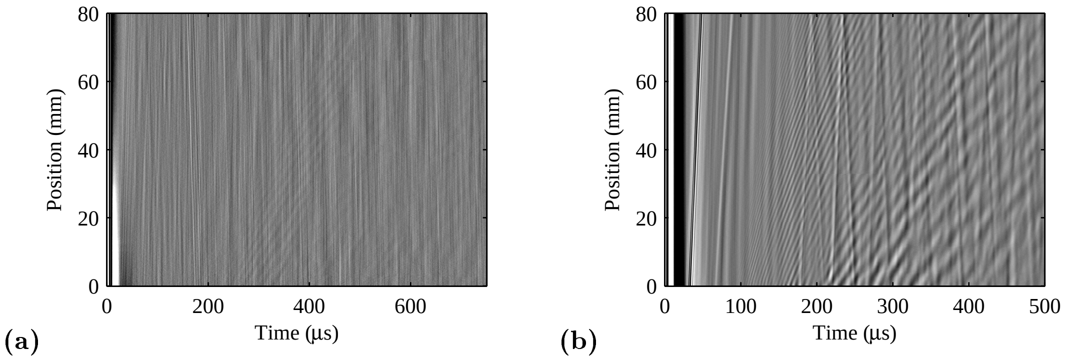

Figure 5.6: B-scans recorded on steel samples for (a) stainless steel and, (b) mild steel. The values on the grayscale axis for the stainless steel B-scan has been expanded a factor of 4 times compared to the mild steel sample.

5.2 Steel samples

In addition to the thicker aluminium samples, a set of steel samples were also tested using the dual channel detection EMAT in order to ascertain the performance of the measurement technique on materials other than aluminium. Both mild steel and stainless steel were tested, using a 200 µm thick mild steel sample, and a 100 µm thick austenitic stainless steel sample (type 316L). The stainless steel sample had the same dimensions as the previous aluminium sheets (300 x 300 mm), although the mild steel sample was of a significantly different size, 1000 x 150 mm. The efficiency of ultrasound generation in steel using EMATs is known to vary depending on the type of steel used [78, 157], and in this experiment the efficiency of generation in the mild steel was found to be considerably greater than in the stainless steel.

For both samples it was found that the signal-to-noise ratio of the A_0 wave was insufficient to perform the data analysis required to obtain a reliable measure of the thickness of the sample. This is due primarily to the lower efficiency of generation in steel using EMATs, when compared to aluminium, due to the lower conductivity. Examples of the B-scans for both the stainless steel and mild steel are shown in figure 5.6 (a) and (b) respectively, where in an attempt to increase the total signal an attempt was made to generate Lamb waves using a broadband source was made on the mild steel sample. This is due to the higher signal levels produced by the broadband generation electronics when compared to the narrow-band tone burst generator. In the stainless steel the A_0 wave can barely be discerned above the background, with the strongest portion of the wave occurring between 200 and 400 µs at the start of the scan, and 400 to 600 µs at the end of the scan. The S_0 wave is also extremely difficult to detect, although reflections of this wave from the edges of the sample can be seen. Taking a window in the time domain over the A_0 wave there are no clear peaks in the frequency domain, and the signal to noise ratio (SNR) is in the region of 1.2.

For the mild steel sample there appears to be sufficient energy in the A_0 wave to measure the thickness, as the SNR in the frequency domain is approximately 7.7, but the problem of multiple overlapping reflections of the S_0 wave greatly interferes with the A_0 wave. The effects of these reflections is exacerbated by the sample geometry in this case; whereas previous samples have uniformly been 300 x 300 mm square sheets, this sample was a longer, but thinner sheet, 1000 x 150 mm. The reduced width of the sample causes the S_0 wave reflections to recur throughout the measurement window, which disrupts the phase measurement of the A_0 wave to the extent where reliable thickness measurements are not possible.

Although this lack of signal-to-noise ratio makes these samples extremely difficult to analyse using the current equipment, it is extremely important to note that this represents a limitation in the experimental method of acquiring the data, not a limitation in the application of the long wavelength approximations to other materials. Using a more powerful generation EMAT, or more sensitive detection EMAT should increase the SNR, and could allow the measurements to be performed on these materials.

5.3 Improvements to the approximation

One of the key limitations to the method presented in chapter 4 is the finite range of validity of the approximation, as discussed in section 4.1. The upper limit of the range of validity for the approximation in an aluminium sample, assuming at most a 1 % systematic error due to the approximation, is 14.1 kHz.mm. Considering the lowest frequency used in this research, which is set by the Ritec signal generator at 30 kHz, this equates to a thickness limit of 0.47 mm. Thickness measurements using SH waves to perform calibrationless measurements have also been performed [62], with a working thickness range of 1.0 to 5.6 mm, although thickness measurements on thinner samples have been reported to have poor accuracy using this technique.

These two measurement techniques could be used in a complementary fashion in order to provide a method of measuring the thickness of a large range of samples without *a priori* knowledge of the sample, provided that the accuracy of the long wavelength Lamb wave approximation can be improved in the region from 0.5 to 1.5 mm. A forward solution has been developed, intended to improve the performance of the approximation using a limited knowledge of the material under test, and is described here.

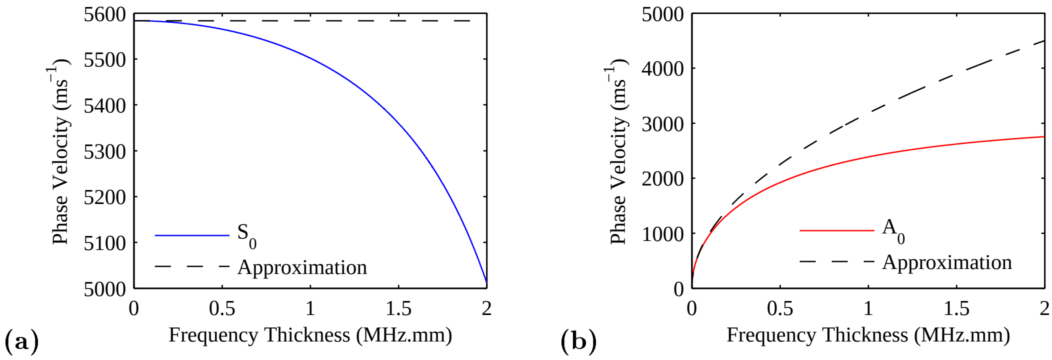

Figure 5.7: Comparison of the long wavelength approximations to the dispersion curves for an aluminium sample for (a) the S_0 wave, and (b) the A_0 wave, where the approximation value is shown by the dashed black line.

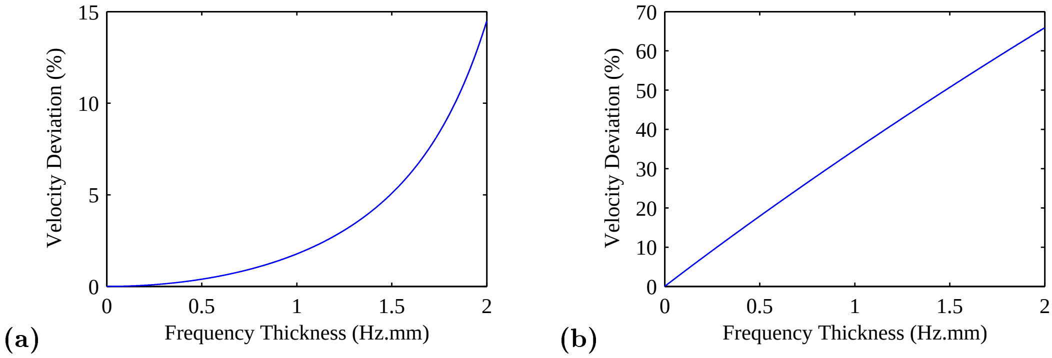

Figure 5.8: Deviation of the approximation phase velocity from the velocity predicted by the dispersion curves, as a percentage for (a) the S_0 wave, and (b) the A_0 wave.

5.3.1 Improvements using the dispersion curves

The long wavelength approximations described in equations 2.58 and 2.62 are only valid in the case where the wavelength of the Lamb wave greatly exceeds the thickness of the sample. The values of the wave velocities provided by these approximations deviate from the values provided by the dispersion curves as the frequency thickness increases, as shown in figure 5.7. In order to improve the performance of the approximation, the deviation from the values of phase velocity obtained from the dispersion curves by each of the approximations was explored.

The discrepancy between the numerical values from the dispersion curves and the approximation values is presented as a percentage of the numerical values of phase velocity as a function of the frequency thickness for an aluminium sample in figure 5.8. This shows that the discrepancy for both the S_0 and A_0 waves increases with increasing frequency thickness, although the S_0 wave approximation has a much lower deviation than that of the A_0 wave. A 5 % deviation occurs at a frequency thickness of 136 kHz.mm for the A_0 wave, while for the S_0 wave it occurs at 1.49 MHz.mm. By altering the long wavelength approximations in order to reduce the deviation

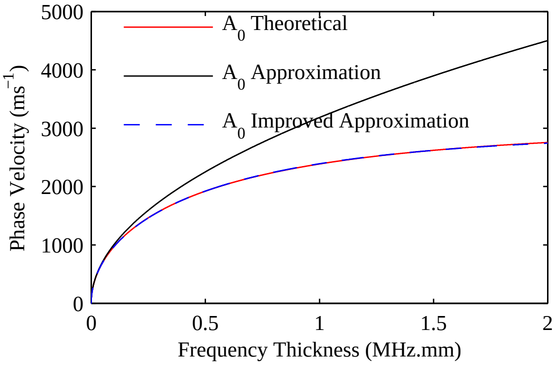

Figure 5.9: The phase velocity of the A$_0$ wave, from the long wavelength approximation and the improved approximation as compared to the values obtained from the dispersion curves.

between the approximate values and the real values the range of validity of the approximation for thickness measurements can be extended.

The deviations from the true velocity values can be modelled by approximating a power fit to the lines in figure 5.8, giving an empirical correction to the approximate values. Although this assumes knowledge of the material properties it provides a technique which is computationally more efficient than a method which calculates the dispersion curves using a forward model. The form of the power fit is

$$\frac{\sigma\left(C_p\right)}{C_p} = a\left(fd\right)^b, \tag{5.2}$$

where $\sigma\left(C_p\right)$ is the deviation in phase velocity, and the coefficients a and b describe the relationship between the deviation of the phase velocity and the frequency thickness product. For any given material the coefficients of this power law fit can be calculated for both the S$_0$ and A$_0$ waves by the calculation of the dispersion curves.

By integrating the empirical corrections into the long wavelength approximation, equation 2.65 can be rewritten as,

$$C_{Am}^2\left[\frac{\alpha\left(fd\right)^{\beta}}{100}+1\right]^2 = \frac{\pi fd}{\sqrt{3}}C_{Sm}\left[\frac{a\left(fd\right)^b}{100}+1\right] \tag{5.3}$$

where the subscript m denotes the measured phase velocity for the S$_0$ and A$_0$ waves, the coefficients α and β are the fit parameters for the A$_0$ wave, and a and b are the fit parameters for the S$_0$ wave. An example of the change in the long wavelength approximation for the A$_0$ wave is shown in figure 5.9 The marked improvement in the agreement with the dispersion curves between the long wavelength approximation and the improved approximation can be seen in the figure, with almost no perceptible deviation from the values obtained from the dispersion curves.

By considering an aluminium sample of thickness 1 mm, with longitudinal and transverse sound velocities of 6374 ms^{-1} and 3111 ms^{-1} respectively [151], the accuracy of the improved approximation

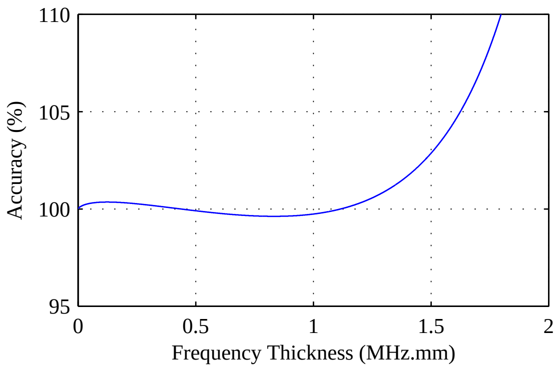

Figure 5.10: The accuracy of the improved phase approximation for aluminium as the frequency thickness product varies. The limit of the region of validity for the improved approximation is 1.32 MHz.mm.

can be calculated in the same way as the combined approximation was assessed in section 4.1. The assessment of the approximation is made by considering the thickness that would be measured at a given frequency thickness value, if the perfect values of the phase velocities obtained from the dispersion curves were measured. The fit to the S_0 wave deviation has been performed considering only the data up to values of 1 MHz.mm, as performing the fit over the entire frequency thickness range was found to compromise the performance of the improvement at lower values of frequency thickness, where this improvement to the technique is focused. For this material the performance of the improved approximation is shown in figure 5.10. The accuracy is evaluated in the same way as the combined approximation was evaluated in section 4.1, where a nominal accuracy of 1 % is selected, and the region of validity is described as that below the frequency thickness at which the improved approximation first deviates from the expected value of thickness by 1 %. For the improved approximation this is calculated to be 1.32 MHz.mm, which is roughly 90 times greater than the limit found for the phase velocity of the combined approximation. This improvement greatly exceeds the original aims of increasing the performance of the approximation to samples of 1.5 mm thickness, and considering the same 30 kHz signal previously discussed would result in an upper limit of the thickness of 44 mm. Beyond this region the improved approximation will overestimate the thickness of the sample rather than underestimate it, in contrast to the combined approximation. This change to the behaviour of the approximation beyond the region of validity could introduce problems, depending on the application of the thickness measurement. For example, in a safety critical application where the thickness of a sample is measured to evaluate its integrity overestimating the thickness could engender a false sense of safety regarding the component, however this could be mitigated by limiting the frequency thickness of the inspection to the region of validity for the approximation.

This significant improvement to the accuracy of the improved approximation comes at the cost of removing the ability to perform thickness measurements without *a priori* knowledge of the material properties. In order to correctly identify the empirical correction factors used in equation 5.3 the approximation must be compared to the dispersion curves, the calculation of which requires knowledge of the material properties. There are, however, significant advantages to the use of the improved approximation compared to other possible methods, such as look-up tables or calculation of the inverse problem. Employing look-up tables means essentially storing the dispersion curves, and comparing frequency and phase velocity of various wavemodes to the stored values would be an extremely memory intensive task. The entire calculated dispersion curve would have to be stored, requiring considerably more physical memory, and possibly precluding the use of embedded systems in the development of any prototype system. Solving the inverse problem poses a similar limitation to the processing power of whatever computer hardware is used to calculate the thickness of the sample, due to the computationally intensive nature of the method [54]. Compared to these two options, the improved approximation occupies a "Goldilocks" zone, as it requires little in the way of processing power or memory, and stores only the four coefficients of the empirical correction.

5.3.2 Dependence of the improved approximation on material properties

The extension to the region of validity in section 5.3.1 assumes that the material properties are well known, which undermines one of the key advantages of the original approach using the combined approximation. However, the effect that approximate knowledge of the material properties will have on the accuracy of the measurements using the improved approximation can be considered, identifying whether choosing from an intentionally poor set of coefficients of the improved approximation has a significant effect on the range of frequency thickness values over which the approximation can be used. The variation in the materials properties of a sample from a chosen ideal material can be due to a number of factors, such as temperature, alloy composition or stress, although the variation in material properties tends not to be extreme; for an increase in temperature of 88 ^{o}C there is a change in the Young's modulus of an aluminium wire of only 5.5 % [106]. Although the Young's modulus of Aluminium is typically given as 70.3 GPa [151], in alloys with high concentrations this is reported to range from 78 to 83 GPa [158].

This dependence of the performance of the improved approximation on perfect knowledge of the materials properties has been examined by calculating values for the fit parameters a, b, α and β for given values of the material properties, and re-evaluating the the range of validity of the approximation, as shown in 5.10, for a range of material properties around this point. This allows figure 5.10 to be drawn for a large range of materials properties, all while assuming only one set of

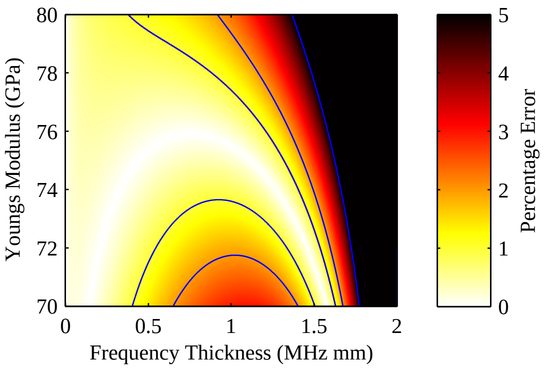

Figure 5.11: The accuracy of the improved approximation as a function of both the frequency thickness and the material properties for fit parameters calculated at 75 GPa. The limit of the region of validity at its lowest value of frequency thickness is 379 kHz.mm at 80 GPa, which corresponds to a variation in the material properties of 6.7 %.

values for the coefficients of the improved approximation. An example of this analysis is shown in figure 5.11, where fit parameters were calculated for a median value of Young's modulus of 75 GPa, while the range of validity was then calculated for a range of values of Young's modulus between 70 and 80 GPa. These individual graphs are combined to form a colour plot, where the colour scale indicates the deviation of the approximation from the nominal value of the thickness as both the frequency thickness and the Young's modulus vary. For a variation in the Young's modulus of 6.7 % the improved approximation remains valid up to a limit of 379 kHz.mm, which is a factor of 25 times higher than the unaltered, combined approximation. However, in this measurement only the variation of a single material property was considered in isolation.

In order to more broadly examine the performance of the improved approximation the effect of varying more than one material property, such as the density or the Poisson's ratio, simultaneously must be considered. This can be simplified by considering instead the longitudinal and transverse wave velocities, as these will both vary as the materials properties change. Additionally, this simplifies the analysis, as only the longitudinal and transverse wave velocities are needed to calculate the dispersion curves of the Lamb waves (equation 2.46). The chosen wave velocities for aluminium, 6374 ms^{-1} and 3111 ms^{-1} for the longitudinal and transverse waves, as given in [151], were considered when calculating the empirical correction to the improved approximation. These values were then varied by ± 10 %, which covers a large range of materials, such as iron, magnesium, molybdenum, steel and titanium [151], and the upper limit, given at the point where the percentage error of the improved approximation exceeds 1 %, of the region of validity for the improved approximation was then calculated. The frequency thickness of this limit is shown by the colour-bar in figure 5.12 as a function of longitudinal and transverse velocity. The figure shows that the approximation is much more sensitive to changes in the transverse velocity than it is to changes

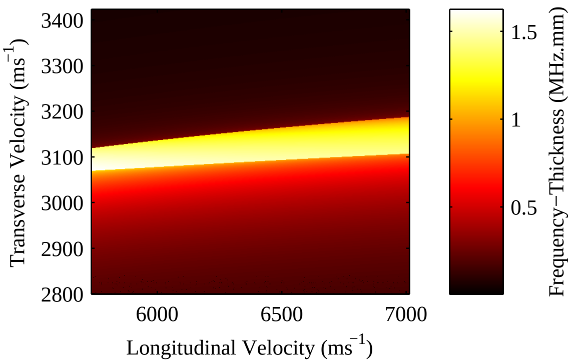

Figure 5.12: The upper limit to the region of validity of the improved approximation as a function of both longitudinal and transverse velocity.

in the longitudinal velocity, although for changes of ± 1 % in the material properties from the chosen values used to calculate the coefficients for the improved approximation, the upper limit of the region of validity is over 800 kHz.mm which corresponds to a thickness limit of 26.7 mm if a 30 kHz signal is used. The extent of the material properties shown in the figure also encompasses mild steel, with longitudinal and transverse wave speeds of 5960 ms^{-1} and 3225 ms^{-1}respectively [151], and at these values the upper limit of the region of validity when using the wave velocities of aluminium to calculate the improved approximation is 104 kHz.mm. This means that even in the case of mistaking a mild steel sample for an aluminium one, the approximation will have an upper thickness limit for accurate measurement (less than 1 % error) of 3.47 mm, when considering a 30 kHz wave, which is considerably above the target thickness limit of 1.5 mm.

Even with only a rudimentary knowledge of the material properties it is possible to considerably improve the performance of this approximation in order to allow this measurement technique to be used to complement the technique previously presented using SH wave dispersion [62]. This allows thickness measurements to be made on a large range of sample thicknesses with only a weak sensitivity to the materials properties, or in fact, no sensitivity at all, with this technique operating for thicknesses of up to 1.5 mm, and the SH based technique used for higher thicknesses.

5.4 Conclusions

The analysis of the thicker aluminium samples is highly encouraging, and shows that, although the absolute performance of the measurement is limited by the validity of the approximation discussed in section 4.1, the performance across each individual sample is highly consistent. A measurement technique has been demonstrated which almost completely eliminates the variation in the thickness measurements due to the reflections of the S_0 wave disrupting the phase of the

A_0 wave, by generating the A_0 wave almost exclusively. Although the measurements have so far been unsuccessful on steel samples this is due to a limitation in the efficiency of generating and detecting ultrasound in these samples using EMATs [68], and not a shortcoming of the technique of measuring thickness in this manner. Additionally, there has been some excellent progress on improving the range of validity for the approximation, and this has been shown to be improved by a factor of seven, even in cases where the values of the empirical correction calculated for aluminium are used for measuring a mild steel sample. Using the approved approximation the measurement should perform well on aluminium samples with thicknesses in excess of 1.5 mm, allowing the technique to be used as a complement to a similar technique using SH waves [62].

Chapter 6

Thickness measurements using Lamb Waves: Conclusions

This chapter presents a summary of the research using the dispersion of Lamb waves to determine the thickness of metal sheets, and the progress made from developing the technique from TRL1 to TRL3, where the proof of concept of the measurement has been demonstrated in the laboratory. The novel EMATs developed are discussed, as are results of thickness measurements on a variety of metal samples. The steps required for further work to develop the method into a more robust technique suitable for industrial application are discussed, as is an analytical approach which could be used to improve the validity of the long wavelength approximation, as an alternative to the empirical approach presented in section 5.3.

6.1 EMAT Design

During the course of this research several topics of note have arisen in the design of the EMATs developed. The effect of the interaction between the relatively large skin depth of the electromagnetic signal compared to the thickness of the thin samples has been shown to preferentially generate the A_0 wavemode (section 2.3.1.2), while the requirement for an EMAT capable of efficiently generating out-of-plane displacements has led to the development of a novel PPM EMAT (section 3.2.1). The technique of using a periodic magnet array to construct periodic EMATs simplifies the coil winding significantly, as a simple racetrack coil can be used in place of a complex meander coil. The use of a PPM array also increases the homogeneity of the EMATs, as it avoids the issues of magnetic field variation in proximity to a single large magnet, and the simplicity of construction of the PPM array allows homogeneous EMATs to be made easily.

These EMATs allow for the preferential generation of Lamb waves with out-of-plane displacements, and offer another tool for mode selectivity besides the typical method of using the frequency and wavelength of the transducer. Additionally, the PPM generates an out-of-plane displacement which would be suitable for the generation of longitudinal waves on bulk samples, while the array nature of the waves has applications for frequency controlled beam steering [159].

6.2 Lamb wave thickness measurements

The effectiveness of the combined approximation, the approximation resulting from the combination of the long wavelength approximations for phase velocity formulated by Lamb [107], as applied to thickness measurements has been demonstrated on a range of aluminium samples, with relatively high accuracy and excellent precision (chapter 4 and section 5.1). The combined approximation has been shown to allow thickness measurements without need for any calibration to have an accuracy of 1 % at sample frequency thickness products of up to 14.1 kHz.mm (section 4.1). The initial broadband measurements have proven to be extremely accurate, and, although similar measurements performed with a narrow-band source were shown to be less accurate, it is thought that this is due to a degradation in the positional accuracy of the XY table rather than an issue with using narrow-band signals. For the broadband signal the measurement on a nominally 100 μm thick sheet gives a thickness of 99.9 ± 2.1 μm, while using a narrow-band signal it is measured as 95.0 ± 4.6 μm.

The attempts to avoid the issue of positional accuracy of the XY table by utilising a dual coil measurement system in order to fix the distance between measurement positions have proven to be a moderate success. However, a phase delay of unknown origin was observed, leading to this being considered during the data processing in order to ensure that the performance of the measurement is accurate. In spite of this, the repeatability of the measurement across each sample is high, leading to the conclusion that, although further work is needed, this method provides a useful technique to perform thickness measurements on thin samples without the need for calibration of the sound velocities of the sample, or indeed any knowledge of the material being examined. For a 100 μm thick sheet the measured thickness was found to be 100 ± 4 μm, while for 250 μm and 500 μm sheets the thickness was found to be 247 ± 1 μm and 488 ± 9 μm respectively.

Another development is that of the empirical correction to the approximation, which greatly increases the range of validity, allowing much thicker samples to be measured (section 5.3). This improved approximation has been shown to allow the technique to be used on samples where the transverse and longitudinal velocities are known to an accuracy of ± 1 % up to a frequency thicknesses in excess of 800 kHz.mm. This is 50 times greater than the original approximation, while still retaining an accuracy of greater than 99 %. Even with a very rudimentary knowledge of the material properties, such as assuming a mild steel sample is aluminium for the purposes of calculating the empirical correction, the range of validity of the approximation shows a large improvement over the combined approximation, in this case giving results with high accuracy at frequency thickness values of up to 104 kHz.mm.

6.3 Further work

This research has identified several areas worthy of further investigation. The first area concerns the formulation of an analytical model for improving the combined approximation, to act as a addendum to the empirical approach already presented (section 5.3). The second area in which further work would be useful is identification of the unknown phase delay introduced when using two measurement coils on the same magnet (section 5.1.3). Finally the requirements for producing a viable system for industrial application such as increasing the robustness of the sensors, are discussed.

6.3.1 Analytical improvement to the approximation

The combined approximation used in the majority of this work has a limitation in its validity; as discussed in section 4.1 the approximation can only be considered accurate to 1 % when the frequency thickness of the sample investigated is less than 14.1 kHz.mm. Although an improvement intended to overcome this limitation was presented in section 5.3, which used an empirical correction to coerce the phase values calculated by the long wavelength approximations to the correct values, an analytical solution is also desirable. By examining the assumptions that led Lamb to the formation of the approximations for the phase velocities of the fundamental wavemodes at low frequency thickness [107], it may be possible to improve the approximation by using an analytic method. The approximations for the phase velocities are obtained by considering only the first order terms of the Taylor expansion of $\tan(\theta)$ in the case of the symmetric wave, and the first and third order terms in the case of the antisymmetric wave, presented in equations 2.54 and 2.59 respectively. By considering the higher order terms of these approximations it should be possible to arrive at a more accurate approximation for the symmetric and antisymmetric phase velocities, with potential improvements to measurements of the thickness of the plate. An investigation of these equations is beyond the scope of this research, however, and unfortunately there is no guarantee that this will achieve an elegant solution relating the phase velocities to the sheet thickness, as shown in equation 2.63. Depending on the complexity of the eventual solution this may be computationally much more intensive than the empirical correction, although it should still remain significantly simpler than methods using the full solution of the dispersion curves.

Although the full solution of the approximations using the higher order terms is beyond the scope of this research, the initial equations to be solved are presented here. The equation for the symmetric wave, considering the first and third order terms is,

$$\frac{qh\left(1+\frac{1}{3}q^2h^2\right)}{ph\left(1+\frac{1}{3}p^2h^2\right)} \approx -\frac{4k^2pq}{\left(k^2-q^2\right)^2}, \tag{6.1}$$

while the equation for the antisymmetric wave, considering terms up to and including the fifth order terms of the Taylor expansion is,

$$\frac{qh\left(1+\frac{1}{3}q^2h^2+\frac{1}{5}q^4h^4\right)}{ph\left(1+\frac{1}{3}p^2h^2+\frac{1}{5}p^4h^4\right)} \approx -\frac{\left(k^2-q^2\right)^2}{4k^2pq}. \tag{6.2}$$

These equations are similar to equations 2.54 and 2.59, and are effectively just a more accurate representation of those equations. Although they cannot be easily manipulated to arrive at a simple relationship between the sample thickness and the A_0 velocity and the S_0 velocity, due to the increased complexity of the equations, it may be possible that by expanding these equations, and attempting to relate them to each other, a relationship between the phase velocities and the sample thickness can be established.

6.3.2 Source of the phase delay in multi-coil measurements

As mentioned in section 5.1 the use of a two coil measurement transducer introduces an unknown phase delay that, while remaining constant for a given sample, varies from sample to sample. The nature and origin of this phase delay must be explored in order to properly develop this research into a practical measurement technique, and although several possible sources of the delay have been excluded, including the presence of a large magnet inducing a change in the phase due to magnetic braking, the source is still in question.

Although the measurement apparatus remained unchanged when the samples were changed there are other effects which could be considered. The lift-off of the coils, if uneven, could present a measurable phase delay, which could account for the change in delay observed between samples [156]. Attempting to use a plastic spacer on which the EMAT rests in order to create a consistent lift-off unfortunately damps the out-of-plane components of the A_0 wave, severely hampering the measurement. A preliminary measurement to test this theory has been made, and has shown that the tilt of the transducer can introduce significant variations in the measured thickness (section 5.1.3). In order to develop the relationship between the tilt and the measured changes in the thickness the presentation of the detection transducer to the sample would have to be thoroughly examined. If this relationship could be quantified, and the static phase delay could be calculated mathematically with a physical basis, greatly improving the utility of the results in section 5.1.

6.3.3 Implementation of an industrial system

Despite the uncertainty over the quantified effects of the tilt of the detection transducer on the thickness measurements the measurement technique is very close to industrial viability. The advantage of only needing access to a single side of the sample, not to mention the lack of reliance on radiographic methods [10], makes the measurement technique attractive for the on-line measurement of thickness of cold rolled aluminium foils. For on-line measurements the aluminium foil would move past a stationary transducer arrangement, making the dual coil technique of measuring the thickness significantly more suitable. Provided that the distance between the aluminium sheet and the detection coils can be maintained then the consistent nature of the measurements should allow the measurements to be performed. Measuring the S_0 wave velocity with an independent measurement may require some level of positional encoding of the sheet being measured to ensure that the velocity of both waves in the same regions are being compared. Further work may also have to be performed in optimising the transducer separation, to ensure that the signal levels are maximised, while minimising the effect of spurious reflections on the thickness measurement.

However, although the measurement technique is promising, a number of problems may arise. Due to the highly sensitive nature of the phase velocity measurements these may be more susceptible to electrical noise, which may be problematic in an industrial environment. Another potential concern is the length of time over which the measurements are acquired, as the work presented in this thesis is typically performed while averaging 512 times, rather than the single shot measurements likely to be required of an on-line measurement system. Additionally, it may be necessary to perform some form of correction to disentangle the wave motion from the motion of the sheet, possibly by performing the phase velocity measurement both in the direction of travel of the sheet, as well as in opposition to its motion. Furthermore, any change in the lift-off between the sheet and the detection transducer could have severe effects on the reliability of the measurement, so steps would have to be taken to minimise this.

A number of concerns over the durability of the EMAT sensors themselves must also be assuaged in any industrial implementation. The ability to reduce the amount of metallic swarf collected by the magnets, or at least to periodically remove it, must be considered, as must the physical hardening of the transducers themselves, potentially using a ceramic wear surface. Additionally, the transducers must be able to be rapidly removed from proximity to the sample in the event of a buckle in the line. In order to satisfy the requirement to minimise any change in the lift-off between the transducer and the sample, the vertical position of the sensor may have to be actuated with a fast responding and highly accurate system.

Chapter 7

Measurement of lift-off using eddy current techniques: Experimental Details

Due to the terms of the research contract the details presented in chapters 7-10 are to be treated as confidential.

[redacted]

[redacted]

[redacted]

[redacted]

[redacted]

- [redacted]
- [redacted]
- [redacted]
- [redacted]
- [redacted]
- [redacted]
- [redacted]
- [redacted]
- [redacted]

[redacted]

[redacted]

[redacted]

[redacted]

[redacted]

[redacted]

[redacted]

[redacted]

$$[redacted] \quad [redacted]$$

[redacted]

[redacted]

[redacted]

[redacted]

[redacted]

[redacted]

[redacted]

[redacted]

[redacted]

[redacted]

[redacted]

[redacted]

[redacted]

[redacted]

[redacted]

[redacted]

[redacted]

[redacted]

[redacted]

[redacted]

[redacted]

[redacted]

[redacted]

[redacted]

[redacted]

[redacted]

[redacted]

[redacted]

[redacted]

[redacted]

[redacted]

[redacted]

[redacted]

[redacted]

[redacted]

[redacted]

[redacted]

[redacted]

[redacted]

[redacted]

[redacted]

[redacted]

[redacted]

[redacted]

[redacted]

[redacted]

[redacted]

[redacted]

[redacted]

[redacted]

[redacted]

[redacted]

[redacted]

[redacted]

[redacted]

[redacted]

$$[redacted] \qquad [redacted]$$

[redacted]

$$[redacted] \qquad [redacted]$$

[redacted]

[redacted]

[redacted]

[redacted]

[redacted]

[redacted]

[redacted]

[redacted]

[redacted]

[redacted]

[redacted]

[redacted]

[redacted]

[redacted]

[redacted]

[redacted]

[redacted]

[redacted] [redacted]

[redacted]

[redacted]

[redacted]

[redacted]

Chapter 8

Profile measurements using the single frequency method

[redacted]

[redacted]

[redacted]

[redacted]

[redacted]

[redacted]

[redacted]

[redacted]

[redacted]

[redacted]

[redacted]

[redacted]

[redacted]

[redacted]

[redacted]

[redacted]

[redacted]

[redacted]

[redacted]

[redacted]

[redacted]

[redacted]

[redacted]

[redacted]

[redacted]

[redacted]

[redacted]

[redacted]

[redacted]

[redacted]

[redacted]

[redacted]

[redacted]

[redacted]

[redacted]

[redacted]

[redacted]

[redacted]

[redacted]

[redacted]

[redacted]

[redacted]

[redacted]

[redacted]

[redacted]

Chapter 9

Profile measurements using the resonance method

[redacted]

[redacted]

[redacted]

[redacted]

[redacted]

[redacted]

[redacted]

[redacted]

[redacted]

[redacted]

[redacted]

[redacted]

[redacted]

[redacted]

[redacted]

[redacted]

[redacted]

[redacted]

[redacted]

[redacted]

[redacted]

[redacted]

[redacted]

[redacted]

[redacted]

[redacted]

[redacted]

[redacted]

[redacted]

[redacted]

[redacted]

[redacted]

[redacted]

[redacted]

[redacted]

[redacted]

[redacted]

[redacted]

[redacted]

[redacted]

[redacted]

[redacted]

[redacted]

[redacted]

[redacted]

[redacted]

[redacted]

[redacted]

[redacted]

[redacted]

[redacted]

[redacted]

[redacted]

[redacted]

[redacted]

[redacted]

[redacted]

[redacted]

[redacted]

[redacted]

[redacted]

[redacted]

[redacted]

[redacted]

[redacted]

[redacted]

[redacted]

[redacted]

[redacted]

[redacted]

[redacted]

[redacted]

Chapter 10

Profile measurements using eddy currents: Conclusions

[redacted]

[redacted]

[redacted]

[redacted]

[redacted]

[redacted]

[redacted]

[redacted]

[redacted]

[redacted]

[redacted]

[redacted]

[redacted]

[redacted]

[redacted]

[redacted]

[redacted]

[redacted]

[redacted]

References

[1] L. Cartz, *Nondestructive testing : radiography, ultrasonics, liquid penetrant, magnetic particle, eddy current.* ASM International, 1995.

[2] J. Blitz and G. Simpson, *Ultrasonic methods of non-destructive testing.* Chapman & Hall, 1996.

[3] X. P. Maldague, *Theory and Practice of Infrared Technology for Nondestructive Testing.* J. Wiley, 2001.

[4] J. Cantrell and W. Yost, "Acoustic harmonic generation from fatigue-induced dislocation dipoles," *Philosophical Magazine A*, vol. 69, no. 2, pp. 315–326, 1994.

[5] A. Scarr, *Metrology and precision engineering*, ser. European mechanical engineering series. McGraw-Hill, 1967.

[6] K. A. Fowler, G. M. Elfbaum, K. A. Smith, and T. J. Nelligan, "Theory and application of precision ultrasonic thickness gauging," *Insight*, vol. 38, no. 8, pp. 582–587, 1996.

[7] W. J. Walecki, F. Szondy, and M. M. Hilali, "Fast in-line surface topography metrology enabling stress calculation for solar cell manufacturing for throughput in excess of 2000 wafers per hour," *Measurement Science and Technology*, vol. 19, no. 2, p. 025302, 2008.

[8] X. Jian, I. Baillie, and S. Dixon, "Steel billet inspection using laser-EMAT system," *Journal of Physics D-Applied Physics*, vol. 40, no. 5, pp. 1501–1506, 2007.

[9] C. Edwards, S. Dixon, A. Widdowson, and S. B. Palmer, "Electromagnetic acoustic transducers for wall thickness applications in the petrochemical industry," in *Review of Progress in Quantitative Nondestructive Evaluation, Vols 19a and 19b*, ser. AIP Conference Proceedings. Amer Inst Physics, 2000, pp. 1793–1800.

[10] G. Robertson, *Food Packaging: Principles and Practice, Second Edition*, ser. Food science and technology. Taylor & Francis, 2005.

[11] M. Potter and S. Dixon, "Apparent texture symmetry deviations in aluminum sheet," *Ultrasonics, Ferroelectrics, and Frequency Control, IEEE Transactions on*, vol. 52, no. 10, pp. 1791–1796, Oct 2005.

[12] "The Ionising Radiations Regulations," Statutory Instruments No.3232, 1999.

[13] Danieli, "HiTHIX/40 X-Ray Thickness Gauge," Danieli, 2015.04.11.

[14] J. Blitz, *Electrical and Magnetic Methods of Non-Destructive Testing.* Chapman & Hall, 1997.

[15] R. Hughes and S. Dixon, "Eddy-current crack detection at frequencies approaching electrical resonance," in *American Institute of Physics Conference Series*, ser. American Institute of Physics Conference Series, vol. 1581, Feb. 2014, pp. 1366–1373.

[16] A. C. Park, D.G. and Y. Cheong, "Differential pulsed eddy current probe to detect the sub surface cracks in a stainless steel pipe," in *18th World Conference on Nondestructive Testing*, 2012.

[17] X. Ma, A. Peyton, and Y. Zhao, "Eddy current measurements of electrical conductivity and magnetic permeability of porous metals," *NDT & E International*, vol. 39, no. 7, pp. 562 – 568, 2006.

[18] J. Moulder, E. Uzal, and J. Rose, "Thickness and conductivity of metallic layers from eddy-current measurements," *Review of Scientific Instruments*, vol. 63, no. 6, pp. 3455–3465, 1992.

[19] E. Jordan, *Electromagnetic waves and radiating systems.* Prentice-Hall, 1950.

[20] W. Yin, A. Peyton, and S. Dickinson, "Simultaneous measurement of distance and thickness of a thin metal plate with an electromagnetic sensor using a simplified model," *Instrumentation and Measurement, IEEE Transactions on*, vol. 53, no. 4, pp. 1335–1338, 2004.

[21] DeFelsko, "N90S Eddy Current Thickness Gauge," DeFelsko, 2015.04.11.

[22] R. Halmshaw, *Industrial Radiology: Theory and Practice.* Chapman & Hall, 1995.

[23] R. Loveman, J. Bendahan, T. Gozani, and J. Stevenson, "Time of flight fast neutron radiography," *Nuclear Instruments and Methods in Physics Research Section B: Beam Interactions with Materials and Atoms*, vol. 99, pp. 765 – 768, 1995.

[24] O. Büyüköztürk, "Imaging of concrete structures," *NDT & E International*, vol. 31, no. 4, pp. 233 – 243, 1998.

[25] J. Ambrose and G. Houndfield, "Computerized transverse axial tomography," *British Journal of Radiology*, vol. 46, no. 542, pp. 148–149, 1973.

[26] K. Marstboom, "Computed radiography for corrosion and wall thickness measurements," *Insight*, vol. 41, no. 5, pp. 308–309, 1999.

[27] J. Cutnell and K. Johnson, *Physics*, ser. Physics. Wiley, 1994, no. v. 2.

[28] F. Maier and B. G. Zagar, "Measurement of paint coating thickness by thermal transient method," *Ieee Transactions on Instrumentation and Measurement*, vol. 58, no. 6, pp. 1958–1966, 2009.

[29] S. Marinetti and V. Vavilov, "IR thermographic detection and characterization of hidden corrosion in metals: General analysis," *Corrosion Science*, vol. 52, no. 3, pp. 865 – 872, 2010.

[30] M. Silk and B. Lidington, "The potential of scattered or diffracted ultrasound in the determination of crack depth," *Non-Destructive Testing*, vol. 8, no. 3, pp. 146 – 151, 1975.

[31] T. Bloodworth, "High-accuracy defect sizing for nozzle attachment welds using asymmetric TOFD," *Insight*, vol. 41, no. 9, pp. 589–591, 1999.

[32] T. Stratoudaki, R. Ellwood, S. Sharples, M. Clark, M. G. Somekh, and I. J. Collison, "Measurement of material nonlinearity using surface acoustic wave parametric interaction and laser ultrasonics," *The Journal of the Acoustical Society of America*, vol. 129, no. 4, pp. 1721–1728, 2011.

[33] S. Song, H. Shin, and Y. Jang, "Development of an ultrasonic phased array system for nondestructive tests of nuclear power plant components," *Nuclear Engineering and Design*, vol. 214, no. 1-2, pp. 151–161, May 2002, 3rd International Workshop on the Integrity of Nuclear Components, Inst. Nucl. Energy Res., Taiwan, Oct 11-12, 2000.

[34] BSI, "Specification for acceptance levels for internal imperfections in steel plate, strip and wide flats, based on ultrasonic testing," British Standards Institution, BS 5996:1993, 1993.

[35] R. K. Oruganti, R. Sivaramanivas, T. N. Karthik, V. Kommareddy, B. Ramadurai, B. Ganesan, E. J. Nieters, M. F. Gigliotti, M. E. Keller, and M. T. Shyamsunder, "Quantification of fatigue damage accumulation using non-linear ultrasound measurements," *International Journal of Fatigue*, vol. 29, no. 9-11, pp. 2032–2039, 2007.

[36] R. Benz, M. Niethammer, S. Hurlebaus, and L. J. Jacobs, "Localization of notches with Lamb waves," *The Journal of the Acoustical Society of America*, vol. 114, no. 2, pp. 677–685, 2003.

[37] P. W. Loveday, "Modeling and measurement of piezoelectric ultrasonic transducers for transmitting guided waves in rails," in *2008 IEEE Ultrasonics Symposium, Vols 1-4 and Appendix*, ser. Ultrasonics Symposium. IEEE, 2008, pp. 410–413.

[38] J. L. Rose, *Ultrasonic waves in solid media.* Cambridge University Press, 1999.

[39] D. N. Alleyne and P. Cawley, "Optimization of Lamb wave inspection techniques," *NDT & E International*, vol. 25, no. 1, pp. 11–22, 1992.

[40] D. Alleyne and P. Cawley, "A two-dimensional Fourier transform method for the measurement of propagating multimode signals," *The Journal of the Acoustical Society of America*, vol. 89, no. 3, pp. 1159–1168, 1991.

[41] D. N. Alleyne and P. Cawley, "The excitation of Lamb waves in pipes using dry-coupled piezoelectric transducers," *Journal of Nondestructive Evaluation*, vol. 15, no. 1, pp. 11–20, 1996.

[42] M. J. S. Lowe, D. N. Alleyne, and P. Cawley, "Defect detection in pipes using guided waves," *Ultrasonics*, vol. 36, no. 1-5, pp. 147–154, 1998.

[43] R. S. Edwards, S. Dixon, and X. Jian, "Characterisation of defects in the railhead using ultrasonic surface waves," *NDT & E International*, vol. 39, no. 6, pp. 468–475, 2006.

[44] R. S. Edwards, Y. Fan, M. Papaelias, S. Dixon, C. L. Davis, and C. Roberts, "Ultrasonic detection of surface-breaking railhead defects," in *Review of Progress in Quantitative Nondestructive Evaluation, Vol 27A and 27B*, ser. AIP Conference Proceedings, Thompson, DO and Chimenti, DE, Ed., vol. 975. QNDE Programs, 2008, pp. 602–609.

[45] B. Dutton, A. R. Clough, and R. S. Edwards, "Near field enhancements from angled surface defects; a comparison of scanning laser source and scanning laser detection techniques," *Journal of Nondestructive Evaluation*, vol. 30, no. 2, pp. 64–70, 2011.

[46] B. Dutton, A. R. Clough, M. H. Rosli, and R. S. Edwards, "Non-contact ultrasonic detection of angled surface defects," *NDT & E International*, vol. 44, no. 4, pp. 353–360, 2011.

[47] S. E. Burrows, B. Dutton, and S. Dixon, "Laser generation of Lamb waves for defect detection: Experimental methods and finite element modeling," *IEEE Transactions on Ultrasonics Ferroelectrics and Frequency Control*, vol. 59, no. 1, pp. 82–89, 2012.

[48] A. R. Clough and R. S. Edwards, "Lamb wave near field enhancements for surface breaking defects in plates," *Journal of Applied Physics*, vol. 111, no. 10, pp. –, 2012.

[49] K. S. Ho, D. R. Billson, and D. A. Hutchins, “Ultrasonic Lamb wave tomography using scanned EMATs and wavelet processing,” *Nondestructive Testing and Evaluation*, vol. 22, no. 1, pp. 19–34, 2007.

[50] K. R. Leonard, E. V. Malyarenko, and M. K. Hinders, “Ultrasonic Lamb wave tomography,” *Inverse Problems*, vol. 18, no. 6, pp. 1795–1808, 2002.

[51] S. V. Walker, J.-Y. Kim, J. Qu, and L. J. Jacobs, “Fatigue damage evaluation in A36 steel using nonlinear Rayleigh surface waves,” *NDT & E International*, vol. 48, pp. 10 – 15, 2012.

[52] I. Viktorov, *Rayleigh and Lamb waves: physical theory and applications*, ser. Ultrasonic technology. Plenum Press, 1970.

[53] K. Graff, *Wave Motion in Elastic Solids*, ser. Dover Books on Engineering Series. Dover Publications, 1975.

[54] J. L. Dean, C. Trillo, A. F. Doval, and J. L. Fernandez, “Determination of thickness and elastic constants of aluminum plates from full-field wavelength measurements of single-mode narrowband Lamb waves,” *Journal of the Acoustical Society of America*, vol. 124, no. 3, pp. 1477–1489, 2008.

[55] R. J. Dewhurst, C. Edwards, A. D. W. McKie, and S. B. Palmer, “Estimation of the thickness of thin metal sheet using laser generated ultrasound,” *Applied Physics Letters*, vol. 51, no. 14, pp. 1066–1068, 1987.

[56] W. M. Gao, C. Glorieux, and J. Thoen, “Laser ultrasonic study of Lamb waves: determination of the thickness and velocities of a thin plate,” *International Journal of Engineering Science*, vol. 41, no. 2, pp. 219–228, 2003.

[57] Y. Hayashi, S. Ogawa, H. Cho, and M. Takemoto, “Non-contact estimation of thickness and elastic properties of metallic foils by laser-generated Lamb waves,” *NDT & E International*, vol. 32, no. 1, pp. 21–27, 1999.

[58] F. Jenot, M. Ouaftouh, M. Duquennoy, and M. Ourak, “Corrosion thickness gauging in plates using Lamb wave group velocity measurements,” *Measurement Science & Technology*, vol. 12, no. 8, pp. 1287–1293, 2001.

[59] F. Lefevre, F. Jenot, M. Ouaftouh, M. Duquennoy, P. Poussot, and M. Ourak, “Laser ultrasonics and neural networks for the characterization of thin isotropic plates,” *Review of Scientific Instruments*, vol. 80, no. 1, 2009.

[60] A. S. Murfin and R. J. Dewhurst, "Estimation of wall thinning in mild steel using laser ultrasound Lamb waves and a non-steady-state photo-EMF detector," *Ultrasonics*, vol. 40, no. 1-8, pp. 777–781, 2002.

[61] R. Zhang, M. X. Wan, and W. W. Cao, "Parameter measurement of thin elastic layers using low-frequency multi-mode ultrasonic Lamb waves," *IEEE Transactions on Instrumentation and Measurement*, vol. 50, no. 5, pp. 1397–1403, 2001.

[62] S. Dixon, P. A. Petcher, Y. Fan, D. Maisey, and P. Nickolds, "Ultrasonic metal sheet thickness measurement without prior wave speed calibration," *Journal of Physics D: Applied Physics*, vol. 46, no. 44, p. 445502, 2013.

[63] J. Curie and P. Curie, "Sur l'électricité polaire dans les cristaux hémièdres à faces inclinées," *Comptes rendus*, vol. 91, pp. 383–386, 1880.

[64] J. Nye, *Physical properties of crystals: their representation by tensors and matrices.* Clarendon Press, 1985.

[65] R. Kažys, A. Voleišis, and B. Voleišienė, "High temperature ultrasonic transducers: review," *Ultragarsas (Ultrasound)*, vol. 63, no. 2, pp. 7–17, 2008.

[66] S. Dixon, C. Edwards, and S. B. Palmer, "Ultrasonic thickness gauging using a dry couplant at elevated temperatures," *AIP Conference Proceedings*, vol. 557, no. 1, pp. 1600–1603, 2001.

[67] S. B. Palmer and S. Dixon, "Industrially viable non-contact ultrasound," *Insight*, vol. 45, no. 3, pp. 211–217, 2003.

[68] M. Hirao and H. Ogi, "Electromagnetic acoustic resonance and materials characterization," *Ultrasonics*, vol. 35, no. 6, pp. 413–421, 1997.

[69] C. Scruby and L. Drain, *Laser Ultrasonics: Techniques and Applications.* A. Hilger, 1990.

[70] R. Longo, S. Vanlanduit, J. Vanherzeele, and P. Guillaume, "A method for crack sizing using laser doppler vibrometer measurements of surface acoustic waves," *Ultrasonics*, vol. 50, no. 1, pp. 76 – 80, 2010.

[71] S. D. Sharples, R. A. Light, S. O. Achamfuo-Yeboah, M. Clark, and M. G. Somekh, "The SKED: speckle knife edge detector," *Journal of Physics: Conference Series*, vol. 520, no. 1, p. 012004, 2014.

[72] X. Jian, S. Dixon, R. Edwards, K. Quirk, and I. Baillie, “Effect on ultrasonic generation of a backplate in electromagnetic acoustic transducers,” *Journal of Applied Physics*, vol. 102, no. 2, pp. –, 2007.

[73] M. Murase, K. Kawashima, and O. Yoshida, “Group velocity measurement of various Lamb waves with two-beam laser interferometer,” *Japanese Journal of Applied Physics Part 1-Regular Papers Short Notes & Review Papers*, vol. 40, no. 5B, pp. 3595–3598, 2001.

[74] S. Kruger, M. Lord, and J. Monchalin, “Laser ultrasonic thickness measurements of very thick walls at high temperatures,” in *Review of Progress in Quantitative Nondestructive Evaluation, Vols 25A and 25B*, ser. AIP CONFERENCE PROCEEDINGS, Thompson, DO and Chimenti, DE, Ed., vol. 820. 2 HUNTINGTON QUADRANGLE, STE 1NO1, MELVILLE, NY 11747-4501 USA: AMER INST PHYSICS, 2006, Proceedings Paper, pp. 240–247, 32nd Annual Review of Process in Quantitative Nondestructive Evaluation, Brunswick, ME, JUL 31-AUG 05, 2005.

[75] W. Böttger, H. Schneider, and W. Weingarten, “Prototype EMAT system for tube inspection with guided ultrasonic waves,” *Nuclear Engineering and Design*, vol. 102, no. 3, pp. 369–376, 1987.

[76] S. Dixon and S. B. Palmer, “Wideband low frequency generation and detection of Lamb and Rayleigh waves using electromagnetic acoustic transducers (EMATs),” *Ultrasonics*, vol. 42, no. 10, pp. 1129–1136, 2004.

[77] B. Dutton, S. Boonsang, and R. J. Dewhurst, “A new magnetic configuration for a small in-plane electromagnetic acoustic transducer applied to laser-ultrasound measurements: Modelling and validation,” *Sensors and Actuators A: Physical*, vol. 125, no. 2, pp. 249–259, 2006.

[78] R. Ribichini, F. Cegla, P. B. Nagy, and P. Cawley, “Experimental and numerical evaluation of electromagnetic acoustic transducer performance on steel materials,” *NDT & E International*, vol. 45, no. 1, pp. 32–38, 2012.

[79] A. V. Clark and Y. Berlinsky, “Effect of liftoff on accuracy of phase velocity measurements made with electromagnetic-acoustic transducers,” *Research in Nondestructive Evaluation*, vol. 4, no. 2, pp. 79–96, 1992.

[80] J. D. Garrett, “Survey of displacement transducers below 50 mm,” *Journal of Physics E: Scientific Instruments*, vol. 12, no. 7, p. 563, 1979.

[81] I. Sherrington and E. Smith, “Modern measurement techniques in surface metrology: Part I; stylus instruments, electron microscopy and non-optical comparators,” *Wear*, vol. 125, no. 3, pp. 271 – 288, 1988.

[82] M. W. Sayers and S. M. Karamihas, *The little book of profiling*, 1998.

[83] K. Stout and L. Blunt, *Three Dimensional Surface Topography.* Elsevier Science, 2000.

[84] BSI, “Assessment of surface texture. guidance and general information,” British Standards Institution, BS 1134:2010, 2010.

[85] G. Bennig, “Atomic force microscope and method for imaging surfaces with atomic resolution,” Feb. 9 1988, US Patent 4,724,318.

[86] L. Gross, F. Mohn, N. Moll, P. Liljeroth, and G. Meyer, “The chemical structure of a molecule resolved by atomic force microscopy,” *Science*, vol. 325, no. 5944, pp. 1110–1114, 2009.

[87] J. Bennett and L. Mattsson, *Introduction to surface roughness and scattering*, ser. UUIP (Institute of Physics, Uppsala University). Optical Society of America, 1989.

[88] J. Schmit, K. Creath, and M. Kujawinska, “Spatial and temporal phase-measurement techniques: a comparison of major error sources in one dimension,” vol. 1755, 1993, pp. 202–211.

[89] A. Fertner and A. Sjolund, “Analysis of the performance of the capacitive displacement transducer,” *Instrumentation and Measurement, IEEE Transactions on*, vol. 38, no. 4, pp. 870–875, Aug 1989.

[90] Z. Chen and R. Luo, “Design and implementation of capacitive proximity sensor using microelectromechanical systems technology,” *IEEE Transactions on Industrial Electronics*, vol. 45, no. 6, pp. 886–894, Dec 1998.

[91] C. V. Dodd and W. E. Deeds, “Analytical solutions to eddy-current probe-coil problems,” *Journal of Applied Physics*, vol. 39, no. 6, pp. 2829–2838, 1968.

[92] B. Auld and J. Moulder, “Review of advances in quantitative eddy current nondestructive evaluation,” *Journal of Nondestructive Evaluation*, vol. 18, no. 1, pp. 3–36, 1999.

[93] W. Yin, R. Binns, S. Dickinson, C. Davis, and A. Peyton, “Analysis of the liftoff effect of phase spectra for eddy current sensors,” *Instrumentation and Measurement, IEEE Transactions on*, vol. 56, no. 6, pp. 2775–2781, 2007.

[94] G. Y. Tian, Y. Li, and C. Mandache, "Study of Lift-Off Invariance for Pulsed Eddy-Current Signals," *IEEE Transactions on Magnetics*, vol. 45, no. 1, pp. 184–191, 2009.

[95] Y. He, M. Pan, F. Luo, and G. Tian, "Reduction of lift-off effects in pulsed eddy current for defect classification," *IEEE Transactions On Magnetics*, vol. 47, no. 12, pp. 4753–4760, 2011.

[96] J. Gu and W. Yin, "Accurate distance measurement using an eddy current sensor based on an analytical model," in *Intelligent Computation Technology and Automation (ICICTA), 2010 International Conference on*, vol. 1, 2010, pp. 397–399.

[97] J. Achenbach, *Wave Propagation in Elastic Solids*, ser. North-Holland Series in Applied Mathematics and Mechanics. Elsevier Science, 1984.

[98] W. Slaughter, *The Linearized Theory of Elasticity.* Birkhäuser Boston, 2002.

[99] A. Einstein, "Die grundlage der allgemeinen relativitätstheorie," *Annalen der Physik*, vol. 354, no. 7, pp. 769–822, 1916.

[100] T. Freegarde, *Introduction to the Physics of Waves.* Cambridge University Press, 2013.

[101] C. Prada, D. Clorennec, and D. Royer, "Local vibration of an elastic plate and zero-group velocity Lamb modes," *Journal of the Acoustical Society of America*, vol. 124, no. 1, pp. 203–212, 2008.

[102] O. Trushkevych, Y. Fan, R. Perry, and R. S. Edwards, "Magnetic phase transitions in Gd64Sc36 studied using non-contact ultrasonics," *Journal of Physics D: Applied Physics*, vol. 46, no. 10, p. 105005, 2013.

[103] J. Buchler, M. Platte, and H. Schmidt, "Electronic-circuit for high-frequnecy and broad-band ultrasonic pulse-echo operation," *Ultrasonics*, vol. 25, no. 2, pp. 112–114, Mar 1987.

[104] A. Jerri, "The Shannon sampling theorem - its various extensions and applications: A tutorial review," *Proceedings of the IEEE*, vol. 65, no. 11, pp. 1565–1596, 1977.

[105] S. Dixon, C. Edwards, and S. B. Palmer, "High accuracy non-contact ultrasonic thickness gauging of aluminium sheet using electromagnetic acoustic transducers," *Ultrasonics*, vol. 39, no. 6, pp. 445–453, 2001.

[106] C. H. Lees, J. P. Andrews, and L. S. Shave, "The variation of Young's modulus at high temperatures," *Proceedings of the Physical Society of London*, vol. 36, no. 1, p. 405, 1923.

[107] H. Lamb, "On waves in an elastic plate," *Proceedings of the Royal Society of London. Series A, Containing Papers of a Mathematical and Physical Character*, vol. 93, no. 648, pp. 114–128, 1917.

[108] L. Rayleigh, "On the free vibrations of an infinite plate of homogeneous isotropic elastic matter," *Proceedings of the London Mathematical Society*, vol. s1-20, no. 1, pp. 225–237, 1888.

[109] H. Lamb, "On the flexure of an elastic plate," *Proceedings of the London Mathematical Society*, vol. s1-21, no. 1, pp. 70–91, 1889.

[110] J. B. Allen, "Short term spectral analysis, synthesis, and modification by discrete Fourier transform," *IEEE Transactions on Acoustics Speech and Signal Processing*, vol. 25, no. 3, pp. 235–238, 1977.

[111] M. Hirao and H. Ogi, *EMATs for Science and Industry: Noncontacting Ultrasonic Measurements*. Springer, 2003.

[112] B. W. Maxfield and C. M. Fortunko, "The design and use of electromagnetic acoustic-wave transducers (EMATS)," *Materials Evaluation*, vol. 41, no. 12, pp. 1399–1408, 1983.

[113] K. Sawaragi, H. J. Salzburger, G. Hübschen, K. Enami, A. Kirihigashi, and N. Tachibana, "Improvement of SH-wave EMAT phased array inspection by new eight segment probes," *Nuclear Engineering and Design*, vol. 198, no. 1-2, pp. 153–163, 2000.

[114] K. Kawashima, "Theory and numerical calculation of the acoustic field produced in metal by an electromagnetic ultrasonic transducer," *The Journal of the Acoustical Society of America*, vol. 60, no. 5, pp. 1089–1099, 1976.

[115] R. Edwards, Y. Fan, and S. Dixon, "High speed detection and characterization of defects in the railhead," vol. 894, 2007, pp. 1406–1412.

[116] F. Hernandez-Valle and S. Dixon, "Initial tests for designing a high temperature EMAT with pulsed electromagnet," *NDT & E International*, vol. 43, no. 2, pp. 171 – 175, 2010.

[117] O. Heaviside, "On the electromagnetic effects due to the motion of electrification through a dielectric," *Philosophical Magazine Series 5*, vol. 27, no. 167, pp. 324–339, 1889.

[118] S. Dixon, C. Edwards, and S. B. Palmer, "The optimization of Lamb and Rayleigh wave generation using wideband-low-frequency EMATs," *Review of Progress in Quantitative Nondestructive Evaluation, Vols 22a and 22b*, vol. 20, pp. 297–304, 2003.

[119] I. D. Kiteley, "A study of EMAT (electromagnetic acoustic transducer) operation on ferromagnetic metals," September 1999.

[120] R. Thurston and A. Pierce, *Ultrasonic Measurement Methods*, ser. Physical Acoustics. Elsevier Science, 2012.

[121] S. Groot and L. Suttorp, *Foundations of electrodynamics*. Noord-Hollandsche U.M., 1972.

[122] R. Bozorth, *Ferromagnetism*, ser. The Bell Telephone Laboratories series. Van Nostrand, 1951.

[123] N. Ida and J. Bastos, *Electromagnetics and Calculation of Fields*. Springer New York, 1997.

[124] H. Wheeler, "Formulas for the skin effect," *Proceedings of the IRE*, vol. 30, no. 9, pp. 412–424, 1942.

[125] X. Jian, S. Dixon, R. S. Edwards, and J. Reed, "Coupling mechanism of electromagnetic acoustical transducers for ultrasonic generation," *The Journal of the Acoustical Society of America*, vol. 119, no. 5, pp. 2693–2701, 2006.

[126] H. Young, R. Freedman, and A. Ford, *University Physics*, ser. Sears and Zemansky's University Physics: With Modern Physics. Pearson Education, Limited, 2011.

[127] Y. Fan, S. Dixon, and X. Ran, "Lift-off performance of ferrite enhanced generation EMATs," in *Review of Progress in Quantitative Nondestructive Evaluation, vol 27A and 27B*, ser. AIP Conference Proceedings, 2008, Proceedings Paper, pp. 835–840.

[128] M. Niethammer, L. J. Jacobs, J. M. Qu, and J. Jarzynski, "Time-frequency representations of Lamb waves," *Journal of the Acoustical Society of America*, vol. 109, no. 5, pp. 1841–1847, 2001.

[129] W. H. Prosser, M. D. Seale, and B. T. Smith, "Time-frequency analysis of the dispersion of Lamb modes," *The Journal of the Acoustical Society of America*, vol. 105, no. 5, pp. 2669–2676, 1999.

[130] A. Apostoloudia, E. Douka, L. J. Hadjileontiadis, I. T. Rekanos, and A. Trochidis, "Time-frequency analysis of transient dispersive waves: A comparative study," *Applied Acoustics*, vol. 68, no. 3, pp. 296–309, 2007.

[131] L. Cohen, *Time-frequency analysis*. PTR Prentice Hall : Prentice-Hall International (UK), 1995.

[132] A. V. Oppenheim, R. W. Schafer, and J. R. Buck, *Discrete-time signal processing*. Prentice Hall International, 1999.

[133] Z. N. Karam, "Computation of the one-dimensional unwrapped phase," Ph.D. dissertation, Massachusetts Institute of Technology, 2006.

[134] J. Tribolet, "A new phase unwrapping algorithm," *IEEE Transactions on Acoustics Speech and Signal Processing*, vol. 25, no. 2, pp. 170–177, 1977.

[135] K. Steiglitz and B. Dickinson, "Phase unwrapping by factorization," *IEEE Transactions on Acoustics Speech and Signal Processing*, vol. 30, no. 6, pp. 984–991, 1982.

[136] G. A. Sitton, C. S. Burrus, J. W. Fox, and S. Treitel, "Factoring very-high-degree polynomials," *Signal Processing Magazine, IEEE*, vol. 20, no. 6, pp. 27–42, 2003.

[137] W. Sachse and Y. H. Pao, "Determination of phase and group velocities of dispersive waves in solids," *Journal of Applied Physics*, vol. 49, no. 8, pp. 4320–4327, 1978.

[138] K. Aki and P. G. Richards, *Quantitative Seismology*. University Science Books, 2002.

[139] P. D. Welch, "The use of fast fourier transform for the estimation of power spectra: A method based on time averaging over short, modified periodograms," *Audio and Electroacoustics, IEEE Transactions on*, vol. 15, no. 2, pp. 70–73, Jun 1967.

[140] Ramiandrez-Pacheco, E. and Espina-Hernaandndez, J.H. and Caleyo, F. and Hallen, J.M., "Defect detection in aluminium with an eddy currents sensor," in *Electronics, Robotics and Automotive Mechanics Conference (CERMA), 2010*, 2010, pp. 765 –770.

[141] G. Y. Tian, Y. He, and A. Simm, "Pulsed eddy current systems for defect and geometrical profile measurement," *Seventh International Symposium On Precision Engineering Measurements and Instrumentation*, vol. 8321, 2011.

[142] R. T. Ko, M. P. Blodgett, S. Sathish, and T. R. Boehnlein, "Resonant frequency eddy current liftoff measurements for shot peening intensity assessment in materials," *AIP Conference Proceedings*, vol. 975, no. 1, pp. 344–351, 2008.

[143] C. N. Owston, "A high frequency eddy-current, non-destructive testing apparatus with automatic probe positioning suitable for scanning applications," *Journal of Physics E: Scientific Instruments*, vol. 3, no. 10, p. 814, 1970.

[144] P. Horowitz and W. Hill, *The Art of Electronics*. Cambridge University Press, 2001.

[145] K. L. Kaiser, *Electromagnetic Compatibility Handbook.* CRC Press, 2004.

[146] R. Thompson, “Physical principles of measurements with EMAT transducers,” *Physical Acoustics*, vol. 19, pp. 157–200, 1990.

[147] S. Wang, L. Kang, Z. Li, G. Zhai, and L. Zhang, “3-D modeling and analysis of meander-line-coil surface wave EMATs,” *Mechatronics*, vol. 22, no. 6, pp. 653 – 660, 2012, special Issue on Intelligent Mechatronics (LSMS2010 & ICSEE2010).

[148] M. Rosli, R. Edwards, and Y. Fan, “In-plane and out-of-plane measurements of Rayleigh waves using EMATs for characterising surface cracks,” *NDT & E International*, vol. 49, no. 0, pp. 1 – 9, 2012.

[149] P. Huthwaite and F. Simonetti, “High-resolution guided wave tomography,” *Wave Motion*, vol. 50, no. 5, pp. 979 – 993, 2013.

[150] X. Jian, S. Dixon, K. Quirk, and K. Grattan, “Electromagnetic acoustic transducers for in- and out-of plane ultrasonic wave detection,” *Sensors and Actuators A: Physical*, vol. 148, no. 1, pp. 51 – 56, 2008.

[151] G. Kaye and T. Laby, *Tables of physical and chemical constants.* Longman, 1995.

[152] V. Bagad, *Mechatronics.* Technical Publications, 2009.

[153] I. Hughes and T. Hase, *Measurements and Their Uncertainties: A Practical Guide to Modern Error Analysis.* OUP Oxford, 2010.

[154] A. Montalibet, J. Jossinet, A. Matias, and D. Cathignol, “Interaction ultrasound-magnetic field: experimental setup and detection of the interaction current,” in *Ultrasonics Symposium, 2000 IEEE*, vol. 1, Oct 2000, pp. 533–536 vol.1.

[155] K. D. Hahn, E. M. Johnson, A. Brokken, and S. Baldwin, “Eddy current damping of a magnet moving through a pipe,” *American Journal of Physics*, vol. 66, no. 12, pp. 1066–1076, 1998.

[156] J. Morrison, S. Dixon, M. Potter, and X. Jian, “Lift-off compensation for improved accuracy in ultrasonic lamb wave velocity measurements using electromagnetic acoustic transducers (EMATs),” *Ultrasonics*, vol. 44, Supplement, no. 0, pp. e1401 – e1404, 2006, proceedings of Ultrasonics International (UI) and World Congress on Ultrasonics (WCU).

[157] R. Ribichini, “Modelling of electromagnetic acoustic transducers,” Ph.D. dissertation, Imperial College London, 2011.

[158] B. Noble, S. Harris, and K. Dinsdale, "The elastic modulus of aluminium-lithium alloys," *Journal of Materials Science*, vol. 17, no. 2, pp. 461–468, 1982.

[159] S. Hill and S. Dixon, "Localisation of defects with time and frequency measurements using pulsed arrays," *NDT & E International*, vol. 67, no. 0, pp. 24 – 30, 2014.

[160] Y. Fainman, E. Lenz, and J. Shamir, "Optical profilometer: a new method for high sensitivity and wide dynamic range," *Appl. Opt.*, vol. 21, no. 17, pp. 3200–3208, Sep 1982.

[161] Posic, "Linear encoder technology," Posic, 2012.10.04.

[162] D.-X. Chen, J. Brug, and R. B. Goldfarb, "Demagnetizing factors for cylinders," *Magnetics, IEEE Transactions on*, vol. 27, no. 4, pp. 3601–3619, Jul 1991.

[163] A. H. Ar-Rawi, M. Moghavvemi, and W. M. A. Wan-Ibrahim, "Comparing between three current source circuits for using in bio electrical impedance design," in *Technical Postgraduates (TECHPOS), 2009 International Conference for*, Dec., pp. 1–4.

[164] C. P. Turner, "Histogram errors," http://suchideas.com/articles/maths/applied/histogram-errors/, Apr 2012, [Online; accessed 29-September-2014].

[165] A. Papoulis and S. Pillai, *Probability, Random Variables, and Stochastic Processes*, ser. McGraw-Hill series in electrical and computer engineering. McGraw-Hill, 2002.

[166] E. DeGarmo, *Materials and Processes in Manufacturing.* Macmillan Publishers Limited, 1979.